Karlsruhe Institute of Technology

The Effective Description of General Neutrino Interactions in Tritium β Decay and first Constraints based on the second KATRIN Science Run

Zur Erlangung des akademischen Grades einer
Doktorin der Naturwissenschaften (Dr. rer. nat.)
von der KIT-Fakultät für Physik
des Karlsruher Instituts für Technologie (KIT)
angenommene **Dissertation** von

M. Sc. Caroline Fengler

aus Gießen

Referent:	Prof. Dr. Guido Drexlin
	Institut für Experimentelle Teilchenphysik, KIT
Korreferentin:	Prof. Dr. Kathrin Valerius
	Institut für Experimentelle Teilchenphysik, KIT

Tag der mündlichen Prüfung: 06.06.2025

Declaration of Authorship

Herewith I affirm that I wrote the current thesis on my own and without the usage of any other sources or tools than the cited ones and that this thesis has not been handed neither in this nor in equal form at any other official commission.

Erklärung der Selbstständigkeit

Hiermit versichere ich, die vorliegende Arbeit selbstständig angefertigt zu haben und keine Hilfsmittel jenseits der kenntlich gemachten verwendet zu haben. Weiterhin habe ich weder diese noch eine äquivalente Version dieser Arbeit bei einer anderen Prüfungskommission vorgelegt.

Karlsruhe, April 30th, 2025	
Ort, Datum	Caroline Fengler

Contents

Introduction

Neutrinos are the most abundant known particles in the cosmos, and their mysterious properties have fascinated physicists ever since they were first proposed by Pauli in 1930 to explain the shape of the β spectrum. Since then, numerous investigations have advanced our understanding of this mysterious particle, while at the same time revealing new questions that need to be answered. The discovery of neutrino flavour oscillations provided evidence for a non-zero neutrino mass, and neutrino-oscillation experiments have since explored the difference in neutrino-mass states; however, the absolute neutrino-mass scale remains undiscovered.

The Karlsruhe Tritium Neutrino Experiment (KATRIN) experiment aims to probe the neutrino-mass scale in an direct kinematic measurement approach, utilising the β decay of gaseous tritium and a high-resolution electron spectrometer. By inferring the neutrino mass from its characteristic shape distortion close to the spectral endpoint, KATRIN sets the world-leading upper limit for direct neutrino-mass searches at 0.45 eV (90 % Confidence Level (CL)). Similarly, the high-precision measurement of the β spectrum can be investigated for further shape deformations that hint at new physics.

The nature of these new physics contributions remains unclear due to the abundance of theories and the elusive nature of the neutrino. A particularly broad and therefore powerful approach to identify such new physics is offered by the theory of general neutrino interactions (GNI) [162, 61, 63], which describes the weak interaction beyond its Standard Model V-A structure in a more generalized manner than the already well-studied neutrino non-standard interactions (NSI) [88, 176, 98, 79, 30]. The new low-energy effective interaction terms of the GNI theory can also be generated by (sterile-neutrino extended) Standard Model effective field theory (SM(N)EFT) operators of mass dimension 6 [215, 125, 75, 61]. Therefore, the GNI theory connects new physics phenomena both below and above the weak scale through the effective field theory (EFT). In recent years, a multitude of investigations have been conducted for various neutrino interaction channels, reaching from neutrino-oscillation experiments [60, 144, 123] to neutrino-scattering processes [155, 72, 37, 178, 191, 158] to studies of β-decay processes [46, 117, 75, 125]. In this work, we examine the impact of GNI on the β-decay spectrum of tritium as measured by KATRIN, also considering the potential existence of additional eV-scale neutrino-mass states.

This work is structured as follows:

In chapter 1, a concise introduction into neutrino physics is given. Following a brief historical introduction of the beginnings of the research field, the neutrino is discussed in the context of the standard model and beyond. Different mechanism for the generation of neutrino masses are presented and the experimental approaches to determine the absolute neutrino mass are compared.

Chapter 2 then introduces the basic concept of effective field theories and describes, how this framework can be used to search for new physics phenomena, such as the general neutrino interactions. In addition to defining the theory of general neutrino interactions, the chapter comments on both the possible theoretical origins of such new interactions and their experimental testability.

Chapter 3 focuses on the experimental setup of the KATRIN experiment, presenting the relevant components and their interplay within the setup.

Thereafter, the experimental model describing the physical effects and transmission conditions of the experimental setup is laid out in chapter 4, starting from the derivation of the differential β spectrum to the integral count rate observed at the detector. In this context, the relevant systematic effects and their influence on the β spectrum are described.

Chapter 5 lays the foundation for the data analysis by describing the statistical methods necessary to fit the model to the data and to place reliable constraints on multi-dimensional parameter spaces. It also introduces the analysis environment, comprising the required statistical methods.

The data set used for the analysis and the corresponding measurement conditions are summarised in chapter 6.

Finally, the search for general neutrino interactions on KATRIN data is performed in chapter 7, combining the insights of the previous chapters. Based on the theory of general neutrino interactions, the effective differential decay rate is derived and the transformations allowing to derive constraints on individual interactions are given. The analysis strategy is outlined and studies ensuring the correct coverage of the exclusion contours are presented. Finally, the exclusion contours for both parameter spaces, with and without an additional heavy neutrino, are discussed and the constraints on individual interactions are placed in the context of existing constraints. In addition, more specific physics scenarios are explored, such as a right-handed W boson, a charged Higgs boson, and leptoquarks.

Chapter 8 concludes with a summary and outlook, addressing the future potential of the search for general neutrino interactions at KATRIN.

1. Neutrino Physics

This chapter gives a concise introduction into neutrino physics. Starting with an overview of the beginnings of the research field in section 1.1, the neutrino is set in context of the Standard Model (SM) in section 1.2. Furthermore, the properties of the neutrino calling for an extension of the SM, that is the neutrino oscillations and the neutrino mass, are further explored in sections 1.3 and 1.4, respectively.

1.1 History of Neutrino Physics

In 1914, intensive studies by Chadwick resulted in the first observation of the β-decay spectrum [70]. Contrary to the prevailing assumption at the time that the β decay is a two-body process, the experiment revealed a continuous spectrum. This observation posed a challenge to the firmly established energy-momentum conservation. Pauli proposed a resolution to this anomaly in 1930, which involved expanding the β decay to a three-body process, thereby ensuring the conservation of energy, momentum and angular momentum. He characterised the additional constituent of the decay as an electrically neutral particle with spin $\frac{1}{2}$, which is only charged under the weak interaction [140]. Fermi proceeded by combining the experimental findings of Chadwick with Pauli's theory and formulating the β decay as single-vertex three-body decay of a neutron (n) to a proton (p), electron (e^-), and a massless neutral particle, the electron anti-neutrino ($\overline{\nu}_\mathrm{e}$)

$$\mathrm{n} \rightarrow \mathrm{p} + \mathrm{e}^- + \overline{\nu}_\mathrm{e}\,. \tag{1.1}$$

In 1942, Wang addressed the challenge of detecting the elusive neutrino by proposing a detection via the inverse β decay [211]. This approach was subsequently employed by Cowan and Reines, who succeeded in detecting neutrinos via the inverse β decay at the Savannah River Experiment in 1956 [189]. Antineutrinos emanating from the Savannah river reactor were captured on protons of a 200 L cadmium chloride-infused water target. The positron and neutron resulting from this reaction were detected by a delayed-coincidence signature, with the positron annihilating rapidly with an electron producing two signature photons. In a second, about 10 µs delayed process, the neutron is captured by the cadmium chloride, emitting a photon during de-excitation. The detection of both signals confirmed the predictions of the β-decay process.

In addition to the electron neutrino ν_e, two further neutrino flavours have been discovered: the muon neutrino ν_μ [82] and the tau neutrino ν_τ [149]. Experiments such as ALEPH have demonstrated, that only three neutrino flavours exist [83], thereby validating their inclusion in the SM.

1.2 Neutrinos in the Standard Model

The Standard Model (SM) of particle physics is a comprehensive theory of the elementary particles and their fundamental interactions within the framework of quantum field theory, that has been developed in the mid 1970s. It is described by the SU(3)×SU(2)×U(1) gauge group and comprises six quarks (*up*, *down*, *charm*, *strange*, *top*, *bottom*), three charged leptons (e, μ, τ) with their neutral leptonic partners, the neutrinos (ν_e, ν_μ, ν_τ), as well as four vector bosons (*gluon*, *photon*, Z^0, $W^\pm$). The Quantum Chromodynamics (QCD) SU(3) subgroup describes the strong force between the quarks, mediated by gluons. The Weinberg-Salam SU(2)×U(1) subgroup [212] represents the electroweak force, which is a unification of electromagnetic and weak force. Photons mediate the electromagnetic force, Z and $\mathrm{W}^\pm$ bosons the weak force. An additional scalar boson, the *Higgs boson*, is generated by Spontaneous Symmetry Breaking (SSB) of the electroweak symmetry below the electroweak scale through the Higgs field H. Alongside the Higgs boson, three massless goldstone bosons are produced, that manifest themselves as the longitudinal component of the Z^0 and $\mathrm{W}^\pm$ gauge bosons. The masses of both Z^0 and $\mathrm{W}^\pm$ bosons arise through this SSB process. The fermions acquire their mass through interaction with the Higgs field. This process demands the existence of both left- and right-handed components of the fermion. The Yukawa Lagrangian for leptons reads

$$\mathcal{L}_{\text{Yukawa}} = -y^e_{\alpha\beta}\,\bar{\ell}_\alpha\, H\, e_{\beta,\mathrm{R}} + \text{h.c.}, \tag{1.2}$$

where $e_{\beta,\mathrm{R}} = e_\mathrm{R}$, μ_R, τ_R are the right handed SU(2) singlets and

$$\ell_\alpha = \begin{pmatrix} \nu_{e,\mathrm{L}} \\ e_\mathrm{L} \end{pmatrix}, \begin{pmatrix} \nu_{\mu,\mathrm{L}} \\ \mu_\mathrm{L} \end{pmatrix}, \begin{pmatrix} \nu_{\tau,\mathrm{L}} \\ \tau_\mathrm{L} \end{pmatrix}$$

the left-handed SU(2) doublets of the leptons. $y^e_{\alpha\beta}$ is the Yukawa coupling strength. Applying the vacuum expectation value (vev) of the Higgs field $\langle H\rangle = \frac{1}{\sqrt{2}}\begin{pmatrix}0 & v\end{pmatrix}^\top$ with $v \approx 246\,\mathrm{GeV}$ [173] gives

$$\mathcal{L}_{\text{mass}} = -\frac{v}{\sqrt{2}}\, y^e_{\alpha\beta}\, \bar{e}_{\alpha,\mathrm{L}} e_{\beta,\mathrm{R}} + \text{h.c.} \tag{1.3}$$

The prefactor $\frac{v}{\sqrt{2}}\, y^e_{\alpha\beta}$ corresponds to the lepton mass. Within the SM theory, the only fermion predicted to be massless is the neutrino. However, observations in the 1990s of a new phenomenon, the neutrino oscillations, led to the conclusion, that this prediction must be inaccurate. Thus far, the only part of the SM not withstanding the experimental scrutiny is the neutrino sector. The discovery of neutrino oscillations led to a re-evaluation of the lepton number conservation within each lepton family (ℓ, ν_ℓ) with $\ell \in \{e, \mu, \tau\}$ and the pure left-handedness of the neutrino. Consequently, a wide variety of neutrino mass generation mechanism and possible extensions of the SM have since been proposed.

1.3 Neutrino Oscillations

In 1964, Bahcall proposed the use of the inherently small interaction cross section of neutrinos to gain insight into the nuclear energy production of stars, such as the Sun, and calculated the solar neutrino flux [42]. In order to verify this prediction, the Homestake experiment was set out to measure the total electron-neutrino flux coming from the Sun, utilising a chemical detection process with neutrino capture on ^{37}Cl [77]. Despite employing a detector mass of 615 t of perchloroethylene (C_2Cl_4), only 1/3 of the anticipated rate was detected, thereby giving rise to the solar-neutrino problem [43]. Subsequent experiments, including Kamiokande, SAGE, GALLEX, and Super-Kamiokande [206, 3, 124, 106], yielded consistent results, confirming the same solar electron-neutrino rate. As no adjustments to the solar model could provide a rationale for these results, it was hypothesised that the effect was related to the propagation of the neutrinos. The Sudbury Neutrino Observatory (SNO) ultimately resolved the solar-neutrino problem by measuring the solar flux of all neutrino flavours and thereby confirming that neutrinos indeed mix amongst their flavours [14]. Later, this mixing behaviour was refined as neutrino oscillations, and experimentally confirmed by the Super-Kamiokande and KamLAND experiments [107, 91]; it directly implied that neutrinos must carry mass, as the oscillation mechanism requires the neutrinos of different flavours to differ in mass.

The notion of an admixture of neutrinos capable of oscillating between states was initially proposed by Pontecorvo in 1957 [183]. This early concept was further developed by Maki, Nakagawa and Sakata in 1962, establishing a theoretical framework to describe the oscillation of the neutrino's flavour states [165].

The theoretical concept describing the phenomenon of neutrino oscillations is based on the flavour states of the neutrino, defined as the eigenstates of the weak interaction, constituting a superposition of the corresponding mass states, which are themselves eigenstates of the free Hamiltonian. In this theoretical framework, the flavour states are denoted by $|\nu_\alpha\rangle$ with $\alpha \in \{\mathrm{e}, \mu, \tau\}$ and the mass states are symbolised by $|\nu_k\rangle$ with $k \in \{1, 2, 3\}$. The unitary PMNS matrix expresses the mixing of neutrino states through the mixing angles θ_{12}, θ_{23}, and θ_{13}, and the CP violating phase δ_{CP}. Two additional Majorana phases α_1 and α_2 appear, if the neutrino is its own anti-particle, namely a Majorana particle. The relation between the flavour and mass states then reads [199]

$$|\nu_\alpha(t)\rangle = \sum_k U_{\alpha k} \exp\left\{-\mathrm{i}E_k^{\mathrm{tot}} t\right\} |\nu_k\rangle \ . \tag{1.4}$$

The factor $\exp\left\{-\mathrm{i}E_k^{\mathrm{tot}} t\right\}$ describes the time propagation of a free particle; the total energy of the neutrino-mass state under relativistic approximation and the "same energy" and "same momentum" assumption ($E_k = E_j = E \simeq p$) reads $E_k^{\mathrm{tot}} = \sqrt{p_k^2 + m_k^2} \simeq p + m_k^2/2E$. The probability P of detecting a neutrino with initial flavour state α in a flavour state β under propagation in vacuum can be derived under the assumption of CP invariance as [59]

$$\mathrm{P}(\nu_\alpha \to \nu_\beta) = |\langle\nu_\beta|\nu_\alpha(t)\rangle|^2 = \delta_{\alpha\beta} - 4\sum_{k>j} \mathrm{Re}(U^*_{\alpha k} U_{\beta k} U_{\alpha j} U^*_{\beta j}) \sin^2\left(\frac{\Delta m^2_{kj} L}{4E}\right) \ . \tag{1.5}$$

Here, the oscillation length L is the distance between the source and the detector. The energy of the neutrinos is denoted by E. Δm^2_{kj} is the difference between the squared masses $\Delta m^2_{kj} = m_k^2 - m_j^2$. Consequently, oscillation experiments can only yield mass differences; the absolute masses of neutrinos remain inaccessible with this experimental approach. Furthermore, in order to ascertain the ordering of the neutrino mass states, it is necessary to go beyond equation 1.5, for example by incorporating matter effects in the experimental setup [188]. The determination of the sign of Δm^2_{23} has so far proven challenging, resulting in two possible orderings for the mass eigenstates: the Normal

Table 1.1: Summary of the current best measurements of the neutrino mixing parameters, the mass differences of the neutrino mass eigenstates, and the CP violating phase. Results are given for both the normal and the inverted hierarchy. All values taken from [173].

Parameter	**Value**	**Comments**	**References**
$\sin^2(\theta_{12})$	$0.307^{+0.013}_{-0.012}$	Results by KamLAND + global solar; assuming 3ν	[7]
$\sin^2(\theta_{23})$ (IO)	$0.553^{+0.016}_{-0.024}$	PDG average: IceCube, T2K, NOvA, MINOS, and Super-Kamiokande	[1, 6, 10, 12, 4]
$\sin^2(\theta_{23})$ (NO)	$0.558^{+0.015}_{-0.021}$		
$\sin^2(\theta_{13})$	$(2.19 \pm 0.07) \times 10^{-2}$	PDG average: T2K, Daya Bay, Double Chooz, and RENO	[6, 33, 142, 201, 44, 32]
Δm^2_{21}	$(7.53 \pm 0.18) \times 10^{-5}\,\mathrm{eV}^2$	Results by KamLAND + global solar + SBL + accelerator; assuming 3ν	[110]
Δm^2_{32} (IO)	$(-2.529 \pm 0.029) \times 10^{-3}\,\mathrm{eV}^2$	PDG average: IceCube, T2K, Daya Bay, NOvA, MINOS, Super-Kamiokande, and RENO	[1, 6, 33, 10, 12, 4, 44]
Δm^2_{32} (NO)	$(2.455 \pm 0.028) \times 10^{-3}\,\mathrm{eV}^2$		
δ_{CP}	$(1.19 \pm 0.22)\,\pi$ rad	PDG average: T2K, NOvA, and Super-Kamiokande	[6, 10, 4]

Ordering (NO) with $m_1 < m_2 < m_3$ and the Inverted Ordering (IO) with $m_3 < m_1 < m_2$ [199]. The data of oscillation experiments exhibits different tendencies as to which ordering is favoured [96]. The most recent neutrino oscillation parameters are summarised in table 1.1.

1.4 Neutrino Mass Generation Mechanisms and Measurement Approaches

The observation of neutrino oscillations indicates that the SM is incomplete and requires the incorporation of Beyond the Standard Model (BSM) physics to elucidate how neutrinos acquire their mass. Concurrently, this observation has evoked the need to develop experimental methods to ascertain the absolute neutrino mass through measurements. This section offers a brief review of the theoretical extensions of the SM and the experimental approaches.

Neutrino Mass Generation Mechanisms: The most straightforward method for introducing neutrino masses is to add three right-handed neutrinos as singlets to the SM, analogous to the charged leptons. Through interaction with the Higgs field, the neutrinos acquire mass, as do all other fermions, following electroweak symmetry breaking. Thus, equation 1.2 can be extended by a Yukawa mass term for neutrinos by introducing a hypercharge-neutral[1] right-handed neutrino singlet $\nu_{\alpha,\mathrm{R}}$:

$$\mathcal{L}_{\mathrm{Yukawa},\,\nu} = -y^{\nu}_{\alpha\beta}\,\bar{\ell}_\alpha\,\tilde{H}\,\nu_{\beta,\mathrm{R}} + \text{h.c.} \quad \xrightarrow{\text{SSB}} \quad -\frac{v}{\sqrt{2}}\,y^{\nu}_{\alpha\beta}\,\bar{\nu}_{\alpha,\mathrm{L}}\,\nu_{\beta,\mathrm{R}} + \text{h.c.} \tag{1.6}$$

In accordance with established upper limits on the absolute neutrino mass scale, the Yukawa coupling is required to be of $\mathcal{O}(10^{-13})$, seven orders of magnitude smaller compared to the electron as the next-lightest fermion. While this is technically natural [132], there

---

[1] The weak hypercharge Y_{W} is a quantum number corresponding to the gauge symmetry U(1). It links the electric charge Q with the third component of the weak isospin T_3 via $Y_{\mathrm{W}} = 2(Q - T_3)$.

are numerous approaches to address the large hierarchy in more elaborate theoretical approaches. These so-called seesaw mechanisms are often accompanied by Majorana neutrinos, which are conjugates of their own anti-particle $\psi = \psi^c := \mathcal{C}\bar{\psi}^T$ [2]. Further details are introduced and discussed in [114]. Given these properties, the Majorana mass term reads

$$\mathcal{L}_{\text{mass}} = -\frac{1}{2}\, m_{\alpha\beta}\, \bar{\nu}^c_{\alpha,\,\text{L}}\, \nu_{\beta,\,\text{L}} + \text{h.c.} \tag{1.7}$$

However, this Majorana mass term cannot be generated from renormalizable gauge-invariant SM operators. It is an effective term with mass dimension larger than the one of the SM Lagrangian and thus necessitates the existence of heavy new physics contributions beyond the currently experimentally accessible energy scale in order to become renormalizable. The underlying framework for constructing an Effective Field Theory (EFT) below a certain mass scale Λ is further introduced in chapter 2. The Weinberg operator [213] offers the simplest realisation of a Majorana mass term as a SM extension at mass dimension 5:

$$\mathcal{L}^{(5)} = \frac{C^{\alpha\beta}_{\nu\nu}}{\Lambda}\, (\bar{\ell}^c_\alpha i\tau_2 H)(\tilde{H}^\dagger \ell_\beta). \tag{1.8}$$

This formulation implies a suppression by v^2/Λ for new physics far above weak scale, thereby providing a compelling reason for the smallness of the neutrino masses. There exist numerous variations of the seesaw mechanism that can generate the Weinberg operator; the most common ones can be grouped into type-I and type-II seesaw mechanisms. Both introduce heavy new particles, whose inverse mass suppresses the neutrino masses.

Type-I seesaw mechanism [168]: This mechanism introduces SM right-handed neutrino singlets, so called sterile neutrinos, $N_{\alpha,\,\text{R}}$ to the SM to produce Dirac masses. When writing down all possible terms, a Majorana mass term simultaneously appears, due to the sterile neutrinos being neutral under the SM gauge group. In total, a kinematic term, a Majorana mass term, and a Yukawa mass term can be written down:

$$\mathcal{L}_{4,\,N} = i\bar{N}_{\alpha,\,\text{R}}\, \gamma^\mu \partial_\mu\, N_{\alpha,\,\text{R}} - (\frac{1}{2}\, \bar{N}^c_{\alpha,\,\text{R}}\, M_{\alpha\beta}\, N_{\beta,\,\text{R}} + \text{h.c.}) - (y^\nu_{\alpha\beta}\, \bar{\ell}_\alpha\, N_{\beta,\,\text{R}}\, \tilde{H} + \text{h.c.}) \tag{1.9}$$

Herein, the number of sterile neutrinos is not restricted by the theory. The introduction of three sterile neutrinos, along with the vanishing of $M_{\alpha\beta}$, results in a pure Dirac nature of the neutrinos. Conversely, for $M_{\alpha\beta} \neq 0$, Majorana neutrino masses are produced. In the case of a very large Majorana mass scale $|M|$, the three mass eigenstates, which are composed primarily of the active neutrinos, scale with $(y^\nu)^2 v^2/|M|$, while the sterile neutrinos scale with $|M|$. Furthermore, the flavour mixing is suppressed by $1/M$, which agrees with the near-unitarity of the PMNS matrix.

Type-II seesaw mechanism [196]: The second type seesaw mechanism introduces a suppression of the neutrino masses by adding a heavy scalar $\text{SU}(2)_\text{L}$ triplet Δ with hypercharge 2 in the following way:

$$\mathcal{L}_{\text{type-II}} = -y^\nu_{\alpha\beta}\, \bar{\ell}^c_\alpha\, (i\tau_2)\, \Delta\, \ell_\beta\, -\, \lambda_{\Delta H}\, \tilde{H}^\dagger\, \Delta^\dagger\, H\, +\, \text{h.c.} \tag{1.10}$$

---

[2] The particle-antiparticle conjugation $\mathcal{C}$ exchanges the creation and annihilation operators of particles and antiparticles, thereby turning a left-chiral spinor into a right-chiral one and vice versa, e.g. $\psi^c_\text{L} = \psi_\text{R}$.

The new scalar Δ connects the neutrino bilinear $\bar{\nu}_{\mathrm{L}}^{c}\nu_{\mathrm{L}}$ in the Yukawa interaction term to the Higgs field in the scalar interaction term. This indirect link between the two terms again leads to the neutrino mass being suppressed by a heavy mass scale m_{Δ}^{2} when integrating out the heavy triplet at tree-level [166]:

$$m_{\nu}^{\alpha\beta} = \frac{2\, y_{\alpha\beta}^{\nu}\, \lambda_{\Delta H}\, v^{2}}{m_{\Delta}^{2}}. \tag{1.11}$$

There are numerous extensions of these seesaw models, including, but not limited to, additional radiative corrections [163, 180] and models assuming approximate lepton number conservation [112, 74].

Different experimental approaches can provide insight into the absolute neutrino mass scale and some even into the Dirac or Majorana nature of neutrinos:

Cosmology: Neutrinos play a key role in the formation of large-scale cosmic structures, as they are among the most abundant particles in the universe. Due to their weak interaction and relativistic velocity, they can escape overdense regions, thereby carrying away mass and slowing down the growth rate of large-scale structures. Similarly, the expansion rate of the universe is coupled to the cosmic energy density, which neutrinos contribute to. As both effects are independent of the flavour of the neutrinos, they constrain the direct sum of the neutrino mass eigenstates

$$m_{\mathrm{cosm}} = \sum_{i} m_{i} \tag{1.12}$$

through cosmological observations. The derived limit is dependent on the chosen cosmological model. Recently, the Dark Energy Spectroscopic Instrument (DESI) released a new limit on the sum of neutrino masses, based on their constraint on the expansion of the universe combined with the data from the Planck satellite, of $\sum_i m_i < 72\,\mathrm{meV}$ (95 % CL) [87]. To obtain this result, DESI measured the position of several million galaxies and analysed the data for Baryonic Acoustic Oscillations (BAO)[3], while the Planck satellite focussed on the “empty spaces” in the universe to measure the Cosmic Microwave Background (CMB) spectrum[4]. The improved knowledge from the BAO is then used as an additional constraint in the analysis of Planck’s CMB data. The thereby obtained limit on the neutrino mass sum is already lower than the minimum neutrino mass sum for the IO hierarchy, based on neutrino oscillation data [173], of 100 meV, and approaches the minimum for the NO hierarchy of 58 meV. The implications of these results, including model dependencies, systematic effects, and new physics scenarios, are currently being discussed [171].

Neutrinoless Double Beta Decay ($0\nu\beta\beta$): Information on the neutrino mass can be obtained by measuring the half-life of the hypothetical $0\nu\beta\beta$ decay. A double β decay is solely realised by nuclei, for which the single β decay is energetically forbidden. The $0\nu\beta\beta$ decay furthermore requires the neutrinos to be of Majorana nature, thereby allowing a virtual neutrino exchange between the two simultaneous β decays. Experimentally, materials such as ^{76}Ge, ^{128}Te or ^{136}Xe are applied as source in low-background setups,

---

[3] BAO show up as spherical patterns in the matter distribution of the universe, which have been shaped by density fluctuations in the primordial plasma right before the decoupling of the photons. The size of these patterns contains information about the expansion of the universe.

[4] The CMB is formed by the photons that were emitted at the time of photon decoupling and fill all space of the observable universe. Their spectrum has been redshifted to microwave scales due to the expansion of the universe and carries information about the early universe.

searching for a monoenergetic-peak signature at the energy of the Q-value[5]. Despite the absence of any observation so far, the effective Majorana mass

$$m_{\beta\beta} = |\sum_i U_{\mathrm{e}i}^2 m_i|, \tag{1.13}$$

representing the coherent sum of the mass eigenstates of the electron neutrino weighted by the PMNS matrix elements, can be constrained by the upper limit on the decay half-life $T_{1/2}^{0\nu}$ [218]

$$T_{1/2}^{0\nu} \sim \frac{1}{|M_{0\nu\beta\beta}|^2 \, m_{\beta\beta}^2} \, . \tag{1.14}$$

One sources of uncertainty in this determination is the theoretical calculation of the nuclear matrix element $M_{0\nu\beta\beta}$, thus a range of upper limits is commonly given. The sensitivity of the experimental setup is determined by a combination of factors, such as the energy resolution, the background, and the amount of source nuclei, which are challenging to optimise simultaneously. The KamLAND-Zen Collaboration poses the most stringent constraints to date at $m_{\beta\beta} < (0.036 - 0.156)\,\mathrm{eV}$ (90 % CL) [8].

Direct kinematic measurements: The single β decay allows for direct, model-independent probing of the neutrino mass. This laboratory approach relies exclusively on the kinematics of the β decay and a precise measurement of its spectral shape close to the kinetic endpoint E_0, where the neutrino mass signal is most prominent (see figure 1.1). The KATRIN experiment employs high-precision electron spectroscopy of the tritium β decay to determine the squared effective electron antineutrino mass

$$m_{\beta}^2 = \sum_i |U_{\mathrm{e}i}^2| m_i^2. \tag{1.15}$$

A comprehensive description of the experimental setup can be found in chapter 3. Utilising this approach, the KATRIN collaboration has set the world-leading upper limit from direct kinematic measurement, which is $m_{\beta} < 0.45\,\mathrm{eV}$ (90 % CL) [17].

There are upcoming experiments developing new experimental approaches to determine the neutrino mass, including Project 8 [78], which measures the emission of cyclotron radiation of the tritium β electrons in a magnetic field, and the ECHo and HOLMES experiments [111, 66], which analyse the ^{163}Ho electron-capture spectrum. The setup of Project 8 allows for a differential measurement of the tritium β spectrum with intrinsically low background by detecting the cyclotron frequency of the electrons. With a first demonstrator, they reach a sensitivity of $m_{\nu} < 155\,\mathrm{eV}$ at 90 % CL [39]. Future challenges for reaching their goal sensitivity of about 50 meV will be the development of an atomic tritium source and enlarging the detector volume, while further improving the accuracy of the magnetic field strength and the observation time of the electrons. Both Holmium-based experiments, ECHo and HOLMES, apply low-temperature calorimeters to measure the ^{163}Ho electron-capture spectrum and detect its neutrino-mass-dependent shape close to the kinetic endpoint. HOLMES recently set a new constraint at $m_{\nu} < 27\,\mathrm{eV}$ at 90 % CL with their current setup [29]. The objective of both experiments is to probe the neutrino mass scale in the low-meV region in the future, which will require a noticeable upscaling of the experimental setups, in addition to an excellent understanding of the spectral shape.

---

[5] The Q-value is defined as the total amount of released decay energy $Q = M_{\mathrm{mother\,nucleus}} - M_{\mathrm{daughter\,nucleus}} - 2\,m_{\mathrm{e}}$.

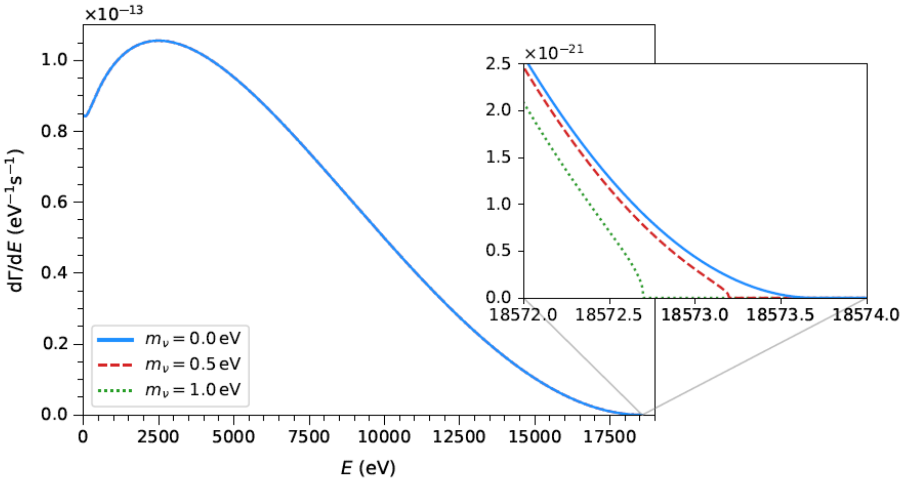

Figure 1.1: Differential β spectrum of tritium, for different neutrino mass values. The impact of the neutrino mass on the spectral shape is most prominent close to the endpoint at 18.6 keV. Figure taken from [152].

2. Effective Field Theory of Neutrino Interactions

Effective Field Theories (EFTs) are widely applied to search for new physics phenomena. This chapter lays out the basic concept of EFTs in general (section 2.1) and as a SM extension with respect to neutrinos (section 2.2). Thereafter, in section 2.3, the focus is set on a specific EFT, describing additional interactions to the Fermi-interaction, the so-called General Neutrino Interactions (GNI). Section 2.4 elaborates on how the GNI can be connected to the high-energy Standard Model Effective Field Theory (SMEFT), while sections 2.5 and 2.6 explore the theoretical origins and experimental testability of GNI, respectively.

2.1 Effective Field Theories

In Quantum Field Theory (QFT), a theory is regarded as fundamental if it is renormalizable. The overreaching objective of this concept is to formulate a single theory that can consistently describe physical processes across all energy scales. The Ultra Violet (UV) completion of a theory to accurately capture high-energy processes is commonly challenging. Therefore, it is often more advantageous to work with an effective description that introduces a new effect at a specific, lower energy scale. This approach can be regarded as a practical intermediate step in constructing a new, UV complete theory.

To provide a more comprehensive understanding of the theoretical concept, we will briefly outline a historical example: The electromagnetic interaction is well described by the U(1) gauge group, which couples photons to electrons (and positrons) within a renormalizable theory. However, to also be able to describe nuclear β decay, this theory must be extended by an electron neutrino taking part in a Fermi-interaction term of mass dimension 6. In other words, the extension makes the theory non-renormalizable. Subsequent discoveries confirmed the already existing theory, that UV completion can be achieved by associating the Fermi constant G_F with the mass of the mediator particle, identified as the W boson, thereby establishing the fundamental theory of electroweak interactions.

Generalising this concept for model-independent searches of new physics, one can formulate an extension of the renormalizable Lagrangian $\mathcal{L}_\mathrm{ren}$. This is achieved by expanding the theory in mass dimension, encompassing all possible combinations of operators that can be constructed from known particles Φ and that obey the symmetries observed at an energy scale μ:

$$\mathcal{L}_\mathrm{eff} = \mathcal{L}_\mathrm{ren}(\Phi) + \sum_{n\geq 5} \sum_{i} \frac{1}{\Lambda^{n-4}} C_i^{(n)} \mathcal{O}_i^{(n)}(\Phi). \tag{2.1}$$

Λ is the unknown mass scale, $C_i^{(n)}$ the dimensionless Wilson coefficients of the operators $\mathcal{O}_i^{(n)}$. The theory provides a reliable description of new physics for $\mu \ll \Lambda$. The expansion of the theory increasingly suppresses terms of higher mass order, and thus, a sufficiently exact description can be reached by cutting off the expansion at a fixed order n. This work focuses on the terms up to mass dimension 6, which suffices to test the leading order contributions of new physics. The Wilson coefficients are expressed in terms of the Fermi coupling, such that they are comparable to the strength of the weak interaction, therefore assuming $\Lambda^{-2} = \sqrt{8}G_\mathrm{F}$.

2.2 Neutrino extended Standard Model Effective Field Theory

The mass scale μ at which the EFT is to be constructed determines the fields and gauge symmetries that must be considered. The high-energy SMEFT is constructed from the full SM gauge group $\mathrm{SU(3)_C \times SU(2)_L \times U(1)_Y}$, since $\mu \gtrsim m_\mathrm{W}$. EFTs operating below the mass scale of the W boson ($\mu \lesssim m_\mathrm{W}$) use the reduced $\mathrm{SU(3)_C \times U(1)_{em}}$ gauge group. Thus, at different energy scales, the fermions are defined in different representations and their interactions are described by different EFTs. Connections between low- and high-energy descriptions can be derived by a so-called mapping, as described in section 2.4.

The SMEFT Lagrangian, constructed from the SM fields and full SM gauge group, can be written as

$$\mathcal{L}_\mathrm{SMEFT}(\Phi_\mathrm{SM}) = \mathcal{L}_\mathrm{SM}(\Phi_\mathrm{SM}) + \sum_{n\geq 5} \sum_i \frac{1}{\Lambda^{n-4}} C_i^{(n)} \mathcal{O}_i^{(n)}(\Phi_\mathrm{SM}). \tag{2.2}$$

The only operator at mass dimension 5 is the Weinberg operator [213], as introduced in section 1.4 equation 1.8. The expansion at mass dimension 6 comprises 59 independent baryon number-conserving operators, listed in [122], which can be categorised into four-fermion operators, two-fermion operators with additional Higgs boson or gauge field-strength tensor contributions, and terms without any fermions. The latter are not of interest to this work, since the focus is the study of neutrino interactions. Furthermore, the SMEFT is expanded by right-handed sterile neutrinos $\mathrm{N_R}$, to in total allow for the existence of Majorana neutrinos through the Weinberg operator, as well as the generation of Dirac-type neutrinos through pairing the SM left-handed neutrinos with the additional right-handed neutrinos.

2.3 Theory of General Neutrino Interactions

The theory of General Neutrino Interactions (GNI) is an EFT below the weak scale and can be considered as a subset of the Low-Energy Effective Field Theory (LEFT) [139]. Therefore, it is constructed under the reduced gauge group, only taking into account light fermions, photons, gluons and sterile neutrinos N with $m_N < m_W$. The theory includes all possible Lorentz-invariant operators for four-fermion interactions involving at least one neutrino. With this approach, the GNI Lagrangian for charged-current interactions can be expressed as

$$\mathcal{L}_\mathrm{GNI}^\mathrm{CC} = -\frac{G_\mathrm{F} V_{\gamma\delta}}{\sqrt{2}} \sum_{j=1}^{10} \left(\overset{(\sim)}{\epsilon}_{j,\mathrm{ud}}\right)^{\alpha\beta\gamma\delta} \left(\bar{\mathrm{e}}_\alpha \mathcal{O}_j \nu_\beta\right) \left(\bar{\mathrm{u}}_\gamma \mathcal{O}'_j \mathrm{d}_\delta\right) + \mathrm{h.c.}, \tag{2.3}$$

Table 2.1: Definition of general neutrino interaction coupling constants and operators appearing in $\mathcal{L}_{\mathrm{GNI}}^{\mathrm{CC}}$ in equation 2.3.

j	ϵ_j	$\mathcal{O}_j$	$\mathcal{O}'_j$
1	ϵ_{L}	$\gamma_\mu(\mathbb{1}-\gamma^5)$	$\gamma^\mu(\mathbb{1}-\gamma^5)$
2	$\tilde{\epsilon}_{\mathrm{L}}$	$\gamma_\mu(\mathbb{1}+\gamma^5)$	$\gamma^\mu(\mathbb{1}-\gamma^5)$
3	ϵ_{R}	$\gamma_\mu(\mathbb{1}-\gamma^5)$	$\gamma^\mu(\mathbb{1}+\gamma^5)$
4	$\tilde{\epsilon}_{\mathrm{R}}$	$\gamma_\mu(\mathbb{1}+\gamma^5)$	$\gamma^\mu(\mathbb{1}+\gamma^5)$
5	ϵ_{S}	$(\mathbb{1}-\gamma^5)$	$\mathbb{1}$
6	$\tilde{\epsilon}_{\mathrm{S}}$	$(\mathbb{1}+\gamma^5)$	$\mathbb{1}$
7	$-\epsilon_{\mathrm{P}}$	$(\mathbb{1}-\gamma^5)$	γ^5
8	$-\tilde{\epsilon}_{\mathrm{P}}$	$(\mathbb{1}+\gamma^5)$	γ^5
9	ϵ_{T}	$\sigma_{\mu\nu}(\mathbb{1}-\gamma^5)$	$\sigma^{\mu\nu}(\mathbb{1}-\gamma^5)$
10	$\tilde{\epsilon}_{\mathrm{T}}$	$\sigma_{\mu\nu}(\mathbb{1}+\gamma^5)$	$\sigma^{\mu\nu}(\mathbb{1}+\gamma^5)$

where $\mathcal{O}_j^{(\prime)}$ are operators describing each new kind of interaction j, listed in table 2.1. ϵ_j and $\tilde{\epsilon}_j$ are the flavour-space tensors, expressing the strength of interaction j with respect to the Standard Model Fermi interaction and are expected to be small. $V_{\gamma\delta}$ denotes the CKM matrix elements and G_{F} is the Fermi constant. Greek indices run over flavour. The neutral-current Lagrangian can be written down in an analogous way [61].

An alternative parametrisation for the 10 interaction terms is the Lee-Yang parametrisation [154], utilising coefficients C and D. This notation exists in parts of the literature and can be related to the ϵ coefficients by linear combination.

All operators related to the $\tilde{\epsilon}$ coefficients contain right-handed projection operators acting on the neutrino field. Thus, the existence of right-handed neutrinos is required for these terms not to vanish. This equally holds for the operators related to ϵ_{S}, ϵ_{P}, and ϵ_{T}, as their operator structure requires opposite-chiral fields. All remaining operators are consistent with SM neutrinos and are commonly investigated within the Neutrino Non-Standard Interactions (NSI) framework [88, 176, 98, 79, 30].

As no assumption is made regarding the mechanism generating the neutrino mass, heavier neutrinos with masses of up to the mass of the W boson are also accounted for in the theory. Similarly, the theory imposes no assumptions regarding the Dirac or Majorana nature of neutrinos. Therefore, any type of right-handed neutrino introduced in section 1.4 can in principle be realised.

2.4 Matching Relations

EFTs above and below the weak scale can be connected via matching relations of their Wilson coefficients and evolution of their renormalization group. This so-called mapping of for example low-energy GNI terms onto dimension-6 (sterile-neutrino extended) Standard Model Effective Field Theory (SM(N)EFT) operators allows for the description of new physics above the weak scale. Assuming a common high-energy origin of new physics allows to set strong indirect constraints on the GNI couplings from existing constraints on the SM(N)EFT couplings, such as in the case for $\epsilon_{\mathrm{S,\,ud}}$ which can be related to the already strongly constrained Wilson coefficients C_{elqd} and C_{eluq} [61]:

$$-\epsilon^{\alpha\beta\gamma\delta}_{\mathrm{S,\,ud}}\,(\bar{\mathrm{e}}_\alpha(\mathbb{1}-\gamma^5)\nu_\beta)(\bar{\mathrm{u}}_\gamma\mathbb{1}\mathrm{d}_\delta) \Leftrightarrow \frac{1}{V_{\gamma\delta}}(V_{\gamma\nu}C^{\alpha\beta\nu\delta}_{elqd}+C^{\alpha\beta\gamma\delta}_{eluq})\,(\bar{\mathrm{e}}_\alpha(\mathbb{1}-\gamma^5)\nu_\beta)(\bar{\mathrm{u}}_\gamma\mathbb{1}\mathrm{d}_\delta). \quad (2.4)$$

The presence of low-energy GNI contributions without a matching counterpart at dimension 6 (such as $\epsilon_{\mathrm{R,\,ud}}$ and $\tilde{\epsilon}_{\mathrm{L,\,ud}}$) may indicate the existence of low-energy new physics or the necessity of expanding the EFT to a higher order [61]. Furthermore, some SMEFT Wilson coefficients correspond to the simultaneous generation of two kind of neutrino interactions at low energies. The detection of such two neutrino interactions would strongly indicate the existence of the underlying SMEFT operator. The matching relations between LEFT and SMEFT are given in [139]. When comparing physics at different energy scales, both the strong energy scale dependency of the couplings [61, 76] and possible energy-dependent mixings among the GNI operators [119] must be taken into account.

2.5 Theoretical Origins of novel Neutrino Interactions

There are several ways to UV complete different GNI scenarios by describing their high-energy origin. Here, theoretical examples are given to explain possible findings of neutrino interactions in β-decay processes. However, only experiments can determine the validity of such a theoretical model by testing further predictions of this model corresponding to other physical processes.

Leptoquarks: Leptoquarks are particles that carry both lepton (L) and baryon number (B), and thus naturally arise in grand unified theories [179]. They offer a potential explanation to the observed mild tension of precision flavour observables and the SM expectation, as seen in B meson decay [49, 51, 34, 131], and are an interesting candidate for a radiative neutrino mass generation mediator [40, 85, 71, 128, 147]. Assuming leptoquarks to function as heavy mediators, they are able to introduce GNI already at tree-level. The various types of leptoquarks can be categorised in groups: those with fermion number $F = 3B + L = 0$ and $F = 2$, and those that possess a scalar and vector-like nature. The nomenclature for different types of leptoquarks is taken from [61, 67]. Each type of leptoquark can be associated with a set of SM(N)EFT Wilson coefficients, which can in turn be connected with the GNI couplings via the matching relations given in [61]. A selection of leptoquark models with their corresponding dimension-6 SM(N)EFT operators and GNI couplings is given in table 2.2. These models are further investigated in section 7.5. The combination of the R_2' leptoquark with one other scalar colour-triplet leptoquark S_1 is of particular interest as it is able to explain B-physics anomalies [69], and can generate radiative neutrino masses at one-loop level [147].

Charged Higgs: Following the discovery of the Higgs boson, a number of extensions of the Higgs sector have been proposed. This work focuses on a minimal charged Higgs model [217, 73], which has been studied in the context of neutrino interactions in [58, 36, 215, 62]. Scalar extensions of the SM have the capacity to generate new neutrino interactions, either in a similar manner to the type-II see-saw mechanism or through one-loop processes. In either scenario, the charged Higgs must be considerably heavy to evade existing stringent

Table 2.2: Selection of leptoquark models. The dimension-6 SM(N)EFT operators that can be generated by these leptoquarks and via the matching corresponding GNI couplings of the β decay ($\epsilon_{\mathrm{X}} = \epsilon^{\mathrm{ee11}}_{\mathrm{X,\,ud}}$ as defined in equation 2.3) are given. Based on [61].

Type	F	Spin	$\mathrm{SU(3)_C}$	$\mathrm{SU(2)_L}$	$\mathrm{U(1)_Y}$	Dimension-6 SM(N)EFT Operators	GNI couplings
S_1	-2	0	$\bar{3}$	1	2/3	$\mathcal{O}_{lNqd}$, $\mathcal{O}'_{lNqd}$, $\mathcal{O}_{eluq}$, $\mathcal{O}_{eNud}$	$\tilde{\epsilon}_S$, $\tilde{\epsilon}_P$, $\tilde{\epsilon}_T$, $\tilde{\epsilon}_R$, ϵ_S, ϵ_P
R'_2	0	0	3	2	1/3	$\mathcal{O}_{lNqd}$, $\mathcal{O}'_{lNqd}$	$\tilde{\epsilon}_S$, $\tilde{\epsilon}_P$, $\tilde{\epsilon}_T$

constraints on charged scalars. The detection of charged-current scalar neutrino interaction may provide evidence for the existence of a charged Higgs.

Right-handed W boson: The W boson, which is known to mediate the β decay, has been observed to couple exclusively to left-handed fermions; the underlying reason for this parity non-conservation remains unclear. However, a left-right symmetry can be introduced by incorporating right-handed neutrino states into the theoretical framework, alongside proposing the existence of a right-handed vector-current interaction, which may be mediated by a right-handed W boson [169, 170]. This results in an expansion of the electroweak gauge group by the $\mathrm{SU(2)_R}$ group. The hitherto absent observation of a right-handed W boson can be explained in the context of a unified gauge theory extending the electroweak gauge group: The parity non-conservation is regarded as a low-energy phenomenon caused by spontaneous symmetry breaking. Parity conservation is restored at high energies, and the corresponding large mass of the right-handed W boson acts as a suppression factor on the interaction. Thus, this left-right symmetric approach has the capacity to provide a direct explanation for the existence of small neutrino masses via this suppression mechanism. The right-handed charged currents of the right-handed W boson can be probed with the GNI framework.

2.6 Experimental Tests of novel Neutrino Interactions

There exist a multitude of interaction channels through which new neutrino interactions may emerge, each characterised by their own set of GNI coupling constants ϵ (see equation 2.3). The following section provides an overview of the experimental approaches that enable to probe the existence of these interactions. The experimental approaches differ in terms of the combination of couplings that is constrained and of the energy scale at which the new interactions are probed. The following overview is predominantly centred on low-energy experimental approaches of up to a few GeV, while also offering insights into high-energy investigations. For any of the approaches, no assumption on the origin of the GNI is imposed. Further details can be found in [60, 61, 98].

Neutrino oscillations: It has been established that neutrinos propagating through matter exhibit a different dispersion relation compared to their propagation in vacuum. This is due to their charged-current interactions of the electron neutrinos with the electrons in the matter. These occur additional to the flavour-universal neutral-current interactions. This phenomenon is known as the Mikheyev–Smirnov–Wolfenstein (MSW) effect [114, 113]. The expansion of the charged-current interactions through the introduction of GNI further modifies the dispersion relation [64]. These modifications can directly impact the neutrino oscillation parameters and their impact increases with the propagation path through matter. It is predicted that the upcoming long-baseline experiments T2HK [5] and DUNE [9], with path lengths through the earth of 300 km and 1300 km, respectively, will be sensitive to these modifications of the dispersion relation; neglecting their potential influence may result in an inaccurate inference of the oscillation parameters [156, 157, 135]. However, only left- and right-handed vector-like interactions and only differences between the lepton families can be constrained by the oscillation experiments themselves [55, 98]. Consequently, complementary tests of GNI are needed to ascertain the correct inference of the neutrino oscillation parameters.

Lepton Flavour Violation (LFV) in μ and τ decays: LFV terms appear in the SMEFT. By mapping SMEFT lepton flavour changing Wilson coefficients to the GNI, existing strong constraints on LFV processes can be utilised to indirectly constraint the respective interaction channels of the GNI. Muon-flavour to electron-flavour transitions are constrained by the SINDRUM experiment [68, 54], the SINDRUM-II experiment [56, 101], and the MEG experiment [45, 68]; tau-flavour to muon-flavour or electron-flavour transitions are constrained by the Belle experiment [68, 130]. The corresponding constraints on the GNI prove to be about five orders stronger than the existing direct constraints, not taking into account the energy-scale dependency of the couplings [61].

Coherent Elastic Neutrino Nucleus Scattering (CEvNS): The process of CEvNS [105] was first observed by the COHERENT collaboration [26]. It occurs characteristically at small neutrino energies with a large cross section compared to inelastic scattering processes, as the neutrino is scattered on the whole nucleus, rather than on individual nucleons. The experimental challenge is to detect the small nuclear recoil energy of the order of keV. This process can constrain neutral-current GNI, assuming that the couplings are independent of the neutrino flavour. Thus, the results of the COHERENT experiment imply bounds on the GNI, given in [37].

Neutrino-electron scattering: Both the W and the Z boson can mediate neutrino-electron scattering processes, thereby allowing the study of both neutral-current and charged-current new neutrino interactions. The constraints for $\bar{\nu}_\mathrm{e}$-e scattering set by the TEXONO experiment [84], and for $\nu_\mu/\bar{\nu}_\mu$-e scattering from the CHARM-II experiment [209, 210] are investigated in the context of GNI in [191, 47]. More recent studies [144, 72] make use of the measurement of solar neutrinos at the Borexino experiment [13].

β decay: Precision measurements of different properties of the β decay can be utilised to search for charged-current GNI. Thus, global analyses combine properties of β-decay transitions, neutron lifetimes, and neutron decay correlation coefficients to gain sensitivity to these novel interactions [117, 75]. The observables are obtained at decay energies from $\mathcal{O}(100\,\mathrm{keV})$ to $\mathcal{O}(1\,\mathrm{MeV})$, depending on the isotope. In contrast, the novel approach explored in the work at hand (see chapter 7) is characterised by constraining GNI at a very low decay energy of 18.6 keV of the tritium β decay, using the high precision electron spectroscopy of the KATRIN experiment to search for spectral shape modifications.
Complementary high-energy investigations make use of Missing Transverse Energy (MET) processes at the Large Hadron Collider (LHC) at about 8 TeV [174]. These searches provide indirect constraints by matching the Wilson coefficients of a high-energy EFT to the GNI couplings. This approach exhibits noticeable dependencies on the energy scale, which modifies the sensitivity to these coefficients. The strong scale dependence of the couplings

between the markedly disparate energy scales poses a challenge for the comparability between low- and high-energy investigations [76, 61].

3. The KATRIN Experiment

The Karlsruhe Tritium Neutrino experiment (KATRIN) is located at the Karlsruhe Institute of Technology (KIT) at Campus North. Its principal objective is to identify the effective electron anti-neutrino mass with a sensitivity better than 0.3 eV at 90 % CL. In order to achieve this, the KATRIN experiment employs a direct, kinematic measurement approach of the endpoint region of the tritium β-decay spectrum. An overview of the experimental setup is shown in figure 3.1.
KATRIN features a 10^{11} Bq high-activity Windowless Gaseous molecular Tritium Source (WGTS), where the β-electrons are emitted and are magnetically guided through the setup [25] towards the detector. In the KATRIN spectrometer, the electrons' momenta are magnetically collimated and the electrons are electrostatically filtered based on their kinetic energy with a filter width of $\mathcal{O}(1\,\mathrm{eV})$ [50, 159, 181]. Only electrons with sufficient surplus energy over threshold are permitted to pass the spectrometer and are subsequently counted at the detector. The filter threshold is varied in steps of smaller than $\mathcal{O}(1\,\mathrm{eV})$ close to the spectral endpoint E_0 in order to record an integral β-spectrum, with a typical scan duration of about 2.5 hours. The KATRIN collaboration has recently set a new world-leading direct upper limit on the effective electron-antineutrino mass to 0.45 eV at 90 % CL [17].
The following provides further details on the relevant components of the experimental setup, based on [25]. Details on the data analysis and modelling are discussed in chapters 4 and 5.

3.1 Source and Transport Section

A fundamental component of the KATRIN experiment is the 10-m-long and 90-mm-diameter cryogenic WGTS in the source section. Gaseous molecular tritium is injected at the axial centre of the WGTS tube and circulated towards both ends. During this process tritium undergoes continuous, isotropic decay into helium-3, an electron and an electron antineutrino:

$$\mathrm{T}_2 \rightarrow \mathrm{T}\,{}^3\mathrm{He}^+ + \mathrm{e}^- + \bar{\nu}_\mathrm{e}. \tag{3.1}$$

The gas density is reduced by a factor of ∼100 at both ends of the WGTS by Turbo Molecular Pumps (TMP), and the gas is then fed into a cleaning and reinjection cycle [185, 186, 187]. This so-called loop system ensures a constant, stable supply of $> 98\,\%$ pure tritium throughout operation. The tritium purity, as well as the overall gas composition in the source, are under continuous monitoring by the Laser Raman spectroscopy system (LARA) [137, 198]. The cycling and reinjection of tritium enables a nominal column density ρd of $5 \times 10^{21}\,\frac{1}{\mathrm{m}^2}$, that is the number of tritium molecules per area integrated over the length of the WGTS, at a source temperature of 30 K. Typical operation temperatures of the

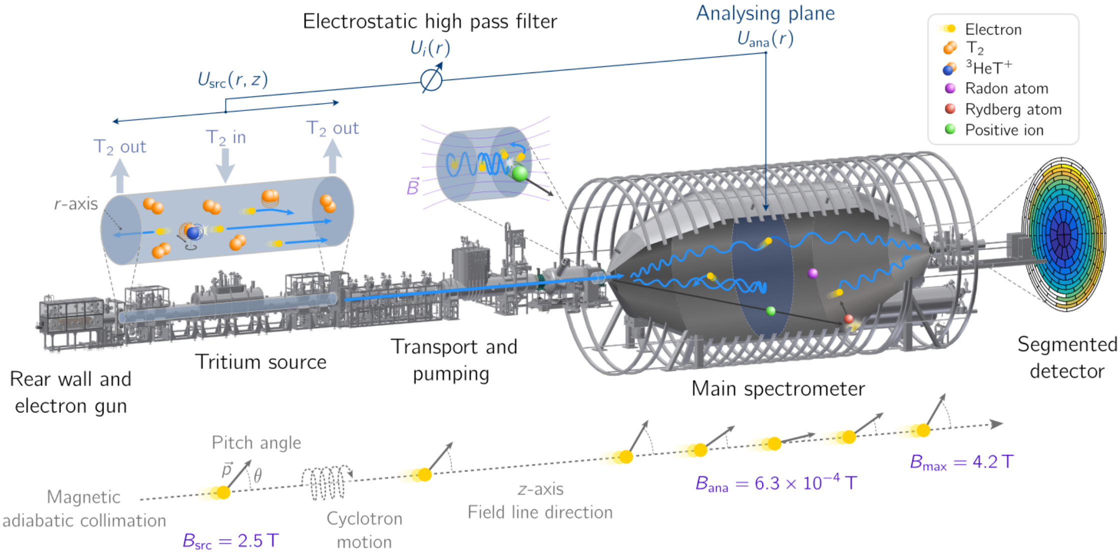

Figure 3.1: The KATRIN experiment. Tritium decays in the source section. The β electrons resulting from this decay are magnetically guided through the experiment towards the detector. Upon arrival at the main spectrometer the electrons are discriminated based on their energy using the Magnetic Adiabatic Collimation with Electrostatic (MAC-E) filter principle. Electrons with sufficient surplus energy pass the main spectrometer and are counted at the detector [25].

WGTS during neutrino-mass measurements are either 30 K or 80 K, which are kept stable at the sub-per-mille level [28]. These low temperatures allow the high tritium throughput necessary to provide a high luminosity of β-electrons due to a low conductance of the source tube. A further advantage of a low-temperature tritium source lies in the reduction of the Doppler broadening of the tritium β spectrum. These configurations providing a high-activity, high-purity, and highly stable tritium source are essential for maximising the experiment's sensitivity to the imprint of the neutrino mass [52].

At the rear of the experiment, the WGTS is terminated by the Rear Wall (RW), a 14.6-cm-diameter gold-coated stainless steel disc. β-electrons emitted in upstream[1] direction are guided along the magnetic field lines within the source of $B_{\mathrm{src}} = 2.51\,\mathrm{T}$ towards the RW and are absorbed on the RW surface. Given that the RW surface is equally exposed to tritium, its gold coating provides chemical inertness [41] and a temporally stable work function [143]. β-electrons heading in downstream direction travel towards the detector. Although some of these electrons can leave the source unscattered, a large fraction undergoes scattering on the neutral gas within the WGTS, leading to energy losses through excitation, ionisation, and dissociation of the molecules. The resulting electron number density allows for the description of the KATRIN source as a low-density, low-temperature plasma, which is influenced by the surface potentials of the RW and beam tube within the WGTS. The application of an external RW bias voltage enables the tuning of the particle dynamics within the source, thereby minimising temporal and spatial inhomogeneities of the electrons' starting potential [151, 164].
The total rate of β electrons on the RW of around $10^{11}\,\mathrm{e}^-/\mathrm{s}$ is monitored by the Beta

---

[1] "Upstream" indicates the direction towards the rear wall, whereas "downstream" refers to the direction towards the detector.

Induced X-ray Spectroscopy (BIXS) system, located in the pump ports in front of the RW. This enables the assessment of the source stability by detecting the characteristic X-ray line spectrum emitted by electrons penetrating the RW surface using two X-ray sensors [25].
A key subsystem employed for a variety of calibration measurements, including the calibration of magnetic fields, column density, and energy loss characteristics within the WGTS, is the high-resolution angular-selective, quasi-monoenergetic photoelectron source [134, 216, 53, 97, 197]. This so-called electron-gun (e-gun) is located behind the RW and supplies the experiment with a fine beam of electrons with adjustable pitch angle, electron energies up to 32 keV and rates of more than 10^4 counts per second (cps) through a centre hole in the RW [204].

In the downstream direction, a transport section adjoins the WGTS. Equipped with two pumping stages, this section enables the transition to an ultra-high vacuum. This, in turn, facilitates a loss-free electron transport from the source to the spectrometer and detector. First, the Differential Pumping Section (DPS) provides a pressure reduction of five orders of magnitude through the use of TMPs and custom hardware configurations; a chicane slows down neutral gas components, while dipole electrodes block ions [25, 148]. In a subsequent step, the Cryogenic Pumping Section (CPS) employs cryosorption of tritium on an argon frost layer to further reduce the pressure by seven orders of magnitude [25, 193]. This pumping stage also accommodates the Forward Beam Monitor (FBM), a movable seven-pixel Silicon Drift Detector (SDD) that measures the electron flux intensity at different locations in the beam tube and thereby monitors the source activity [129, 92, 52, 150].

3.2 Spectrometer and Detector Section

Subsequent to the transport section, the β-electrons enter the spectrometer section, consisting of a pre- and a main spectrometer. The pre-spectrometer served as a pre-filter blocking low-energy electrons during the first four measurement campaigns up until October 2020. It was known that the electromagnetic field settings of the pre- and main spectrometer caused an inter-spectrometer Penning trap, accumulating scattered electrons and thus leading to a time-dependent background. A conductive wire cleared the Penning trap in regular intervals [15]. The penning background was mitigated during measurement campaign four by setting the pre-spectrometer to ground potential during normal operation [184, 208].

The main spectrometer is one of the most crucial components of the KATRIN experiment, serving as a high-precision energy filter for keV electrons. For this purpose it employs, equally to the pre-spectrometer, the MAC-E filter principle [50, 159, 181]. By lowering the magnetic field within the high-vacuum spectrometer vessel by four orders of magnitude, the electrons' momenta are collimated in forward direction, as visualised in figure 3.1. Then, an electrostatic retarding potential serves as a high pass filter, thereby slowing down the electrons. Only electrons with sufficient surplus energy can pass the filter and are counted at the detector. All other electrons are reflected by the electromagnetic fields and eventually absorbed at the RW. The plane within the spectrometer vessel at which maximum collimation and maximum retardation coincide is referred to as the analysing plane. The magnetic field strength in the analysing plane B_{ana} in relation to the strongest magnetic field, the pinch magnetic field B_{pch} at the downstream end of the main spectrometer, defines the energy resolution of the experimental setup [145]:

$$\frac{\Delta E}{E} = \frac{B_{\text{ana}}}{B_{\text{pch}}} \frac{\gamma + 1}{2} \,. \tag{3.2}$$

γ is the Lorentz factor. The filter width ΔE accounts to 2.8 eV for the magnetic field settings during the first two measurement campaigns. A large volume air coil system, consisting of the Earth Magnetic field Compensation System (EMCS) and Low-Field Correction System (LFCS), surrounds the 23 m long and 10 m diameter main spectrometer and fine shapes the magnetic field inside the vessel [116, 25, 97, 94]. Studies have shown that there exists a trade-off between a low magnetic field in the analysing plane, which enables high resolution, and higher fields, which reduce background electron rates [161]. Further hardware configurations of the main spectrometer aid in maintaining a low background rate [**Harms2015**, 120]: Wire electrodes covering the inside surface of the spectrometer vessel are set to -200 V relative to the vessel potential and thereby repel electrons coming from the vessel surface. Nitrogen-cooled cryogenic baffles in the pump ports of the Non-Evaporating Getter pumps (NEG) hinder the emanation of ^{219}Rn from the NEG materials into the 10^{-11} mbar ultra-high vacuum within the main spectrometer vessel.

Only electrons with an initial pitch angle of up to the maximum acceptance angle

$$\theta_{\text{max}} = \arcsin\left(\sqrt{\frac{B_{\text{src}}}{B_{\text{pch}}}}\right) \,. \tag{3.3}$$

are permitted to traverse the entire beamline and may be counted at the detector; any electrons with a higher pitch angle are eventually reflected by the magnetic mirror effect. Given that a larger pitch angle is associated with a longer path length of the electrons in the spectrometer, and therefore with an increase in both scattering probability and synchrotron radiation, θ_{max} can be utilised to optimise the energy loss of the electrons. An optimised setting is reached at $\theta_{\text{max}} = 51^\circ$.

Finally, all electrons that meet the transmission conditions are counted at the Focal Plane Detector (FPD) [31], a 90 mm in diameter monolithic silicon wafer comprising 148 concentric pixels of equal surface area. Each pixel functions as a PIN diode, which is connected to custom read-out electronics and the Data Acquisition (DAQ) system. A γ- and an e^--source, situated in the detector section, allow for dedicated calibration measurements of the FPD [31]. External backgrounds are addressed by an active muon veto consisting of plastic scintillators, combined with a passive lead and copper shielding. The detection efficiency is optimised by accelerating the electrons within the detector section by 10 kV with the Post Acceleration Electrode (PAE), which allows the detection in a region with lower intrinsic detector background and reduces backscattering and dead layer losses on the FPD surface due to the decreased pitch angle.

4. Physics Model

The experimental conditions and physical effects that influence the propagation of the β electrons through the experiment and the rate counted at the detector must be modelled accurately in order to correctly infer the signal from the neutrino mass or BSM physics. This chapter provides an introduction to the derivation of the theoretical differential and experimental integral β spectrum in sections 4.1 and 4.2, respectively. Subsequent sections then describe further systematic contributions related to the source (section 4.3) and the detector (section 4.4).

4.1 Differential Tritium β-Decay Spectrum

Tritium undergoes radioactive decay into helium, releasing an electron and an electron antineutrino, as introduced in equation 3.1. The differential decay rate can be obtained directly by applying Fermi's golden rule [100] and a detailed derivation can be found in [177]. In natural units, the decay probability from initial (i) to final state (f) in first-order perturbation is expressed as follows:

$$\Gamma_{i \to f} = 2\pi | \langle f | \mathcal{M} | i \rangle |^2, \tag{4.1}$$

where the transition matrix element $|\mathcal{M}_{fi}|$ includes leptonic and nuclear transitions. The resulting differential tritium β-decay rate [145]

$$\begin{aligned} \frac{\mathrm{d}\Gamma}{\mathrm{d}E} =& \frac{G_\mathrm{F}^2 V_\mathrm{ud}^2}{2\pi^3} F(E,\, 2) |\mathcal{M}_\mathrm{nucl}|^2 \sqrt{(E + m_\mathrm{e})^2 - m_\mathrm{e}^2}(E + m_\mathrm{e}) \\ &\cdot \sum_j \zeta_j \varepsilon_j \sqrt{\varepsilon_j^2 - m_\upbeta^2}\, \Theta(\varepsilon_j - m_\upbeta) \end{aligned} \tag{4.2}$$

is composed of the Fermi function, $F(E,\, 2)$, which models the electromagnetic interaction of the emitted electrons with the daughter nucleus, and the nuclear transition matrix $\mathcal{M}_\mathrm{nucl}$ with the coupling structure $|\mathcal{M}_\mathrm{nucl}|^2 = g_\mathrm{V}^2 + 3g_\mathrm{A}^2$. V refers to vector-like and A to axial vector-like interactions. The electrons' kinetic energy is denoted by E and their mass by m_e. $m_\upbeta$ is the neutrino mass, introduced in equation 1.15. The Heavyside step function Θ ensures energy-momentum conservation. The differential β spectrum is illustrated in figure 1.1. In addition, this formula already contains several corrections specific to the KATRIN set-up:

To reflect the fact that KATRIN uses molecular tritium, which can exhibit molecular excited states after the β decay, the effect of these molecular final states is taken into account by including the molecular excitation energy, V_j, which reduces the available neutrino energy according to $\varepsilon_j = E_0 - E - V_j$ [145]. The probability of producing the excited state j is expressed by ζ_j. The corresponding molecular Final-States Distribution (FSD), describing the excitation probability of each final state over the energy, incorporates recoil excitations of rotational and vibrational final states, in addition to excitations of the electron shells [89, 90, 194, 195].

Furthermore, radiative corrections $G_{\mathrm{rad}}(E, E_0)$ for the contributions coming from both real and virtual photons during the decay, derived for tritium β decay in [190], are taken into account, while further theoretical corrections are neglected [145].

Other contributions to this spectrum, describing different contributions of new physics [20, 24, 24, 153], can be added. The corrections necessary to study GNI are derived and introduced in section 7.1.

4.2 Integral β-Decay Spectrum

The integral β spectrum measured at the detector is a composition of the differential β spectrum and the experimental response function, which reflects the transmission properties and physical effects of the experimental setup. This section provides a concise overview of the integral spectrum's composites.

4.2.1 Transmission function

The probability for isotropically generated electrons to be transmitted by the MAC-E filter is described by the transmission function [121, 95, 16, 145]:

$$\begin{aligned} T(E, qU_0) &= \int_0^{\theta_{\max}} \mathcal{T}(E, \theta, U_i) \sin\theta \mathrm{d}\theta \\ &= \begin{cases} 0 & \text{if} \quad E - qU_0 < 0 \\ 1 - \sqrt{1 - \frac{E - qU_0}{E} \frac{B_{\mathrm{src}}}{B_{\mathrm{ana}}} \frac{2}{\gamma + 1}} & \text{if} \quad 0 \leq E - qU_0 \leq \Delta E \\ 1 - \sqrt{1 - \frac{B_{\mathrm{src}}}{B_{\max}}} & \text{if} \quad E - qU_0 > \Delta E \end{cases} \end{aligned} \tag{4.3}$$

with $\mathcal{T}$ being the transmission condition and $E - qU_0$ the surplus energy of the electrons above the filter threshold. The transmission function is represented by a broadened step function; the width is due to partly uncollimated momenta of the electrons in the analysis plane, which the MAC-E filter is not sensitive to and thus connected to the energy resolution defined in equation 3.2. Furthermore, the transmission function depends on the electrons' emission angle θ_{src} in the source and the acceptance angle $\theta_{\max}$ defined in equation 3.3. Consequently, other electron sources, such as the e-gun, exhibit a characteristic transmission function [197].

4.2.2 Response Function

As an extension of the transmission function $T(E, qU_0)$, a response function $f(E, qU_i)$ can be defined to encompass further influences on the electrons' energy spectrum after their generation in the source, thus giving the probability for electrons to reach the detector when propagating through the experiment. The response function reads

$$f(E, qU_i) = \int_{\epsilon=0}^{E-qU} \int_{\theta=0}^{\theta_{\max}} \mathcal{T}(E-\epsilon, \theta, qU_i) \sin\theta \sum_s P_s(E) f_s(\epsilon) \mathrm{d}\theta \mathrm{d}\epsilon. \tag{4.4}$$

The most relevant effects that are taken into account by this function are energy loss processes from inelastic electron-tritium scattering in the WGTS and synchrotron radiation, and an energy broadening caused by the Doppler effect [133]. The energy loss through scattering is denoted by ϵ; the transmission condition $\mathcal{T}$ is accordingly shifted by this value. The scattering probability P_s for a certain pitch angle and starting position is approximated by a Poisson distribution depending on the column density and the energy dependent scattering cross section [145]. The energy-loss function f_s describes the electrons' probability to lose the energy ϵ after s-fold scattering [23, 2, 38] and is obtained by in-situ e-gun measurements [23].

4.2.3 Integrated Rate

The combination of the aforementioned differential β spectrum $\frac{\mathrm{d}\Gamma(E)}{\mathrm{d}E}$ and experimental response function $f(E, qU_i)$ through convolution, results in the measured integral rate for each retarding voltage setpoint qU_i:

$$R(qU_i) = A_\mathrm{s} N_\mathrm{T} \int\limits_{qU_i}^{E_0} \frac{\mathrm{d}\Gamma(E)}{\mathrm{d}E} f(E, qU_i) \mathrm{d}E + R_\mathrm{bg}(qU_i). \tag{4.5}$$

N_T serves as a signal renormalization factor for the normalized amplitude A_s and is based on the number of tritium atoms in the source, the maximum acceptance angle due to the magnetic field design, and the detection efficiency (see section 4.4). $R_\mathrm{bg}(qU_i)$ is the background rate. In the neutrino-mass analysis, the amplitude A_s, the endpoint E_0, and a constant background component $R_\mathrm{bg}^\mathrm{base}$ are treated as nuisance parameters.

4.2.4 Background Components

The background rate in equation 4.5 is comprised of a constant rate component, a qU-dependent contribution stemming from the spectrometer and detector, a scan-step-dependent contribution arising from an inter-spectrometer Penning trap, and an additional component originating from the RW:

$$R_\mathrm{bg}(qU_i) = R_\mathrm{bg}^\mathrm{base} + R_\mathrm{bg}^\mathrm{slope}(qU_i) + R_\mathrm{bg}^\mathrm{penning}(t(qU_i)) + R_\mathrm{bg}^\mathrm{RW}(qU_i). \tag{4.6}$$

The constant rate $R_\mathrm{bg}^\mathrm{base}$ is the primary background component and is to a large extent constrained by the measurement points above the endpoint. It is predominantly influenced by the surface conditions of the spectrometer and the intrinsic background of the detector [81]. On the spectrometer surface, ^{210}Pb is implanted, which produces ^{210}Po in its decay chain. Subsequently, ^{210}Po undergoes α decay; the recoiling ^{206}Pb can sputter off the spectrometer walls and thereby produce highly excited neutral Rydberg atoms, which isotropically distribute in the spectrometer volume. The subsequent ionisation of the

Rydberg states by black body radiation and auto-ionisation results in the production of an isotropic very low-energy electron background [104, 126, 207, 35, 81].

Dedicated measurements revealed a slightly retarding-energy-dependent background contribution $R_{\mathrm{bg}}^{\mathrm{slope}}(qU_i)$ with a slope of the order of 1 milli count per second per keV. This background component results from different transmission and detection probabilities for background electrons [126, 207, 81].

An additional non-Poissonian background component is accounted for by increasing the statistical uncertainty of the background rate. This contribution arises from radioactive decays, mainly of ^{219}Rn, producing keV-scale electrons that become trapped in the electromagnetic fields of the main spectrometer. Scattering processes and thus energy losses on residual atoms generate correlated populations of secondary electrons of up to 100 events arriving at the detector within 1000 s intervals, leading to a non-Poissonian overdispersion of the detected rate [103, 167]. This background component was eliminated in later campaigns by a redesign of the electromagnetic field setting, that changed the background-electron storage conditions [22].

The scan-step-dependent Penning background $R_{\mathrm{bg}}^{\mathrm{penning}}(t(qU_i))$ originates from the inter-spectrometer Penning trap situated between the pre- and main spectrometer, which accumulates electrons over time. These electrons subsequently generate ions through scattering processes, which can travel into the spectrometer, thereby creating a low-energy background. The scan-step dependence is caused by an emptying of the Penning trap between each scan step [184, 208]. In later campaigns, this background component was eliminated by setting the pre-spectrometer to a small voltage of $-100\,\mathrm{V}$ [17].

Finally, residual tritium ions accumulate on the RW over time, resulting in a second RW β spectrum superimposed on the main β spectrum of gaseous tritium in the source. Despite the low activity of the RW spectrum in comparison with that of the source, this background component must be considered within the model. For this reason, dedicated measurements with an empty source are performed to characterise the RW spectrum in terms of its amplitude, endpoint and FSD [**aker**, 17].

4.3 Source Potential Effects

In addition to the aforementioned description of the integral β-spectrum rate, source effects must be taken into account. Deviations from a constant electric starting potential for the β electrons in the source result in a modification of the detected spectral shape, thereby introducing a bias on the neutrino mass observable Δm^2. Possible temporal and spacial variations in the starting potential result in a broadening σ of the spectrum. Furthermore, the asymmetry parameter Δ_{P} reflects the difference in starting potential distribution for different scattering multiplicities of the electrons. The majority of unscattered electrons originate from the front of the source section, closer to the spectrometer, while s-fold scattered electrons mainly originate from the rear of the source. Due to the asymmetric nature of the starting potential, different scattering multiplicities experience, on average, a different starting potential. The knowledge of σ and Δ_{P} directly allows the quantification of the neutrino mass bias Δm^2 [164, 151]. Therefore, dedicated calibration measurements with co-circulated ^{83m}Kr have been performed. Both σ and Δ_{P} can be inferred from the quasi-monoenergetic krypton-electron N line spectrum. However, krypton-specific systematic effects have thus far overshadowed the spectral region from which Δ_{P} is obtained; thus a maximum limit based on σ is used [164]. A re-evaluation of the data will enable a precise determination of both source potential observables once the relevant systematic effects have been determined through ongoing dedicated investigations [11].

4.4 Detection Efficiency

The detected count rate of the integral β spectrum is furthermore dependent on detector effects. The FPD counts the by the post-acceleration electrode to around 28 keV accelerated electrons with 95 % detection efficiency [31, 200]. The 3-keV FWHM energy resolution permits a region-of-interest cut between 14 keV and 28 keV in the first two measurement campaign to enhance the signal-to-background ratio. This cut has been further optimised in subsequent campaigns. However, the region-of-interest cut influences the detection efficiency and thus necessitates consideration within the model: At low retarding voltages, a high rate of electrons arrives at the detector, causing pile-up effects which likely shift the event outside the region of interest. Furthermore, a significant fraction of electrons is backscattered off the FPD, despite the additional kinetic energy and smaller pitch angle caused by the post-acceleration. The electrons are reflected by the electromagnetic fields and subsequently hit the same or another pixel within a shaping length of 1.6 µs. Notably, backscattered electrons with high surplus energies above a low retarding potential may overcome the retarding potential a second time and escape through the main spectrometer. This effect is investigated through a combination of simulations and dedicated e-gun measurements. The pitch-angle dependency of the backscattering processes is implemented in the model by a modification of the transmission function.

5. Statistical Methods and Analysis Tools

The analytical description of the integral β spectrum, as introduced in the previous chapter, is combined with statistical methods and applied to data in order to interpret the observed count rate. The present chapter first introduces the concept of the Likelihood function, which quantifies the difference between the analytical model under a given parameter set and the observed data (section 5.1). In addition, the concept of the Likelihood function is extended to include systematic and correlation effects (section 5.2). Subsequently, the chapter presents optimisation strategies for identifying the parameter set that best describes the data (section 5.3), in addition to methods of setting limits on parameters of interest (section 5.4). Finally, the KATRIN analysis environment, which combines all methods previously discussed, is introduced in section 5.5.

5.1 The Likelihood Function

The analytical model of the integral β spectrum is fitted to the observed count rate by tuning the model parameters $\vec{\Theta}$. The Likelihood function $\mathcal{L}(\vec{\Theta}|\vec{N}_{\text{obs}})$ quantifies the model's fitness to the data through the likeliness for parameter set $\vec{\Theta}$ to occur, given the observed count rate $\vec{N}_{\text{obs}}$. This formulation is equivalent to the probability $\mathcal{P}(\vec{N}_{\text{obs}}|\vec{\Theta})$ of observing the count rate $\vec{N}_{\text{obs}}$ given the parameter set $\vec{\Theta}$. The calculation of these quantities requires the evaluation of a Probability Density Function (PDF) $f(\vec{N}_{\text{obs}}|\vec{N}_{\text{theo}}(qU_i, \vec{\Theta}))$ at each retarding-energy set point qU_i. $\vec{N}_{\text{theo}}$ is the theoretically predicted count rate of the model. $\vec{\Theta}$ comprises all parameters required to describe the integral spectrum, which are the parameters of interest (e.g. the neutrino-mass observable m_ν^2), the standard nuisance parameters (the amplitude A_{S}, the constant background rate $R_{\text{bg}}^{\text{base}}$, and the kinetic endpoint E_0), in addition to any parameters describing systematic effects. The Likelihood function can then be expressed as follows:

$$\mathcal{L}(\vec{\Theta}|\vec{N}_{\text{obs}}) = \mathcal{P}(\vec{N}_{\text{obs}}|\vec{\Theta}) = \prod_{i=0}^{n} f(\vec{N}_{\text{obs}}|\vec{N}_{\text{theo}}(qU_i, \vec{\Theta})). \tag{5.1}$$

Statistical fluctuations of the probability $\mathcal{P}$ may necessitate an extension of the Likelihood function to non-physical regions for parameters such as m_ν^2. Consequently, a mathematical continuation of the model is implemented. The PDF f is represented by a normal distribution for sufficiently large statistics. Accordingly, the uncertainty can be expressed as:

$$\sigma(N_{\text{theo},i}) = \sqrt{N_{\text{theo},i}}. \tag{5.2}$$

A Maximum Likelihood Estimation (MLE) allows to identify the parameter set $\vec{\Theta}$ that best describes the data. Rather than maximising the Likelihood function, it is common to search for the global minimum of the Pearson's χ^2 statistic [182] due to computational advantages. The Pearson's χ^2 statistic for a normal distribution is given as:

$$\chi^2 = -2\log\mathcal{L}(\vec{\theta}) = \sum_{i=0}^{n}\left(\frac{N_{\text{obs},i} - N_{\text{theo},i}}{\sigma(N_{\text{theo},i})}\right)^2 . \tag{5.3}$$

5.2 Treatment of Systematic Effects

In order to correctly infer the parameters of interest from the data and obtain an unbiased result, it is necessary to precisely model and propagate systematic uncertainties in the analysis. For this purpose, the so-called pull-term approach is used in this work. The total set of parameters, comprising the parameters of interest, the basic nuisance parameters, and the parameters describing systematic effects $\vec{\kappa}$, with $\vec{\bar{\kappa}}$ being their expected mean value, is denoted by $\vec{\Theta}_{\text{total}}$. The additional information on $\vec{\kappa}$ can then be incorporated into the χ^2 function through a pull term:

$$\chi^2 = \chi^2(\vec{\Theta}_{\text{total}}) + \left(\vec{\bar{\kappa}} - \vec{\kappa}\right)\Sigma^{-1}\left(\vec{\bar{\kappa}} - \vec{\kappa}\right)^{\top} . \tag{5.4}$$

The covariance matrix Σ consists of the uncertainties $\sigma_{\kappa,i}$ and the correlation coefficients $\rho_{\kappa,ij}$ with

$$\Sigma_{ii} = \sigma_{\kappa,i}^2 \qquad \& \qquad \Sigma_{ij} = \sigma_{\kappa,i}\cdot\sigma_{\kappa,j}\cdot\rho_{\kappa,ij} \tag{5.5}$$

The uncertainties, correlations and expected mean values for each systematic effect are obtained from calibration measurements.

5.3 Parameter Estimation

Two statistical approaches are commonly utilised to infer the parameters of interest from the comparison between the model prediction and the data: the frequentist and the Bayesian approach.

Frequentist approach: The frequentist approach interprets probability as the relative frequency of the results of many independent events and makes purely data-driven statements on the probability of observing the data given an a-priori fixed Null Hypothesis (NH). The minimum of the χ^2 function χ^2_{min} with respect to $\vec{\Theta}$ corresponds to the identification of the parameter set that provides the most accurate description of the data. For a Gaussian PDF and therefore a parabolic χ^2 function, the parameter uncertainties are given by the Hesse matrix, which is the second derivative of the χ^2 function with respect to the entries of $\vec{\Theta}$. In the event of a slightly asymmetric χ^2 distribution, a more precise method is to scan the distribution over its multi-dimensional parameter space, also called Likelihood profiling. The upper and lower 1-σ uncertainties are then found at $\Delta\chi^2 = \chi^2_{\text{NH}} - \chi^2_{\text{min}} = 1$, following Wilks' Theorem [214].

Bayesian approach: In contrast to the frequentist approach, the Bayesian approach treats parameters and hypotheses as probability distributions, that are compared to a fixed set of data, taking into account a degree of belief or prior knowledge. The probability distribution that reflects the current state of knowledge is termed the prior $\pi(\vec{\Theta})$. Bayes' theorem defines the posterior probability distribution $P(\vec{\Theta}|\vec{N}_{\mathrm{obs}})$ to give the updated probability estimate after combining the prior with the data:

$$P(\vec{\Theta}|\vec{N}_{\mathrm{obs}}) = \frac{\pi(\vec{\Theta})\,\mathcal{L}(\vec{\Theta}|\vec{N}_{\mathrm{obs}})}{p(\vec{N}_{\mathrm{obs}})}. \tag{5.6}$$

The probability $p(\vec{N}_{\mathrm{obs}})$ of observing the count rate $\vec{N}_{\mathrm{obs}}$ functions as a normalisation factor. This approach facilitates the incorporation of current knowledge via the prior; however, it simultaneously implies a potential dependency of the result on the selected prior.

The present work and the following sections are based on a frequentist analysis approach.

5.4 Limit Setting Techniques

Statistical hypothesis testing can be applied to make a statement about the significance of a finding with respect to the null hypothesis H_0. The test hypothesis H_1 is compared to H_0 by the Likelihood ratio $\lambda = \mathcal{L}(\vec{\Theta}_1)/\mathcal{L}(\vec{\Theta}_0)$, where $\vec{\Theta}_i$ is the parameter space of H_i ($i \in \{0,\, 1\}$). For composite hypotheses, where H_1 specifies a set of probability distributions rather than one simple distribution, it is challenging to calculate this ratio directly. Wilks' theorem [214] allows to approximate λ with the χ^2 function following $\chi^2 \approx -2\log\lambda$ for large samples and unbounded parameter spaces. The dimension of the χ^2 function n is the difference between the dimension of the parameter space of the test hypothesis $\vec{\Theta}_1$ and the parameter space of the null hypothesis $\vec{\Theta}_0$, assuming uncorrelated parameters. To obtain the critical χ^2 value for a confidence level η, the χ^2 distribution f for n degrees of freedom (dof) must be integrated over:

$$\int_0^{\Delta\chi^2} f_n(\chi)\mathrm{d}\chi = \eta. \tag{5.7}$$

The thus obtained value of $\Delta\chi^2$ can be used to determine the uncertainties of a single parameter from Likelihood profiling (with e.g. $\Delta\chi^2 = 1$ for the 1-σ uncertainty, see section 5.3), as well as to construct exclusion contours in a multi-dimensional parameter space, such as the one shown in figure 5.1.

An alternative approach to obtain the true upper and lower uncertainties for a given best-fit value are the so-called belt constructions. An example for the neutrino-mass analysis is shown in figure 5.2. These belt constructions are based on large samples of Monte Carlo (MC) for a range of different true values (e.g. $m^2_{\nu,\,\mathrm{true}}$). Each data set is analysed and the distribution of fit values (e.g. $m^2_{\nu,\,\mathrm{fit}}$) is evaluated for each MC true value. Each parameter distribution is then integrated up to a percentage value η of the total sample size, which is equivalent to a confidence level of η. The integration limits may be chosen as two-sided or one-sided, resulting in different confidence belts; however, they are all equivalent in their statistical coverage.

Neyman construction [175]**:** The Neyman belt construction is the simplest approach, which takes a two-sided confidence interval over the parameter distribution, following e.g.

$$\eta = \int_{m^2_{\nu,\,\mathrm{lower}}}^{m^2_{\nu,\,\mathrm{upper}}} \mathcal{L}(m^2_{\nu,\,\mathrm{fit}}|m^2_{\nu,\,\mathrm{true}}) \tag{5.8}$$

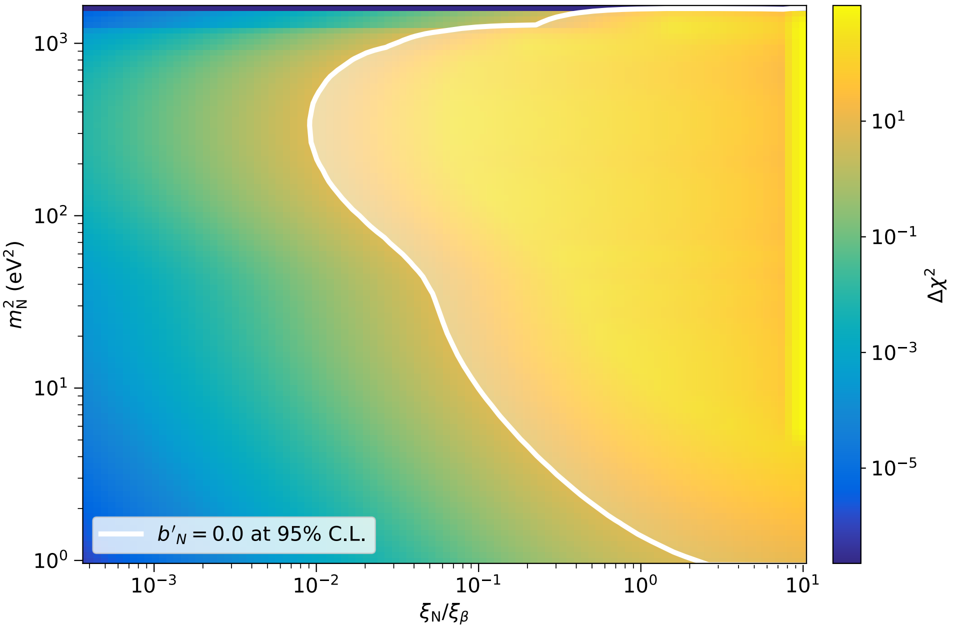

Figure 5.1: Example of an exclusion contour for the parameter space of the GNI based on the second measurement campaign (KNM2). $\Delta\chi^2$ gives the agreement of the model with given parameters m_N^2, ξ_N/ξ_β, and b'_N (introduced in chapter 7) with the data set. The exclusion contour is drawn at the $\Delta\chi^2_\mathrm{crit}$ corresponding to a 95 % CL. Any parameter combinations exhibiting a $\Delta\chi^2 > \Delta\chi^2_\mathrm{crit}$ are excluded and constitute the white shaded parameter space.

for the neutrino mass analysis. The resulting lower and upper boundaries for each true value are then connected to give the confidence belt, as shown in figure 5.2. The true parameter uncertainties are then given by the intersections of the best-fit value with the upper and lower boundaries of the belt. This procedure is equivalent to evaluating the Likelihood profile on Asimov data [80]. However, this approach is not well suited to large negative best-fit values, as they may exceed the bounds of the confidence belt. In such cases, a later modification to the belt construction is necessary, leading to a one-sided evaluation of the parameter distribution. The following belt constructions are designed to circumvent this issue.

Feldman-Cousins [99]**:** The Feldman-Cousins belt construction adjusts the coverage region for large negative best-fit values compared to the Neyman belt by sorting the parameter distribution by its Likelihood ratio

$$R\left(m^2_{\nu,\,\mathrm{fit}}|m^2_{\nu,\,\mathrm{true}}\right) = \frac{\mathcal{L}\left(m^2_{\nu,\,\mathrm{fit}}|m^2_{\nu,\,\mathrm{true}}\right)}{\mathcal{L}\left(m^2_{\nu,\,\mathrm{fit}}|\max\left(m^2_{\nu,\,\mathrm{true}},0\right)\right)} \tag{5.9}$$

rather than the bare Likelihood before integration. This provides a smooth transition between a two-sided and one-sided confidence interval, ensuring proper coverage also for negative best-fit values.

Lokhov-Tkachov [160]**:** Similar to the Feldman-Cousins belt construction, the Lokhov-Tkachov belt construction also addresses the correct coverage of negative best-fit values, however, it is designed not to improve the sensitivity in the negative region. This is achieved

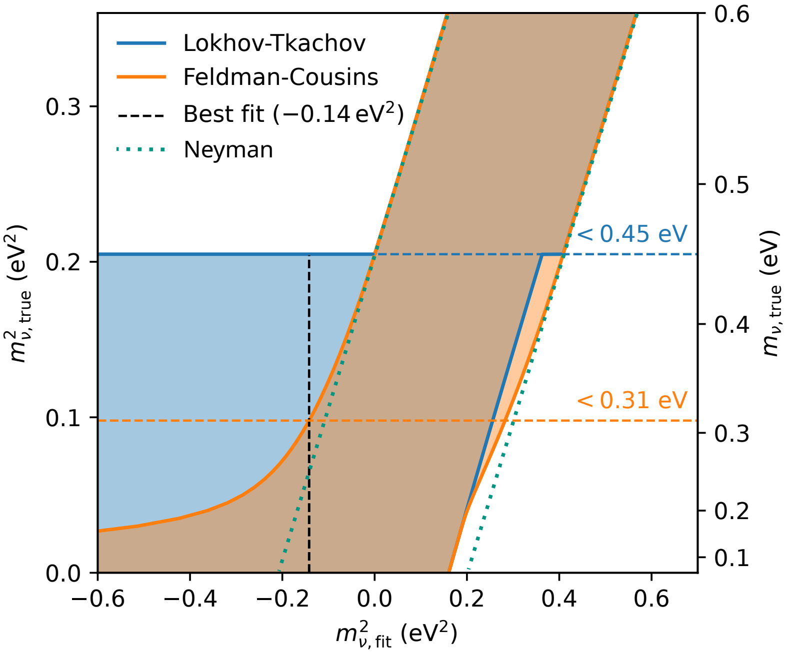

Figure 5.2: Example of Lokhov-Tkachov, Feldman-Cousins, and Neyman confidence-belt construction for the KATRIN neutrino mass analysis. The confidence belts are constructed from the evaluation of fit-parameter ($m^2_{\nu,\mathrm{fit}}$) distributions generated based on large-sample MC for different true values $m^2_{\nu,\mathrm{true}}$, and allow to obtain the true upper and lower uncertainties for a given best-fit value. All confidence belts provide equivalent coverage; here shown for 90 % CL. Based on [17].

by defining two regions: A two-sided confidence interval is calculated for $m^2_{\nu,\,\mathrm{fit}} > 0$, while a one-sided confidence interval is chosen for negative $m^2_{\nu,\,\mathrm{fit}}$ values. This methodology consequently constructs a plateau in the region for negative fit values, thereby preventing a seeming increase in sensitivity caused by statistical fluctuations of the best fit. Thus, this is regarded as a conservative sensitivity estimation.

The procedure of the belt construction from large MC samples is also known as full construction of confidence intervals, as it is robust against deviations from Wilks' theorem. However, it is also very computationally expensive. The belt construction presented above can be extended for multi-dimensional parameter spaces, such as the sterile-neutrino and GNI parameter spaces, to ensure correct coverage for a given $\Delta\chi^2_{\mathrm{crit}}$ value.

5.5 The KASPER Framework

KASPER is a versatile C++ software environment, that has been developed for the use of KATRIN. The multiple components enable access to all KATRIN detector and sensor data via KaLi, data processing such as the generation of the run-summary files via BEANS, simulations such as the tracking of charged particles in the electromagnetic fields with Kassiopeia[1] [108], and data analysis with KaFit. Several additional components are interconnected with and provide functionalities to the aforementioned examples. Comprehensive documentation on the components can be found in [109, 108, 121, 146]. The following describes the two main components used for the data analysis in this work.

5.5.1 Source and Spectrum Calculation

A mathematical description of the experimental setup and calculation of its integral spectrum is provided by the Source and Spectrum Calculation (SSC) module, containing a model of the source and transmission properties [133, 146]. Based on the electromagnetic and gas-dynamic settings, SSC calculates the differential spectrum and numerically convolves it with the response function, as introduced in chapter 4. These calculations are implemented for both tritium and krypton [164], thereby also allowing the analysis of dedicated krypton calibration campaigns [11]. The modularity of SSC allows for easy configuration of the model based on the experimental conditions during the measurement; the source model, the FSD, the differential spectrum model, the energy-loss function, the transmission and response function, the detector, and finally, the integrated spectrum are all initialised with individual settings via a configuration file. Further information on the individual components can be found in [121, 133, 141, 146]. These model calculations are essential for the data analysis with KaFit and as input for the simulations with Kassiopeia. During the data analysis with KaFit, the initialised model parameters can be introduced as fit parameters and thereby further optimised. In addition, the model evaluation is characterised by its good precision and numerical stability, which is ensured through a binning of the spectrum and integration based on either Simpson's rule, Romberg's method, or the Legendre-Gauss quadrature. Finally, the calculations have been significantly sped up by the introduction of caching for most of the model components, thereby avoiding reoccurring calculation steps.

---

[1] Kassiopeia is the only open-source component of KASPER and can be found under https://github.com/KATRIN-Experiment/Kassiopeia

5.5.2 The KaFit Framework

The KATRIN Fit environment (KaFit) has been designed for two principal purposes: firstly, the generation of simulated Asimov or MC data for the purpose of sensitivity studies and statistical coverage test; secondly, the performance of complex analyses of given data sets. The required model evaluations for the data generation and analysis are performed by SSC; the Likelihood estimation for the frequentist analysis is performed with the C++ package MINUIT. In addition, sampling algorithms such as a Markov Chain Monte Carlo (MCMC) algorithm are available for Bayesian analyses [127, 102]. The handling of the data during the analysis, along with links to the model configuration, data, and parameter settings, are detailed in the KaFit configuration file. The data is stored in so-called run-summary files, which contain the spectral count rates in addition to slow control values recorded during the time of the spectral scan. More general parameter values that persist for the duration of an entire campaign are stored in the period-summary document. The so-called run register links all data going into the fit, while handling the exclusion of individual pixels, the grouping of the data, and the choice of the analysis interval. Generally, all scans of a measurement campaign can be stacked into one spectrum and their slow control values can be averaged. This data combination is done either via the run register or in advance via the run-summary-merger functionality of KaFit, producing a merged run-summary document, thereby reducing the read-in time during the analysis itself. For each scan, the rate in the run-summary file is given per pixel. The run register allows these rates to be combined uniformly across the detector, or in predefined patterns of concentric rings or patches. The fit parameters are defined in the extended-parameter document, which initialises the parameter with a given start value, start error, given bounds, and either as a fixed or free parameter. In addition, Gaussian penalty terms and correlations between fit parameters are introduced in this file. Finally, the analysis routine commences by evaluating the Likelihood function based on the initial parameters and the given data set, and continues to stepwise optimise the parameters until convergence for a minimum is reached. The final parameter set is then written to a root file.

6. The second KATRIN Measurement Campaign

Data taking with the KATRIN experiment commenced in June 2018, with the First Tritium campaign. The first dedicated KATRIN Neutrino-mass Measurement campaign (KNM) followed in March 2019. Since then, data taking has been continuously ongoing, with KNM16 currently being recorded as of February 2025, and will continue until the end of 2025.

The analysis presented in this thesis is based on the data from the second measurement campaign (KNM2), which was carried out from September 27th to November 14th 2019 with about 45 measurement days. During this time, a total of 361 spectral scans were collected that went into the analysis, scanning in up, down, and random order to avoid bias. The scan-step duration for each retarding energy was optimised for sensitivity to the neutrino mass between KNM1 and KNM2. A comparison between the spectra and Measurement Time Distribution (MTD) of the two campaigns is shown in figure 6.1. Further insights into the optimisation of the MTD can be found in [146, 204].

As in the neutrino-mass analysis, the data recorded at the scan steps within the range $[E_0 - 40\,\mathrm{eV},\, E_0 + 135\,\mathrm{eV}]$ is used. Measurement points beyond this range are utilised to monitor the rate stability and quantify systematic effects. The measurement points above the kinetic endpoint E_0 are vital for a precise determination of the background rate. The homogenous electromagnetic fields configuration and stable measurement conditions allow a uniform combination of the 117 active detector pixels[1] for each scan and a combination of all scans, leading to a total of 3.76×10^6 signal electrons going into the analysis[2]. The KNM2 campaign was selected for the proof-of-principle study in this thesis because it features a background reduced by 25 % to 0.22 cps, and an increased signal rate due to a 3.9 times higher tritium gas density in the source of $4.2 \times 10^{21}\,\frac{1}{\mathrm{m}^2}$, compared to the first neutrino-mass measurement [21]. The background reduction was achieved by a baking of the main spectrometer vessel at 200 °C for an approximate duration of two weeks, which improved the vacuum conditions, reduced the occurrence of loosely bound atoms contributing to the background, and increased the capture efficiency for radon emanating from the getter pumps of the main spectrometer. Further details on the data set can be found in ref. [18]. An overview of key values of the second measurement campaign is given in table 6.1.

---

[1] From a total of 148 detector pixels, 31 are excluded due to either the FBM shadowing pixels, high noise or damage of a pixel, or due to the alignment of the fluxtube onto the detector.

[2] Another 5.54×10^5 electrons were detected, which are attributed to the background.

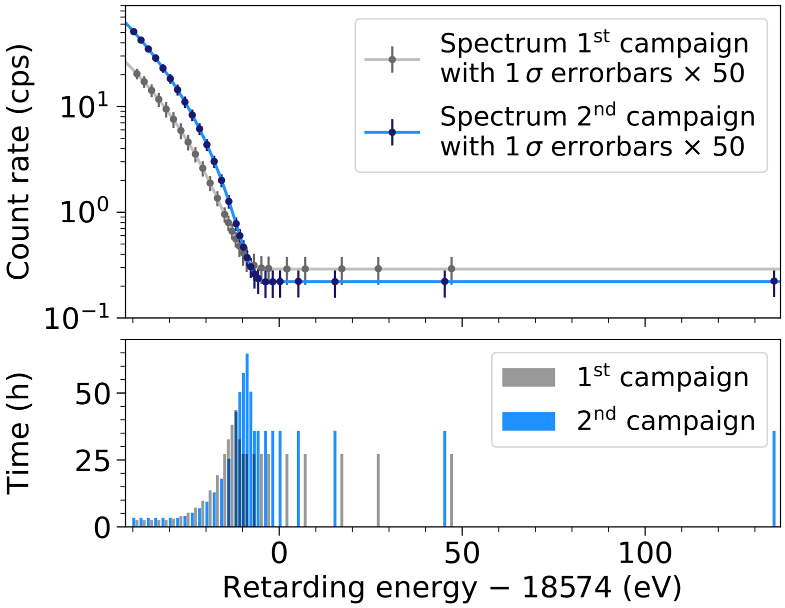

Figure 6.1: Combined spectra of all spectral scans performed during KNM1 and KNM2 (upper plot). Data points are shown with their statistical error, enlarged by a factor of 50. The lower plot gives the time spent at each measurement point, i.e. the MTD. Figure taken from [18].

Table 6.1: Summary of important key numbers and measurement settings of the second measurement campaign (KNM2).

Number of scans	361
Live time	694 hrs
Number of β electrons	3.76×10^6
Background rate	0.22 cps
Pre-spectrometer voltage	−10.5 keV
T_2 column density	$4.2 \times 10^{21}\ \frac{1}{\mathrm{m}^2}$
Stability	< 0.02 ‰
Source activity	94 GBq
Source temperature	30.1 K
Rear wall potential	−0.05 V to 0.19 V

7. General Neutrino Interactions at KATRIN

This chapter presents the theoretical calculations, analysis strategy and results for the search for GNI at KATRIN. Firstly, the effective differential decay rate is derived from the GNI theory (see section 7.1), and the connection between the experimental GNI parameters and the individual interactions is laid out (see section 7.2). Thereafter, the analysis strategy is presented in section 7.3. The subsequent section 7.4 is concerned with ensuring correct coverage of the exclusion contours. Finally, the resulting exclusion contours and constraints on individual interactions are presented in section 7.5. The derivation, analysis, and results presented in this chapter have been published in [19].

7.1 Derivation of the Effective Decay Rate

For deriving the effective β-decay rate under the influence of GNI, reference [162] is taken as a starting point. The effective Lagrangian used for this derivation is composed of two elements: the Lagrangian describing the Standard Model contribution and the charged-current GNI Lagrangian, denoted by $\mathcal{L}_{\mathrm{GNI}}^{\mathrm{CC}}$ and defined in equation 2.3. The GNI operators are defined in table 2.1. In order to obtain the squared matrix element of the decay, $|\mathcal{M}|^2$, a sum of traces over all possible combinations of GNI and Standard Model interactions must be calculated. The integration of $|\mathcal{M}|^2$ over the neutrino energy provides a complete description of the total differential decay rate. To simplify the lengthy new description of the total differential decay rate, in order for it to be applicable for a search for new physics on the β-spectrum, we expand in small parameters [162]

$$\varepsilon := \frac{m_{\mathcal{A}} - m_{\mathcal{B}}}{m_{\mathcal{A}}}, \quad \delta := \frac{m_{\mathrm{e}}}{m_{\mathcal{A}}}, \quad \eta := \frac{E_{\mathrm{e}}}{m_{\mathcal{A}}} \quad \text{and} \quad \rho := \frac{m_j}{m_{\mathcal{A}}}, \tag{7.1}$$

where $\mathcal{A}$ indicates the mother nucleus and $\mathcal{B}$ the daughter nucleus. m_j are the individual neutrino-mass eigenstates. To incorporate nuclear effects into the quark-level calculations, nuclear matrix elements are taken into account. The corresponding nuclear form factors are given in table 7.1. The relevant matrix elements for tritium β decay can be found in [75]. Given that $q \equiv p_n - p_p < 20\,\mathrm{keV}$ and $M_{\mathrm{N}} \equiv (m_{\mathcal{A}} + m_{\mathcal{B}})/2 \simeq 3\,\mathrm{GeV}$ for tritium decay, it is sufficient to consider terms up to $\mathcal{O}(q/M_{\mathrm{N}}) < 10^{-5}$ in the calculation. The matrix element associated with the pseudoscalar coupling

$$\langle \mathrm{p}(p_{\mathrm{p}})|\, \bar{\mathrm{u}}\gamma_5\mathrm{d}\, |\mathrm{n}(p_{\mathrm{n}})\rangle = g_{\mathrm{P}}(q^2)\bar{u}_{\mathrm{p}}(p_{\mathrm{p}})\gamma_5 u_{\mathrm{n}}(p_{\mathrm{n}}) = \mathcal{O}(q/M_{\mathrm{N}}) \tag{7.2}$$

Table 7.1: Numerical values for the nuclear form factor used in the calculations at hand. (CVC = conserved vector current, $\overline{\mathrm{MS}}$ = modified minimal subtraction scheme).

Coupling	Value	Reference, Comments
g_{V}	1	[203], (assuming CVC) ^{3}H
$\frac{g_{\mathrm{A}}}{g_{\mathrm{V}}}$	1.2646 ± 0.0035	[27], ^{3}H
g_{S}	1.02 ± 0.11	[118], $\overline{\mathrm{MS}}$, neutron
g_{P}	349 ± 9	[118], $\overline{\mathrm{MS}}$, neutron
g_{T}	$0.987 \pm 0.051 \pm 0.020$	[57], lattice, $\overline{\mathrm{MS}}$, neutron

is suppressed at the order 10^{-5} and therefore not further considered due to its negligible impact. u_{p} and u_{n} are the spinors of the proton and neutron, respectively. Also, the contribution of the weak magnetism is assumed to be negligible. This leads to an effective description of the GNI contributions in terms of the GNI parameters ξ, b, b' and c as

$$\begin{aligned}\left(\frac{\mathrm{d}\Gamma}{\mathrm{d}E}\right)_j =& \frac{G_{\mathrm{F}}^2 V_{\mathrm{ud}}^2}{2\pi^3}\sqrt{(E+m_{\mathrm{e}})^2 - m_{\mathrm{e}}^2}(E+m_{\mathrm{e}})(E_0-E)\sqrt{(E_0-E)^2 - m_j^2} \\ &\cdot \xi\left[1 + b\frac{m_{\mathrm{e}}}{E+m_{\mathrm{e}}} - b'\frac{m_j}{E_0-E} - c\frac{m_{\mathrm{e}} m_j}{(E+m_{\mathrm{e}})(E_0-E)}\right].\end{aligned} \tag{7.3}$$

This effective description has successfully been derived from first principles using Mathematica; good agreement was found with the existing literature [136, 63].

In this analysis, we employ an effective mass description, wherein the neutrino masses m_j are considered to be fully degenerate. This is a valid approximation, as the individual neutrino-mass states cannot be resolved by the current setup. Consequently, the sum over the neutrino-mass states can be treated as the effective neutrino mass, m_β. Also, as only lepton number conserving terms are considered in equation 2.3, no distinction between a Dirac or Majorana nature of the neutrinos can be made. Since the current setup is not sensitive to the parameters b or to b' and c individually, we apply $E \ll m_{\mathrm{e}}$ in the analysis. The corresponding redefinition is $\xi_k + \xi_k b_k \rightarrow \xi_k$ and $\xi_k b'_k + \xi_k c_k \rightarrow \xi_k b'_k$. For future reference and better comparison with published results, we give the explicit definitions for the four GNI parameters separately in equations 7.6 to 7.9.

The analysis furthermore distinguishes between a scenario with (N) and without (β) an additional heavier neutrino-mass state. In accordance to [162], we define m_i and M_j to be the masses of the light and heavy neutrino-mass eigenstates ν'_i and N'_j, respectively. The left- and right-handed neutrino-flavour fields with the mixing matrices U, T, S, and V are given in a left-right-symmetric approach by

$$\nu_{\mathrm{e,L}} = U_{\mathrm{e}i}\,\nu'_i + S_{\mathrm{e}j}\,\mathrm{N}'^{\,c}_j, \tag{7.4}$$

$$\nu_{\mathrm{e,R}} = T^*_{\mathrm{e}i}\,\nu'^{\,c}_i + V^*_{\mathrm{e}j}\,\mathrm{N}'_j. \tag{7.5}$$

S and T are presumably small. The explicit dependency of the GNI parameters is analogous for both cases. Therefore, we present the results only for the light neutrino-mass state. With $U \rightarrow S$ and $T \rightarrow V$ the results are valid for the heavy neutrino-mass state.

$$\begin{aligned}\xi_\beta =& |U_{\mathrm{e}i}|^2 \left[(g_\mathrm{V}^2 + 3g_\mathrm{A}^2)(1 + |\epsilon_\mathrm{L}|^2 + |\epsilon_\mathrm{R}|^2 + 2\,\mathrm{Re}(\epsilon_\mathrm{L})) + 2(g_\mathrm{V}^2 - 3g_\mathrm{A}^2)(\mathrm{Re}(\epsilon_\mathrm{R}\epsilon_\mathrm{L}^*)\right. \\ &\left. + \mathrm{Re}(\epsilon_\mathrm{R})) + g_\mathrm{S}^2|\epsilon_\mathrm{S}|^2 + 48 g_\mathrm{T}^2|\epsilon_\mathrm{T}|^2\right] + |T_{\mathrm{e}i}|^2\left[(g_\mathrm{V}^2 + 3g_\mathrm{A}^2)(|\tilde{\epsilon}_\mathrm{L}|^2 + |\tilde{\epsilon}_\mathrm{R}|^2)\right. \\ &\left. + 2(g_\mathrm{V}^2 - 3g_\mathrm{A}^2)\,\mathrm{Re}(\tilde{\epsilon}_\mathrm{R}\tilde{\epsilon}_\mathrm{L}^*) + g_\mathrm{S}^2|\tilde{\epsilon}_\mathrm{S}|^2 + 48 g_\mathrm{T}^2|\tilde{\epsilon}_\mathrm{T}|^2\right]\end{aligned} \tag{7.6}$$

$$\begin{aligned}\xi_\beta b_\beta =& |U_{\mathrm{e}i}|^2\left[2g_\mathrm{S}g_\mathrm{V}\,\mathrm{Re}(\epsilon_\mathrm{S}(1 + \epsilon_\mathrm{L} + \epsilon_\mathrm{R})^*) - 24 g_\mathrm{A}g_\mathrm{T}\,\mathrm{Re}(\epsilon_\mathrm{T}(1 + \epsilon_\mathrm{L} - \epsilon_\mathrm{R})^*)\right] \\ & + |T_{\mathrm{e}i}|^2\left[2g_\mathrm{S}g_\mathrm{V}\cdot\mathrm{Re}(\tilde{\epsilon}_\mathrm{S}(\tilde{\epsilon}_\mathrm{L} + \tilde{\epsilon}_\mathrm{R})^*) + 24 g_\mathrm{A}g_\mathrm{T}\,\mathrm{Re}(\tilde{\epsilon}_\mathrm{T}(\tilde{\epsilon}_\mathrm{L} - \tilde{\epsilon}_\mathrm{R})^*)\right]\end{aligned} \tag{7.7}$$

$$\begin{aligned}\xi_\beta b'_\beta =&\ \mathrm{Re}(U_{\mathrm{e}i}T_{\mathrm{e}i})\left[2g_\mathrm{V}g_\mathrm{S}(\mathrm{Re}(\tilde{\epsilon}_\mathrm{S}(1 + \epsilon_\mathrm{L} + \epsilon_\mathrm{R})^*) + \mathrm{Re}(\epsilon_\mathrm{S}(\tilde{\epsilon}_\mathrm{L} + \tilde{\epsilon}_\mathrm{R})^*))\right. \\ & \left. - 24 g_\mathrm{A}g_\mathrm{T}(\mathrm{Re}(\tilde{\epsilon}_\mathrm{T}(1 + \epsilon_\mathrm{L} - \epsilon_\mathrm{R})^*) - \mathrm{Re}(\epsilon_\mathrm{T}(\tilde{\epsilon}_\mathrm{L} - \tilde{\epsilon}_\mathrm{R})^*))\right]\end{aligned} \tag{7.8}$$

$$\begin{aligned}\xi_\beta c_\beta =&\ \mathrm{Re}(U_{\mathrm{e}i}T_{\mathrm{e}i})\left[2g_\mathrm{V}^2\,\mathrm{Re}((\tilde{\epsilon}_\mathrm{L} + \tilde{\epsilon}_\mathrm{R})(1 + \epsilon_\mathrm{L} + \epsilon_\mathrm{R})^*)\right. \\ & \left. - 6g_\mathrm{A}^2\,\mathrm{Re}((\tilde{\epsilon}_\mathrm{L} - \tilde{\epsilon}_\mathrm{R})(1 + \epsilon_\mathrm{L} - \epsilon_\mathrm{R})^*) + 2g_\mathrm{S}^2\,\mathrm{Re}(\epsilon_\mathrm{S}\tilde{\epsilon}_\mathrm{S}^*) + 96 g_\mathrm{T}^2\,\mathrm{Re}(\epsilon_\mathrm{T}\tilde{\epsilon}_\mathrm{T}^*)\right)\end{aligned} \tag{7.9}$$

These equations agree with the corresponding formulas in references [93, 136, 115, 65]. In order to derive the limits on the ϵ_i and $\tilde{\epsilon}_i$ couplings, we assume the above-defined terms and their constituents to be real.

Consequently, the full differential decay rate including GNI then takes the form:

$$\begin{aligned}\frac{\mathrm{d}\Gamma}{\mathrm{d}E} =& \frac{G_\mathrm{F}^2 V_\mathrm{ud}^2}{2\pi^3} F(E,\, 2)\sqrt{(E + m_\mathrm{e})^2 - m_\mathrm{e}^2}(E + m_\mathrm{e}) \\ & \cdot\sum_j \sum_{k=\beta,\,\mathrm{N}} \zeta_j\varepsilon_j\sqrt{\varepsilon_j^2 - m_k^2}\xi_k\left[1 - b'_k\frac{m_k}{\varepsilon_j}\right]\Theta(\varepsilon_j - m_k).\end{aligned} \tag{7.10}$$

The Fermi function, $F(E,\, 2)$, models the electromagnetic interaction of the emitted electrons with the daughter nucleus. The electrons' kinetic energy is denoted by E and their mass by m_e. Analogous to the already discussed calculations for the tritium β-decay rate in section 4.1, the impact of the molecular final states is considered by incorporating the molecular excitation energy, V_j, which reduces the available neutrino energy, $\varepsilon_j = E_0 - E - V_j$. The probability of producing the excited state j is given by ζ_j. Beyond that, radiative corrections are taken into account, while further theoretical corrections are neglected [145]. Further details can be found in chapter 4. Following the derivation above, both the ξ_k and the b'_k parameters are now defined in terms of the flavour-space tensors $\epsilon_{j,\mathrm{ud}}$ and $\tilde{\epsilon}_{j,\mathrm{ud}}$, expressing the coupling strength of the GNI to left- and right-handed neutrinos, respectively, the mixing matrices $U_{\mathrm{e}i}$ and $T_{\mathrm{e}i}$ for the left- and right-handed light neutrino, the mixing matrices $S_{\mathrm{e}i}$ and $V_{\mathrm{e}i}$ for the left- and right-handed heavy neutrino, and the nuclear form factors g_V, g_S, g_T, and g_A. The Standard Model differential decay rate introduced in equation 4.2 can be restored by setting $\xi_\mathrm{N} = b'_k = 0$. Furthermore, the differential equation for the search of sterile neutrinos [20] can be obtained by neglecting all GNI couplings ϵ, resulting in the vanishing of b'_N and the transformation

$$\frac{\xi_\mathrm{N}}{\xi_\beta} = \frac{S_{\mathrm{e}i}^2}{U_{\mathrm{e}i}^2} \mathrel{\widehat{=}} \frac{U_{\mathrm{e}4}^2}{1 - U_{\mathrm{e}4}^2}, \tag{7.11}$$

with $U_{\mathrm{e}4}^2$ being the active-to-sterile mixing. The distinct signatures of ξ_k and b'_k on the β-spectrum are visualized in figure 7.1. The differential decay rate is included in the prediction

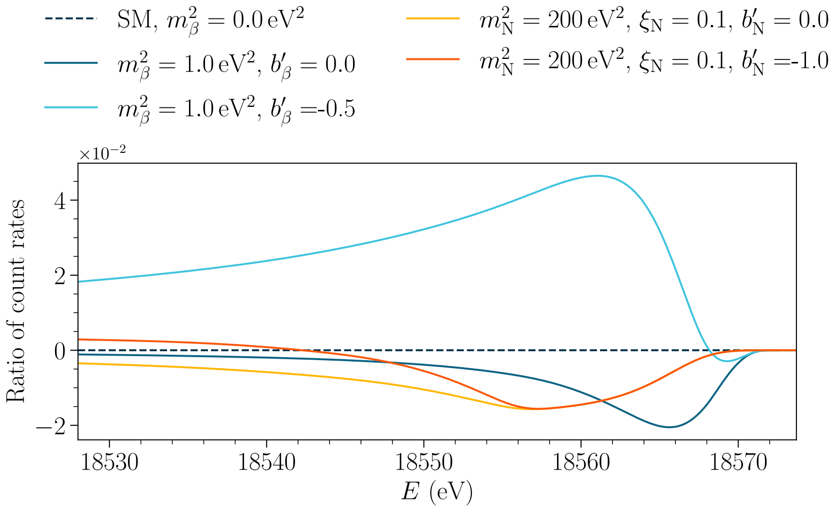

Figure 7.1: Effect of different GNI contributions on the endpoint region of the integral β-spectrum. Both cases with (N) and without (β) the presence of an additional heavier neutrino have been considered. The position of the kink-like structure in the signal is dependent on the (heavy) neutrino mass $m^2_{\beta(\mathrm{N})}$. The endpoint is here at 18 573.7 eV.

of the observed integral rate through equation 4.5, combining it with the experimental response function $f(E, qU_i)$, which describes the transmission properties of the experiment, as well as accounting for additional physical effects such as electron scatterings. All relevant systematic effects included in the model are covered in [17] and chapter 4, and are being investigated in the context of GNI in section 7.5.

7.2 Inference on individual General Neutrino Interaction Couplings

The above derived description of GNI in tritium β decay allows to constrain the GNI parameter space of m_k, ξ_k and b'_k with the data of KATRIN, thereby constraining the specific combination of additional interactions via their coupling strength ϵ, given by equations 7.6 to 7.9. Comparability with constraints from other experimental approaches can be achieved by considering more specific scenarios of individual or a small subset of interactions. Consequently, all but the desired ϵ couplings are set to zero. In the absence of a heavier neutrino, the parameter space $m^2_\beta \times b'_\beta$ is probed. For a chosen value of m^2_β, the experimental limit on b'_β can then be converted into limits on the ϵ couplings. The transformations for the individual interaction couplings are given by:

$$\tilde{\epsilon}_\mathrm{L}: \quad b'_\beta = \frac{(-6g_\mathrm{A}^2 + 2g_\mathrm{V}^2)\, T_{\mathrm{e}i}\tilde{\epsilon}_\mathrm{L}}{(3g_\mathrm{A}^2 + g_\mathrm{V}^2)(1 + T_{\mathrm{e}i}^2\tilde{\epsilon}_\mathrm{L}^2)}, \tag{7.12}$$

$$\tilde{\epsilon}_\mathrm{R}: \quad b'_\beta = \frac{(-6g_\mathrm{A}^2 + 2g_\mathrm{V}^2)\, T_{\mathrm{e}i}\tilde{\epsilon}_\mathrm{R}}{(3g_\mathrm{A}^2 + g_\mathrm{V}^2)(1 + T_{\mathrm{e}i}^2\tilde{\epsilon}_\mathrm{R}^2)}, \tag{7.13}$$

$$\tilde{\epsilon}_\mathrm{S}: \quad b'_\beta = \frac{2g_\mathrm{S}g_\mathrm{V}T_{\mathrm{e}i}\tilde{\epsilon}_\mathrm{S}}{3g_\mathrm{A}^2 + g_\mathrm{V}^2 + g_\mathrm{S}^2T_{\mathrm{e}i}^2\tilde{\epsilon}_\mathrm{S}^2}, \tag{7.14}$$

$$\tilde{\epsilon}_\mathrm{T}: \quad b'_\beta = -\frac{24g_\mathrm{A}g_\mathrm{T}T_{\mathrm{e}i}\tilde{\epsilon}_\mathrm{T}}{3g_\mathrm{A}^2 + g_\mathrm{V}^2 + 48g_\mathrm{T}^2T_{\mathrm{e}i}^2\tilde{\epsilon}_\mathrm{T}^2}. \tag{7.15}$$

In the presence of an additional heavier neutrino, the experimental limit on the parameter space $m_N^2 \times \frac{\xi_N}{\xi_\beta} \times b'_N$ is converted into constraints on individual couplings by choosing a value for m_N^2 and considering the maximal range of $b'_\mathrm{N} \in [-1.0,\, 1.0]$. This results in an upper limit range. The transformations read:

$$\tilde{\epsilon}_\mathrm{L}: \quad \frac{\xi_\mathrm{N}}{\xi_\beta} = \tilde{\epsilon}_\mathrm{L}^2, \tag{7.16}$$

$$\tilde{\epsilon}_\mathrm{R}: \quad \frac{\xi_\mathrm{N}}{\xi_\beta} = \tilde{\epsilon}_\mathrm{R}^2, \tag{7.17}$$

$$\tilde{\epsilon}_\mathrm{S}: \quad \frac{\xi_\mathrm{N}}{\xi_\beta} = \frac{g_\mathrm{S}^2\tilde{\epsilon}_\mathrm{S}^2}{3g_\mathrm{A}^2 + g_\mathrm{V}^2}, \tag{7.18}$$

$$\tilde{\epsilon}_\mathrm{T}: \quad \frac{\xi_\mathrm{N}}{\xi_\beta} = \frac{48g_\mathrm{T}^2\tilde{\epsilon}_\mathrm{T}^2}{3g_\mathrm{A}^2 + g_\mathrm{V}^2}. \tag{7.19}$$

Constraints for multiple couplings are derived in an analogous way.

7.3 Analysis Strategy

The presented analysis separately investigates a case with light and with additional heavier neutrinos. Consequently, two distinct sets of parameters of interest are considered. In order to infer the parameters of interest in the absence of any heavy neutrinos, we focus on the two-dimensional parameter space comprising the effective neutrino mass m_β and the shape-modifying GNI parameter b'_β. In the presence of heavier neutrinos, the three-dimensional parameter space is defined by the heavier neutrino-mass state m_4^2 and the GNI parameters ξ_N, in units of $\xi_\beta = g_\mathrm{V}^2 + 3g_\mathrm{A}^2$, and b'_N. The amplitude of the additional neutrino branch is scaled by ξ_N, while specific shape deformations are introduced by b'_N, as can be seen in figure 7.1 and equation 7.10. E_0, A_s, and the constant background component $R_\mathrm{bg}^\mathrm{base}$ are added as nuisance parameters.

The GNI parameter space is probed on a grid, for which the model is fit to the data with respect to the nuisance parameters at each grid point using χ^2-function minimization. This allows for a numerically robust minimization of the χ^2-function. The propagation of systematic uncertainties is conducted using a pull-term approach [18], as introduced in section 5.2.

In the absence of a heavy neutrino, a 60 × 30 linearly spaced grid over the parameter space $m_\upbeta^2 \times b'_\upbeta$ within the intervals $[0\,\mathrm{eV}^2,\ 2.2\,\mathrm{eV}^2] \times [-1.0,\ 1.0]$ has been employed. The three-dimensional parameter space for the case including heavy neutrinos with masses $m_\mathrm{N} \gg m_\upbeta$ is defined by 30×40 logarithmically spaced values of the parameters $m_\mathrm{N}^2 \times \xi_\mathrm{N}/\xi_\upbeta$ within $[1\,\mathrm{eV}^2,\ 1600\,\mathrm{eV}^2] \times [3.6 \cdot 10^{-4},\ 10.0]$ times 9 linearly spaced values for b'_N within $[-1.0,\ 1.0]$.

In addition, further improvements have been implemented to optimise the fit duration and convergence for the more computationally expensive three-dimensional grid involving the additional heavier neutrino, both on the level of the model evaluation in SSC and in the initialisation procedure of each grid point.
Firstly, the spectral discontinuity caused by the rate drop at the endpoint of the additional β-spectrum branch was addressed by separating the integration of both spectral branches in SSC. This enabled the usage of an optimised integration procedure, that uses the more accurate Gauss-Legendre quadrature in the endpoint region, while the Simpson method is used for the rest of the spectrum. This implementation resulted in an enhancement in fit stability, albeit at the expense of an increase in fit duration.
Secondly, an iterative approach for the initialisation of the fits on the grid has been developed: The initialisation of the fits in the lowest-expected χ^2 region is performed with the default start values $\vec{\Theta}_{0,\,\mathrm{start}}$. The resulting parameter set $\vec{\Theta}_{0,\,\mathrm{best}}$ is then utilised to initialise the subsequent subset of fits towards higher values of χ^2, following $\vec{\Theta}_{i+1,\,\mathrm{start}} = \vec{\Theta}_{i,\,\mathrm{best}}$. In addition, to better account for the changes in amplitude over the grid in the start values, the fitting procedure at each grid point has been split in two parts: A simplified fit is used to approximate the amplitude at the new grid point, which is then applied to initialise the proper fit of the grid point, together with the iterated parameter set $\vec{\Theta}_{i+1,\,\mathrm{start}}$. This approach has been shown to optimise both the total calculation time and the fit stability.

The correctness of the implementation of the model has been confirmed by the conformity of the results with those obtained with the independent sterile-neutrino analysis framework at KATRIN, see figure 8 in [20]. A direct comparison of sensitivity contours between the two implementations is shown in figure 7.2. Furthermore, to mitigate human-induced biases, a blinding scheme was applied. The analysis procedure was first applied to an Asimov data set [80]. Next, a simulated data set with statistical fluctuations was used to test the robustness of the procedure, as shown in figure 7.3. Thereafter, the analysis procedure was fixed and applied to the experimental data.

7.4 Coverage Studies of Exclusion Contours

The correct coverage of the contours is ensured by dedicated MC studies. In addition to the full model description outlined in chapter 4, a simplified analytical model has been employed to reduce computation time; the consistency of the models' results has been confirmed. It was found, that there exist noticeable correlations between the neutrino mass m_k^2, the endpoint E_0, and b'_k, as shown in figure 7.4, as well as that these parameters exhibit non-Gaussian parameter distributions. The correlation between the neutrino mass and endpoint is known [177, 205], whereas the correlation between the neutrino mass and b'_k can be directly inferred from equation 7.10. Consequently, the critical values of the $\Delta\chi^2$ distribution have been derived through a full construction of confidence intervals (see section 5.4) using Monte Carlo simulations on $\mathcal{O}(10\,000)$ randomised spectra. The obtained $(m_{\upbeta,\,\mathrm{true}}^2,\ b'_{\upbeta,\,\mathrm{true}})$ values are compared with the $\Delta\chi^2$ map based on Asimov data to derive

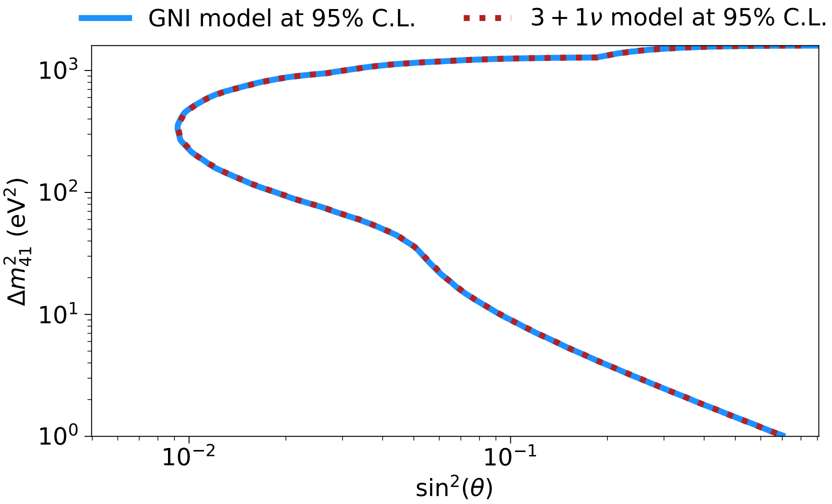

Figure 7.2: Comparison of sensitivity contours obtained with the GNI framework and the independent $3+1\nu$ sterile-neutrino framework. The GNI parameter space is reduced to $m_{\mathrm{N}}^2 \times \xi_{\mathrm{N}}/\xi_\beta$ with $b'_{\mathrm{N}} = 0$ and transformed into the sterile-neutrino parameter space $\Delta m_{41}^2 \times \sin^2(\theta)$, with Δm_{41}^2 being the difference between the squared sterile-neutrino mass m_4^2 and the squared light active-neutrino mass m_1^2, and $\sin^2(\theta) = |U_{\mathrm{e4}}|^2$ being the active-to-sterile mixing, following equation 7.11.

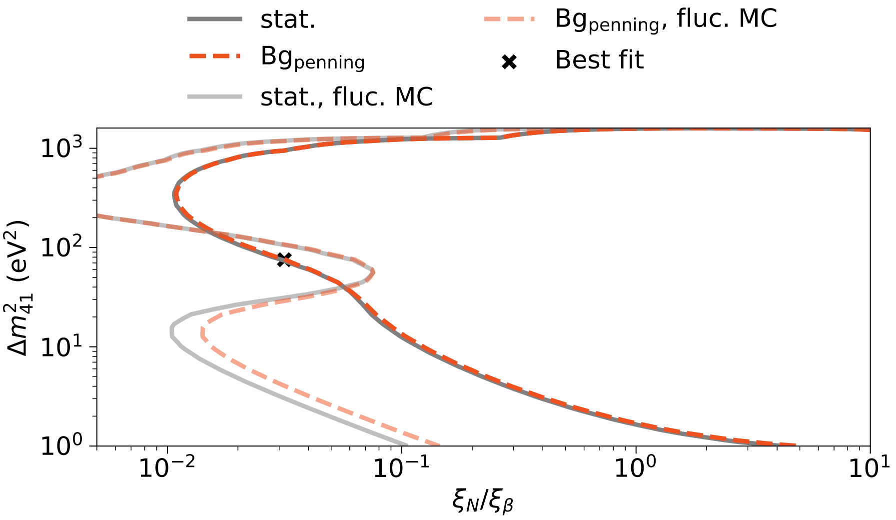

Figure 7.3: Comparison of sensitivity contours on simulated data with and without statistical fluctuations, taking into account an additional heavier neutrino. The contours are drawn for $b'_{\mathrm{N}} = 0$ at 95 % CL and take into account only statistical uncertainties (stat.) or in addition the scan-step-duration dependent Penning background, which is the largest systematic contribution (see figure 7.11). The sensitivity contour derived on the fluctuated data set warps around the corresponding best fit value, demonstrating proper behaviour of the analysis.

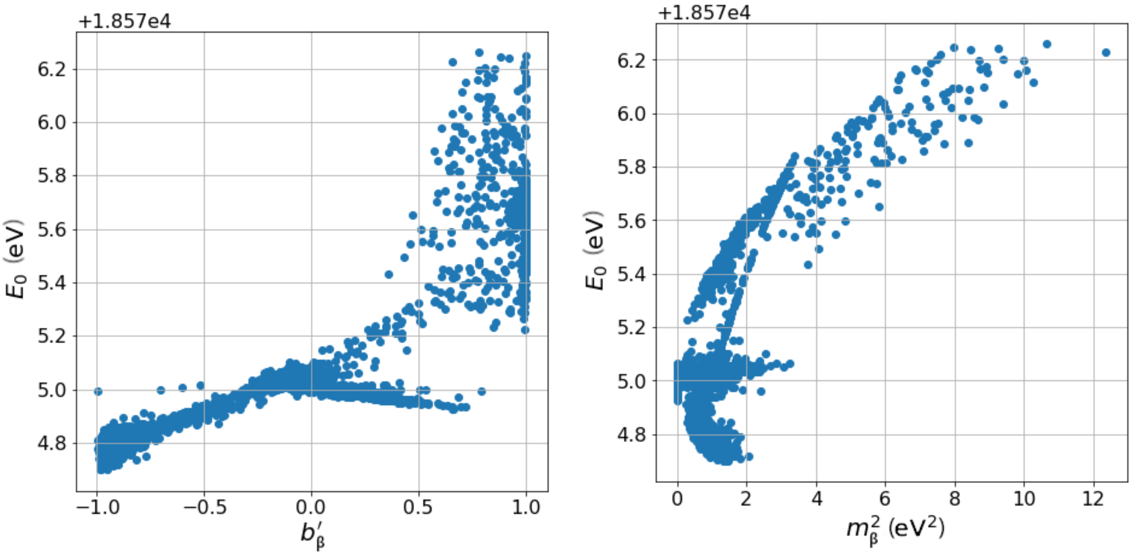

Figure 7.4: Correlations between the neutrino mass m^2_β, the endpoint E_0, and b'_β from studies on MC.

the corresponding $\Delta\chi^2_{\mathrm{crit}}$ value, as shown in figure 7.5. A good agreement is found between the results of the full construction and the prediction by Wilks' Theorem for $(n-1)$ dof, accounting for the observed correlations. The exclusion contours at the 95 % CL are then drawn at $\Delta\chi^2_\beta = 3.84$ and $\Delta\chi^2_{\mathrm{N}} = 5.99$ for the grids without and with heavy neutrinos, respectively.

7.5 Results

The combination of the description of the GNI for tritium β decay, the analysis strategy, and the coverage studies, as previously outlined, enables the derivation of constraints on the GNI, when applied to data. Firstly, the exclusion contours for both GNI parameter spaces are presented. Subsequently, the relations described in section 7.2 are used to find constraints on individual interactions, which are then compared to other experimental constraints. In addition, constraints on more specific physics scenarios, such as a right-handed W boson, charged Higgs boson, and leptoquark, are explored.

7.5.1 Exclusion Contours for General Neutrino Interactions at KATRIN

When applying this analysis procedure to the KNM2 data set, no significant indication of a GNI-like spectral distortion could be identified in either case, with or without an additional heavy neutrino-mass state. Also, the uncertainties in both cases are dominated by statistics (see figures 7.10 and 7.11). Figure 7.6 presents the 95 % CL exclusion contour for the GNI; the region with high values of m^2_β is excluded. Furthermore, a correlation between m^2_β and b'_β can be observed, which makes it more challenging to constrain the latter. Consequently, the effect of additional charged currents on the neutrino-mass observable is slight [65]. The best fit is located at $b'_\beta = -0.94$ and $m^2_\beta = 0.11\,\mathrm{eV}^2$ with a significance with respect to the null hypothesis of $\Delta\chi^2 = \chi^2_{\mathrm{NH}} - \chi^2_{\mathrm{min}} = 0.003$, thus implying no statistical significance and a goodness-of-fit of $\chi^2_{\mathrm{min}} = 30.6$ (24 dof, p-value of 0.17). A combination of external

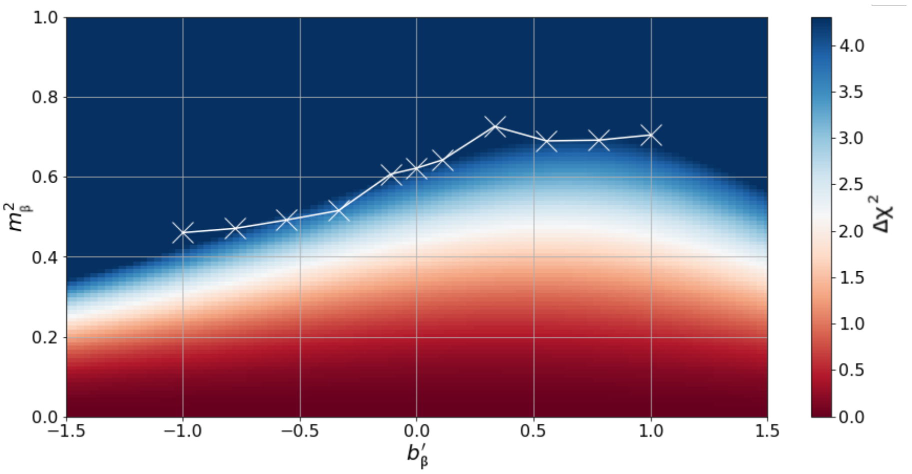

Figure 7.5: Evaluation of the full construction of confidence intervals to retrieve the χ^2_{crit}. The obtained ($m^2_{\beta,\,\mathrm{true}}$, $b'_{\beta,\,\mathrm{true}}$) values from the full construction (white crosses) are drawn on the $\Delta\chi^2$ map based on Asimov data to find the corresponding χ^2_{crit} value. The χ^2_{crit} for the parameter space without a heavy neutrino is found at 3.84.

constraints suggests $|b'| < 0.26$ (95 % CL) [65]. Furthermore, the projected final sensitivity for KATRIN after 1000 days measurement time was estimated using an Asimov data set assuming $m^2_\beta = 0\,\mathrm{eV}^2$. It is apparent that the sensitivity to m^2_β is considerably enhanced while the impact of b'_β is diminished for small neutrino masses.

The exclusion contours at 95 % CL for the GNI acting on an additional heavier neutrino-mass state are displayed in figure 7.7. In this primary analysis, the value of m^2_β was fixed to $0\,\mathrm{eV}^2$. The sensitivity contours visibly depend on b'_N: It enhances the kink-like signature due to the heavier mass state for negative values, whereas it diminishes the manifestation of the signal structure for more positive values. Moreover, the sensitivity is markedly enhanced in the higher-mass region. This will become relevant when KATRIN commences its search for keV sterile neutrinos with the planned TRISTAN detector upgrade [48, 202]. The best fit is found at $m^2_\mathrm{N} = 97.45\,\mathrm{eV}^2$, $\xi_\mathrm{N}/\xi_\beta = 0.005$, and $b'_\mathrm{N} = -1$ with a goodness-of-fit of $\chi^2_{\mathrm{min}} = 29.9$ (23 dof, p-value of 0.15). The significance of the best fit compared to the null hypothesis is $\Delta\chi^2 = 3.338$ and is thus not statistically significant.

Furthermore, the estimate of the projected final sensitivity corresponding to 1000 days measurement time at KATRIN demonstrates a substantial improvement of approximately one order of magnitude in terms of ξ_N/ξ_β. In addition, there is potential for a further order-of-magnitude improvement by eliminating parameter correlations with respect to E_0 through a more precise understanding of the absolute energy scale in KATRIN [205, 192]. Also an extension of the analysis interval of the data at hand from 40 eV to 90 eV below the endpoint yields up to one order of magnitude improvement in the high-mass region of $m^2_\mathrm{N} \approx 2000\,\mathrm{eV}^2$, while providing sensitivity to GNI for heavy neutrino masses up to $8100\,\mathrm{eV}^2$, as shown in a first study in figure 7.8. An even further extension of the analysis interval and therefore increased range of m^2_N to probe the GNI at, will become available with the upcoming TRISTAN upgrade. As the sensitivity to the effective GNI parameters scales with the neutrino mass, a markedly overall enhancement in sensitivity is expected, as predicted by a first sensitivity study shown in figure 7.9. For this study,

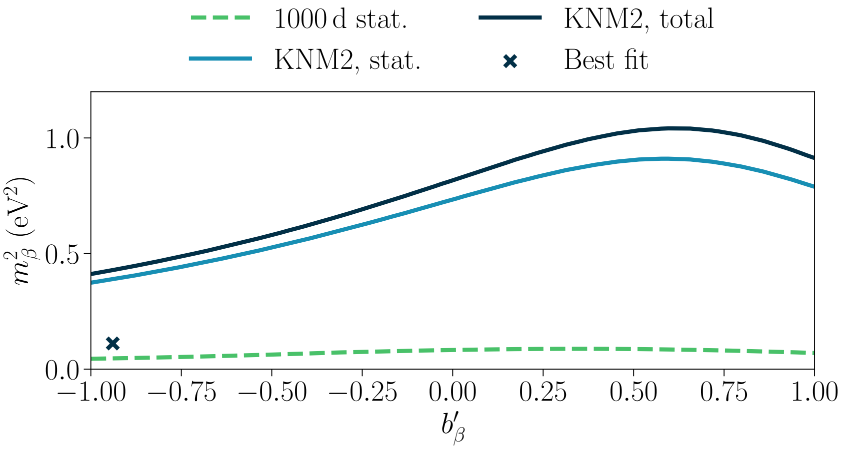

Figure 7.6: Exclusion contour for GNI contributions on the β-spectrum at 95 % CL based on the KNM2 data set. The contour is shown considering statistics only (stat.) and full systematics (total). The projected final sensitivity based on an Asimov data set with 1000 days statistics and $m_\beta^2 = 0\,\text{eV}^2$ is shown by the green dashed line.

the TRISTAN spectral model has been used, reflecting the differential mode in which the TRISTAN detector will measure the β spectrum.

An interplay between the spectral components attributed to the light and heavy neutrino-mass states can occur during the fitting procedure due to correlations between the fitted masses of light and heavy neutrinos. When treating m_β^2 as a free parameter, a loss in sensitivity for both high and low values of m_N^2 is observed. To avoid unphysically large negative m_β^2 values, a different constraint $0\,\text{eV}^2 < m_\beta^2 < m_N^2$ is also used. The resulting exclusion contour shown in figure 7.7 resembles the one using an unconstrained m_β^2 in the high-mass region, while regaining the sensitivity of the contour for fixed m_β^2 at low masses.

In the presented analysis all known systematic effects from the neutrino-mass analysis [17] are considered. The breakdown of systematic uncertainties on the contours is performed on a simulated data set with the neutrino mass set to zero. Grid scans are performed, wherein each systematic effect is considered separately. The analysis shows that the sensitivity of the contour is limited by statistics while the systematic effects only cause slight alterations. To quantitatively assess the relative contribution of each individual systematic effect [18], raster scans are performed. For each value of m_4^2 and b'_β, respectively, the 95 % CL contour for one degree of freedom is drawn, and the squared difference with respect to the statistics-only contour is calculated to obtain the pure systematic contribution. The impact of systematic effects on the GNI sensitivity is shown in figures 7.10 and 7.11. The low signal rate for small neutrino masses m_β and m_N gives relevance to the background-related systematics, such as the uncertainty on the non-Poissonian distributed background events and the scan-step-duration dependent background component coming from electrons stored in the Penning trap between the pre- and main spectrometers. Towards large values of m_N the signal-to-background ratio enlarges, reducing the relevance of the background systematics while highlighting the dominance of other systematics, such as the uncertainty contributions of the energy-loss function and the column density.

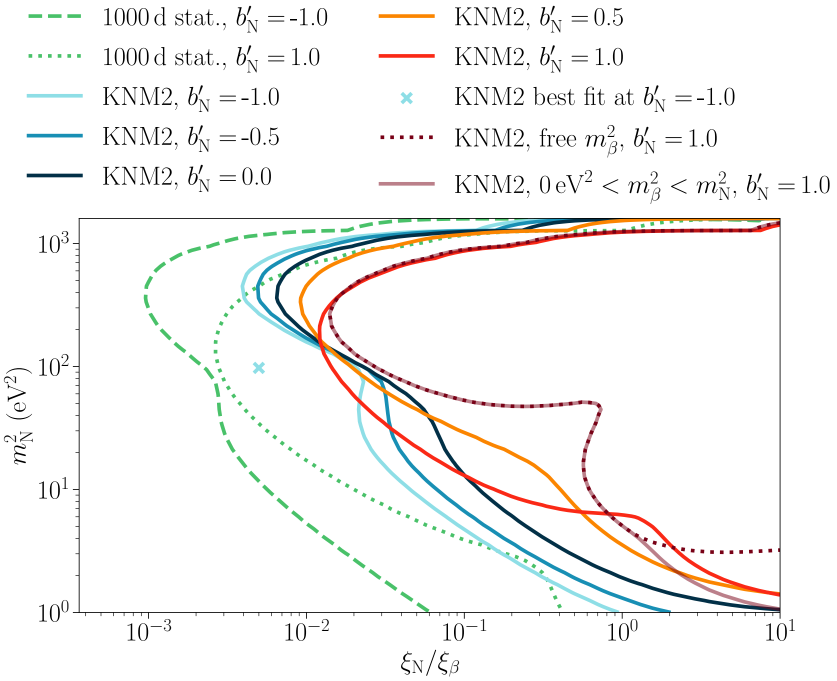

Figure 7.7: Exclusion contours for GNI contributions on an additional heavier neutrino-mass state at 95 % CL based on the KNM2 data set, taking into account full systematics. The two alternative treatments to fixing the light neutrino mass to $m^2_\beta = 0\,\text{eV}^2$ lead to the dark red contours. The projected final sensitivity for two different values of b'_N based on an Asimov data set with 1000 days statistics and $m^2_\beta = 0\,\text{eV}^2$ is shown by the dashed and dotted green lines.

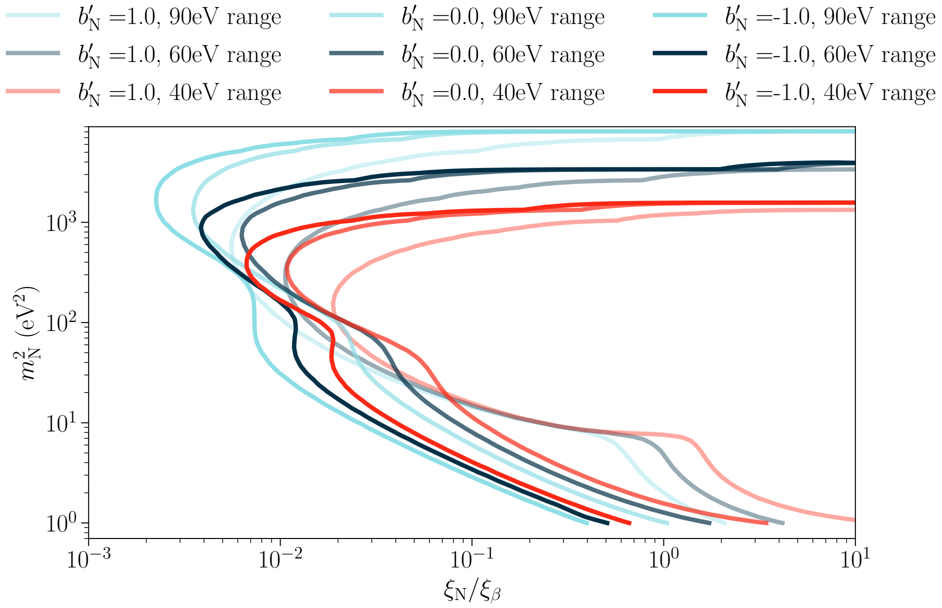

Figure 7.8: Sensitivity for GNI at 95 % CL for different extensions of the analysis interval based on Asimov data for KNM2. The analysis interval is extended from the standard 40-eV interval below the endpoint to 60 eV and 90 eV. Only statistical uncertainties are taken into account. An overall improvement in sensitivity is obtained.

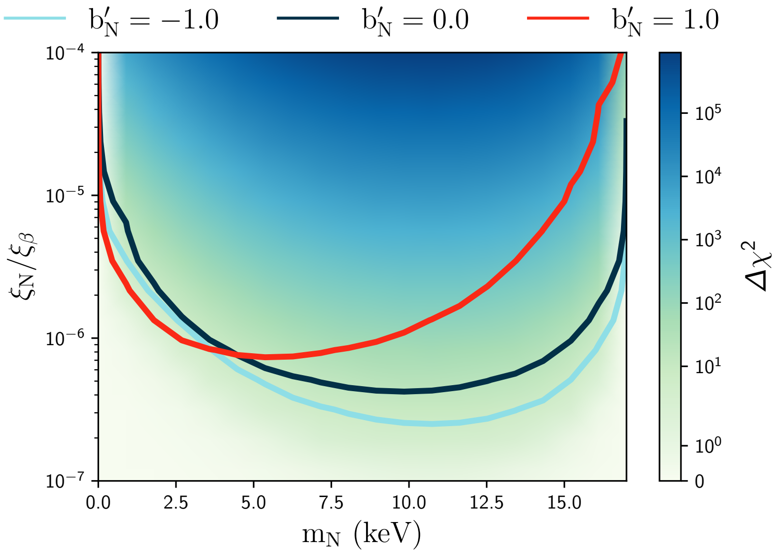

Figure 7.9: Estimated statistical sensitivity for GNI at 95 % CL with the TRISTAN detector upgrade, assuming the detection of 3.2×10^{14} events within the 17-keV interval below the endpoint over four months of measurement time. The impact of the systematic uncertainties is expected to reduce the sensitivity by about one order of magnitude, analogous to the sterile-neutrino search with TRISTAN, described in [86, 172].

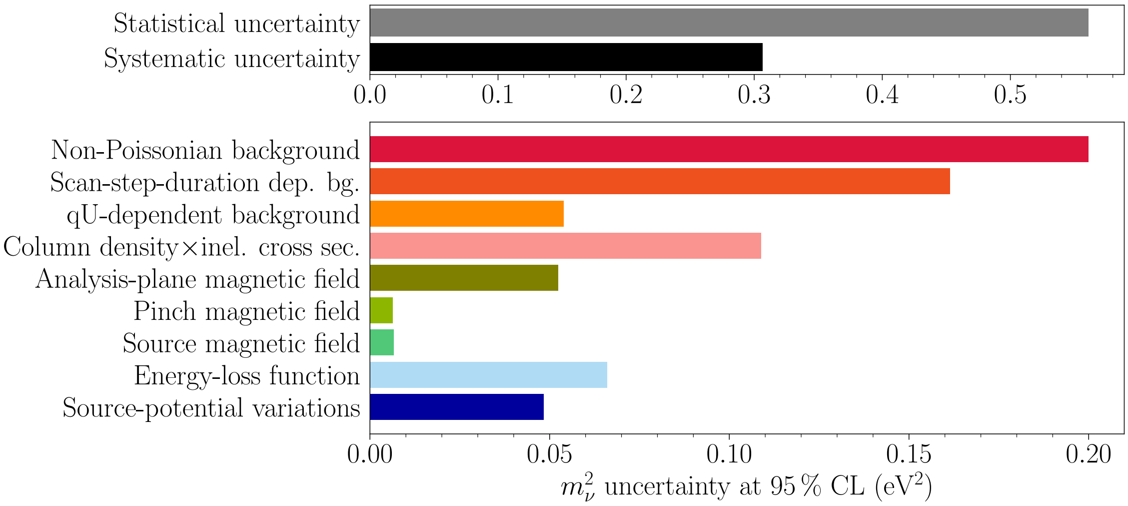

Figure 7.10: Uncertainty breakdown showing the impact of the KNM2 systematic effects on the GNI sensitivity contour based on the β-spectrum. The breakdown is shown for $b'_\beta = 0$ and obtained from a simulated data set without fluctuations with $m_\beta^2 = 0\,\text{eV}^2$. The uncertainty is dominated by its statistical component. The most significant systematic effects are the non-Poissonian and the scan-step-duration dependent background.

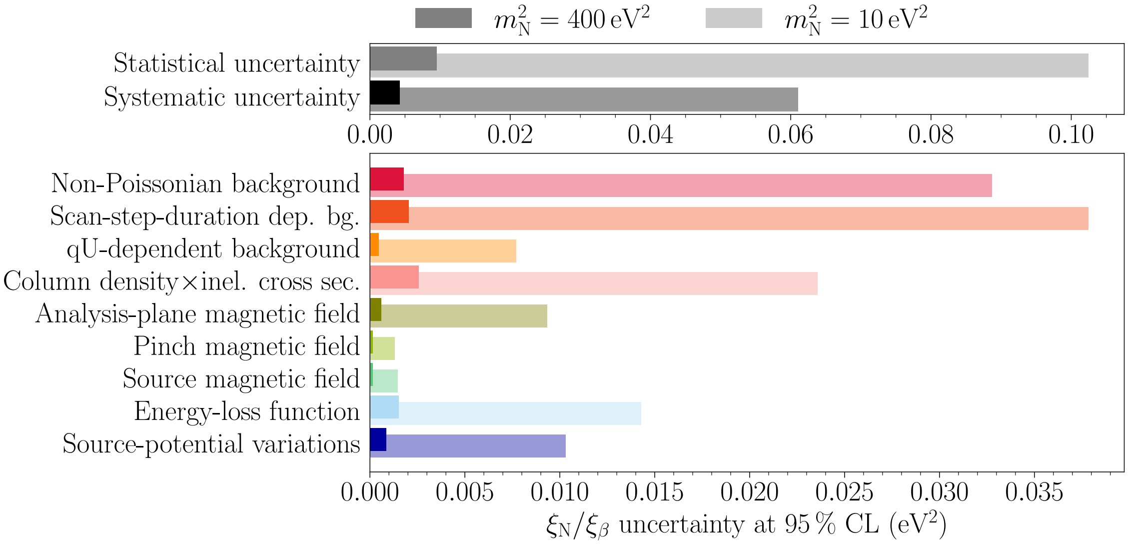

Figure 7.11: Uncertainty breakdown showing the impact of the KNM2 systematic effects on the GNI sensitivity contour taking into account the presence of an additional heavier neutrino (N). The breakdown is shown for the lower- and higher-mass region of the additional mass state with $b'_\text{N} = 0$ and obtained from a simulated data set without fluctuations with $m_\beta^2 = 0\,\text{eV}^2$. In both cases of m_N^2 the uncertainty is statistics dominated. In the lower-mass region the most significant systematic effects are the non-Poissonian and scan-step-duration dependent background, while the energy-loss function and column density gain significance towards the higher-mass region.

7.5.2 Constraints on individual General Neutrino Interaction couplings

The presented results can be placed into the context of other experiments by comparing the limits on individual types of GNI via their ϵ couplings. This is necessary since each of the different experimental approaches observes a different combination of ϵ couplings. Here, we compare our results to experiments utilizing lepton-flavour-conserving charged-current interactions, such as nuclear and neutron β decay, and π decay. A more comprehensive comparison between experiments within the neutrino sector would only be possible under additional assumptions regarding the coupling behaviour of the GNI. For instance, one might assume that the coupling strength is independent of the type of fermion. Furthermore, a comparison to high-energy processes is possible via the matching relations of the low-energy GNI terms to the SM(N)EFT Wilson coefficients.

The equations needed to place limits on the individual contributions of the ϵ_i and $\tilde{\epsilon}_i$ terms are derived in section 7.2. The values of the nuclear form factors are presented in table 7.1. When only considering light neutrinos, we assume a neutrino mass of $m_\beta^2 = 1\,\mathrm{eV}^2$ in figure 7.6 to provide an indication of the sensitivity of our data set to the magnitude of the individual ϵ_i contributions in a neutrino-mass regime in which this data set is sensitive to. We derive the following illustrative boundaries at 95 % CL: $\mathrm{Re}(T_{ei}\tilde{\epsilon}_\mathrm{L}) > -0.349$, $0.213 < \mathrm{Re}(T_{ei}\tilde{\epsilon}_\mathrm{R}) < 0.530$, $\mathrm{Re}(T_{ei}\tilde{\epsilon}_\mathrm{S}) > 1.952$, and $-0.227 < \mathrm{Re}(T_{ei}\tilde{\epsilon}_\mathrm{T}) < -0.083$. Strong correlations between m_β and b'_β visible in figure 7.6, and between $\tilde{\epsilon}_i$ and T_{ei} visible in equations 7.6 to 7.9 present a challenge in deriving competitive constraints on single ϵ_i contributions in comparison to the existing limits.

In the case of a heavy neutrino, our constraints on $\tilde{\epsilon}_i$ are derived from our high-sensitivity region at $m_\mathrm{N}^2 = 400\,\mathrm{eV}^2$ and summarized in table 7.2. For all calculations we assume $\sum |U_{ei}| = \sum |V_{ei}| \approx 1$. Constraints on ϵ_i would require additional assumptions on T_{ei} and S_{ei}, and a left-right-symmetric coupling behaviour of the GNI.

Given that the impact of the GNI on the β spectrum scales with the mass of the neutrino, our investigations yield the most stringent constraints when including a heavier neutrino N. KATRIN's new constraints are distinguished by a precise, direct measurement of the spectral shape of the β decay with the lowest energy of 18.6 keV. Existing limits (see table 7.2) are derived at vastly different energy scales and with disparate experimental approaches. When compared with global analyses combining properties of β-decay transitions, neutron lifetimes, and neutron decay correlation coefficients, competitive bounds on $\tilde{\epsilon}_i$ are derived for the left-handed vector and tensor interactions from only 5 % of the expected final KATRIN data set. The bound for the scalar interaction is less than one order of magnitude weaker than the competing constraints from global β-decay analyses. The projected final sensitivity will enable a further improvement in these limits by about a factor of three. The LHC's searches for missing-transverse-energy processes at 8 TeV yield indirect constraints by matching the Wilson coefficients of a high-energy EFT to the GNI couplings. This approach has noticeable dependencies on the energy scale, which benefits the sensitivity to these coefficients. The constraints are overall one order of magnitude stronger compared to the current β-decay investigations and their bounds will come into reach for the full KATRIN data set. Moreover, the strong scale dependence of the couplings between the markedly disparate energy scales has not yet been adequately taken into account [76, 61].

The TRISTAN detector upgrade permits to extend the mass scale of the additional heavier neutrino-mass state for the GNI search to the keV region. Expected sensitivities on individual interactions are estimated based on the predicted sensitivity shown in figure 7.9,

Table 7.2: Overview of 90 % CL bounds on the GNI coefficients $\tilde{\epsilon}_{i,\,\mathrm{ud}}^{\mathrm{ee11}}$ from various low- and high-energy searches, obtained with different experimental approaches. The indirect constraints by LHC are obtained at 8 TeV, evaluating processes with missing transverse energy (MET). Global analyses combine properties of β-decay transitions, neutron lifetimes, and neutron decay correlation coefficients to find constraints at $\mathcal{O}(100\,\mathrm{keV})$ to $\mathcal{O}(1\,\mathrm{MeV})$. The bounds in this work are solely derived from the spectral shape of the β decay with the lowest energy of 18.6 keV. They assume $m_\mathrm{N}^2 = 400\,\mathrm{eV}^2$ and reflect the range of allowed values for b'_N.

Bound (90 % CL)	Source	Reference
$\mathrm{Re}(\tilde{\epsilon}_\mathrm{L}) < 0.06$	Global β-decay analysis	[75]
$\lvert\tilde{\epsilon}_\mathrm{L}\rvert < 0.057 - 0.118$	KATRIN	this work
$\lvert\tilde{\epsilon}_\mathrm{R}\rvert < 2.2 \cdot 10^{-3}$	LHC (MET) via matching	[174]
$\lvert\tilde{\epsilon}_\mathrm{R}\rvert < 0.057 - 0.118$	KATRIN	this work
$\lvert\tilde{\epsilon}_\mathrm{S}\rvert \leq 0.063$	Global β-decay analysis using CKM unitarity	[117]
$\lvert\tilde{\epsilon}_\mathrm{S}\rvert < 5.8 \cdot 10^{-3}$	LHC (MET) via matching	[174]
$\lvert\tilde{\epsilon}_\mathrm{S}\rvert < 0.134 - 0.278$	KATRIN	this work
$6 \cdot 10^{-3} \leq \lvert\tilde{\epsilon}_\mathrm{T}\rvert \leq 0.024$	Global β-decay analysis	[117]
$\lvert\tilde{\epsilon}_\mathrm{T}\rvert < 1.3 \cdot 10^{-3}$	LHC (MET) via matching	[174]
$\lvert\tilde{\epsilon}_\mathrm{T}\rvert < 0.020 - 0.042$	KATRIN	this work

taking into account a loss in sensitivity of approximately one order of magnitude due to systematic uncertainties. Consequently, the sensitivity to the individual interactions is predicted to be below the following bounds, given a heavy neutrino of a few keV: to $\tilde{\epsilon}_L$ and $\tilde{\epsilon}_R$ below 3.2×10^{-3}, to $\tilde{\epsilon}_S$ below 7.5×10^{-3}, and to $\tilde{\epsilon}_T$ below 1.1×10^{-3}. These predictions imply the setting of leading constraints for all interaction channels among β-decay experiments and the derivation of competitive constraints with regard to the high-energy investigations at the LHC.

Furthermore, we examine simultaneous constraints on more than one interaction type. In this study, we have selected combinations that may provide indications of the existence of specific new-physics scenarios. The resulting contours are presented in figure 7.12 for $m_\mathrm{N}^2 = 400\,\mathrm{eV}^2$ and b'_N between -1 and 1. Two values for the unknown mixing S are explored: an external, conservative constraint of $S = 0.0727$ from $0\nu\beta\beta$-decay [20, 138] and a small mixing of $S = 10^{-5}$.

The W boson, which mediates the β decay, only couples to left-handed fermions. Incorporating right-handed neutrino states into our theoretical framework enables the existence of a right-handed vector-current interaction, which may be mediated by a right-handed W boson [169, 170]. This scenario would thus necessitate both ϵ_L and $\tilde{\epsilon}_\mathrm{R}$ to be non-zero. Both $S \cdot \epsilon_\mathrm{L}$ and $\tilde{\epsilon}_\mathrm{R}$ can be simultaneously constrained at the order of 10^{-1}. Furthermore, the GNI introduce scalar charged-current interactions, represented by ϵ_S and $\tilde{\epsilon}_\mathrm{S}$, which can indicate the existence of a charged Higgs boson [217, 73]. The exclusion contours in

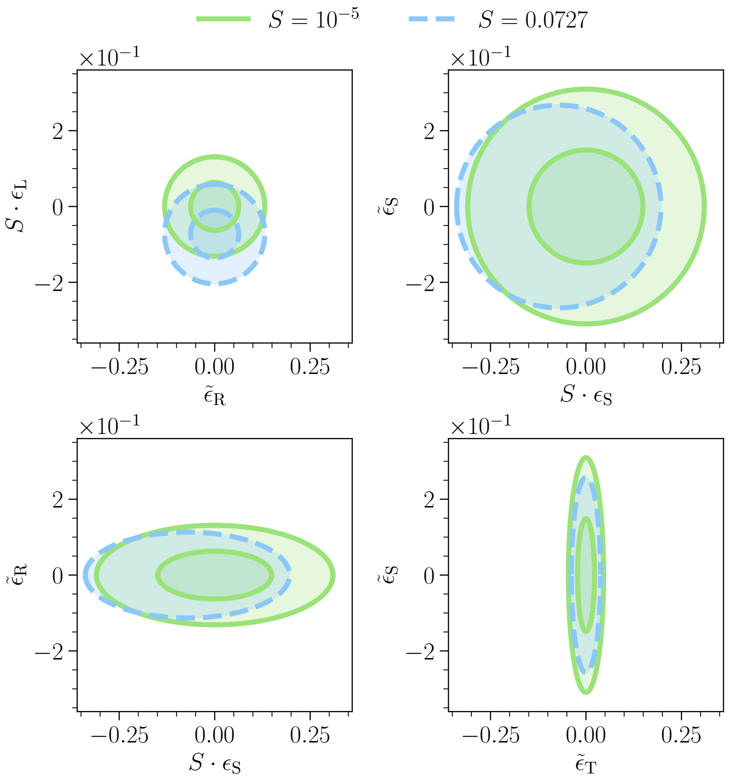

Figure 7.12: 95 % CL exclusion contours for selected combinations of ϵ_i and $\tilde{\epsilon}_i$ derived from the exclusion contours on KNM2 data assuming $m_\beta^2 = 0\,\mathrm{eV}^2$ for the high-sensitivity region at $m_\mathrm{N}^2 = 400\,\mathrm{eV}^2$. Coloured regions display the not excluded region in the range of b'_N between -1 and 1, and depend on the choice of mixing parameter S. If parameters run out of their defined range, only the contour for $b'_\mathrm{N} = 1$ is shown.

figure 7.12 demonstrate that if such a charged scalar interaction couples both to left- and right-handed neutrinos, the bounds on both $S \cdot \epsilon_\mathrm{S}$ and $\tilde{\epsilon}_\mathrm{S}$ are below 0.35. Additionally, we present the constraints on the combination of the couplings ϵ_S and $\tilde{\epsilon}_\mathrm{R}$, which may provide insights into the combined interaction of a charged Higgs boson acting on the left-handed neutrino state and a right-handed W boson. The constraints are at an 10^{-1} level for $\tilde{\epsilon}_\mathrm{R}$ while encountering a factor of 2 lower sensitivity in the $S \cdot \epsilon_\mathrm{S}$ dimension. Finally, the matching relations in [61] enable us to derive which interactions would be needed to realise various leptoquark models [179]. These would serve as a unified approach to UV completion of the effective GNI theory [61]. As an illustrative example we present the combination of the couplings $\tilde{\epsilon}_\mathrm{S}$ and $\tilde{\epsilon}_\mathrm{T}$ for the scalar colour-triplet leptoquark R'_2, as defined in [61] and table 2.2. We constrain $\tilde{\epsilon}_\mathrm{T}$ to a precision of below 5×10^{-2} while the constraint on $\tilde{\epsilon}_\mathrm{S}$ is about half an order of magnitude larger. The combination with one other scalar colour-triplet leptoquark S_1 is of interest as it allows for the explanation of B physics anomalies [69], and is able to generate radiative neutrino masses at one-loop level [147]. The above investigated combinations, namely ϵ_L and $\tilde{\epsilon}_\mathrm{R}$, ϵ_S and $\tilde{\epsilon}_\mathrm{S}$, and $\tilde{\epsilon}_\mathrm{S}$ and $\tilde{\epsilon}_\mathrm{T}$, are expected to occur in the presence of the S_1 leptoquark.

8. Summary and Conclusion

The high-statistics spectra of the tritium β decay recorded by KATRIN allow to go beyond the neutrino mass determination and examine multiple scenarios related to beyond-the-standard-model physics. This work presents the first search for general neutrino interactions at the KATRIN experiment. We derived an effective description of general neutrino interactions in tritium β decay and applied this model to the data of the second KATRIN measurement campaign. In these investigations, the possibility of the existence of an additional heavier neutrino with $m_\mathrm{N}^2 \leq 1600\,\mathrm{eV}^2$ was considered. In the absence of a significant signal for general neutrino interactions, we present the exclusion contours at 95 % CL on the effective GNI parameters. In order to realise these results, a suitable analysis procedure was designed, and the spectral model was derived and implemented in the KASPER software. Further improvements of the fit performance and routines in both the KASPER framework and the supporting analysis environment ensure the robustness of the analysis procedure, preparing it for future investigations using larger data sets and analysis intervals.

The impact of systematic effects was studied in detail for both the case with and without the inclusion of an additional heavier neutrino in our model. We have shown, that our sensitivity is clearly statistics-limited for the KNM2 data set. The systematic uncertainty breakdown furthermore demonstrates, that the sensitivity in the lower neutrino-mass range is mainly influenced by the background-related systematic uncertainties, while the systematic uncertainties on the column density and energy-loss function become more prominent for $\mathcal{O}(100\,\mathrm{eV}^2)$ neutrino masses.

We derived constraints on the coupling strength of single types of interactions on right-handed neutrinos, designated as $\tilde{\epsilon}_i$. Thereby, we are able to place competitive constraints with respect to global analyses on β-decay processes for left-handed vector and tensor interactions for high masses of an additional neutrino with $m_\mathrm{N}^2 = 400\,\mathrm{eV}^2$. Indirect constraints from high-energy investigations at the LHC prove to be about one order of magnitude more sensitive, although being subject to noticeable energy dependencies of the couplings, which have not yet been adequately taken into account for the comparison with the results of KATRIN.

Furthermore, we investigated more specific new physics scenarios, including a right-handed W boson, charged Higgs boson, and scalar leptoquark, by drawing exclusion contours for selected combinations of the coupling strengths, ϵ_i and $\tilde{\epsilon}_i$.

With the full data set of KATRIN collected until 2025, a significant threefold enhancement in GNI sensitivity is expected, which would entail setting leading constraints among β-decay experiments. An extension of the analysis interval below the endpoint would further increase the sensitivity, both in the ξ_N dimension and towards higher neutrino masses

m_{N}^2. As the sensitivity to the effective GNI parameters scales with the neutrino mass, the planned detector update TRISTAN, designed to search for keV-scale sterile neutrinos, promises significant future potential for further GNI searches.

List of Acronyms

BAO Baryonic Acoustic Oscillations

BIXS Beta Induced X-ray Spectroscopy

BSM Beyond the Standard Model

CEvNS Coherent Elastic Neutrino Nucleus Scattering

CL Confidence Level

CMB Cosmic Microwave Background

cps counts per second

CPS Cryogenic Pumping Section

DAQ Data Acquisition

DESI Dark Energy Spectroscopic Instrument

dof degrees of freedom

DPS Differential Pumping Section

EFT Effective Field Theory

e-gun electron-gun

EMCS Earth Magnetic field Compensation System

FBM Forward Beam Monitor

FPD	Focal Plane Detector
FSD	Final-States Distribution
GNI	General Neutrino Interactions
IO	Inverted Ordering
KaFit	KATRIN Fit environment
KATRIN	Karlsruhe Tritium Neutrino Experiment
KIT	Karlsruhe Institute of Technology
KNM	KATRIN Neutrino-mass Measurement campaign
LARA	Laser Raman spectroscopy system
LEFT	Low-Energy Effective Field Theory
LFCS	Low-Field Correction System
LFV	Lepton Flavour Violation
LHC	Large Hadron Collider
MAC-E	Magnetic Adiabatic Collimation with Electrostatic
MC	Monte Carlo
MCMC	Markov Chain Monte Carlo
MET	Missing Transverse Energy
MLE	Maximum Likelihood Estimation
MSW	Mikheyev–Smirnov–Wolfenstein
MTD	Measurement Time Distribution

NEG Non-Evaporating Getter pumps

NH Null Hypothesis

NO Normal Ordering

NSI Neutrino Non-Standard Interactions

PAE Post Acceleration Electrode

PDF Probability Density Function

QCD Quantum Chromodynamics

QFT Quantum Field Theory

RW Rear Wall

SDD Silicon Drift Detector

SM Standard Model

SMEFT Standard Model Effective Field Theory

SM(N)EFT (sterile-neutrino extended) Standard Model Effective Field Theory

SSB Spontaneous Symmetry Breaking

SSC Source and Spectrum Calculation

TMP Turbo Molecular Pumps

UV Ultra Violet

vev vacuum expectation value

WGTS Windowless Gaseous molecular Tritium Source

List of Figures

List of Tables

Bibliography

[1] R. Abbasi et al. "Measurement of atmospheric neutrino mixing with improved IceCube DeepCore calibration and data processing". In: *Physical Review D* 108 (1 July 2023), p. 012014. DOI: 10.1103/PHYSREVD.108.012014.

[2] D. N. Abdurashitov et al. "Electron scattering on hydrogen and deuterium molecules at 14–25 keV by the "Troitsk nu-mass" experiment". In: *Physics of Particles and Nuclei Letters* 14.6 (Nov. 2017), pp. 892–899. DOI: 10.1134/S1547477117060024.

[3] J. N. Abdurashitov et al. "Results from SAGE (The Russian-American gallium solar neutrino experiment)". In: *Physics Letters B* 328.1-2 (May 1994), pp. 234–248. DOI: 10.1016/0370-2693(94)90454-5.

[4] K. Abe et al. "Atmospheric neutrino oscillation analysis with external constraints in Super-Kamiokande I-IV". In: *Physical Review D* 97.7 (Apr. 2018), p. 072001. DOI: 10.1103/PHYSREVD.97.072001.

[5] K. Abe et al. *Hyper-Kamiokande Design Report.* 2018. arXiv: 1805.04163 [physics.ins-det].

[6] K. Abe et al. "Measurements of neutrino oscillation parameters from the T2K experiment using 3.6×10^21 protons on target". In: *The European Physical Journal C* 83.9 (Sept. 2023), pp. 1–50. DOI: 10.1140/EPJC/S10052-023-11819-X.

[7] K. Abe et al. "Solar neutrino measurements in Super-Kamiokande-IV". In: *Physical Review D* 94.5 (Sept. 2016), p. 052010. DOI: 10.1103/PHYSREVD.94.052010.

[8] S. Abe et al. "Search for the Majorana Nature of Neutrinos in the Inverted Mass Ordering Region with KamLAND-Zen". In: *Physical Review Letters* 130.5 (Feb. 2023), p. 051801. DOI: 10.1103/PHYSREVLETT.130.051801.

[9] B. Abi et al. "Volume I. Introduction to DUNE". In: *Journal of Instrumentation* 15.08 (Aug. 2020), T08008–T08008. DOI: 10.1088/1748-0221/15/08/T08008.

[10] M. A. Acero et al. "Improved measurement of neutrino oscillation parameters by the NOvA experiment". In: *Physical Review D* 106.3 (Aug. 2022), p. 032004. DOI: 10.1103/PHYSREVD.106.032004.

[11] H. Acharya et al. *Measurement of the inhomogeneity of the KATRIN tritium source electric potential by high-resolution spectroscopy of conversion electrons from* ^{83m}*Kr.* Mar. 2025. arXiv: 2503.13221 [nucl-ex].

[12] P. Adamson et al. "Precision Constraints for Three-Flavor Neutrino Oscillations from the Full MINOS+ and MINOS Dataset". In: *Physical Review Letters* 125.13 (Sept. 2020), p. 131802. DOI: 10.1103/PHYSREVLETT.125.131802.

[13] M. Agostini et al. "Simultaneous precision spectroscopy of pp, 7Be, and pep solar neutrinos with Borexino Phase-II". In: *Physical Review D* 100.8 (Oct. 2019), p. 082004. DOI: 10.1103/PHYSREVD.100.082004.

[14] Q. R. Ahmad et al. "Direct Evidence for Neutrino Flavor Transformation from Neutral-Current Interactions in the Sudbury Neutrino Observatory". In: *Physical Review Letters* 89.1 (June 2002), p. 011301. DOI: 10.1103/PhysRevLett.89.011301.

[15] M. Aker et al. "Suppression of Penning discharges between the KATRIN spectrometers". In: *The European Physics Journal C* 80.9 (2020), p. 821. DOI: 10.1140/epjc/s10052-020-8278-y.

[16] M. Aker et al. "Analysis methods for the first KATRIN neutrino-mass measurement". In: *Physical Review D* 104.1 (July 2021), p. 012005. DOI: 10.1103/PhysRevD.104.012005.

[17] M. Aker et al. *Direct neutrino-mass measurement based on 259 days of KATRIN data*. June 2024. arXiv: 2406.13516 [nucl-ex].

[18] M. Aker et al. "Direct neutrino-mass measurement with sub-electronvolt sensitivity". In: *Nature Physics* 18.2 (Feb. 2022), pp. 160–166. DOI: 10.1038/s41567-021-01463-1.

[19] M. Aker et al. *First constraints on general neutrino interactions based on KATRIN data*. Oct. 2024. arXiv: 2410.13895 [nucl-ex].

[20] M. Aker et al. "Improved eV-scale sterile-neutrino constraints from the second KATRIN measurement campaign". In: *Physical Review D* 105.7 (Apr. 2022), p. 072004. DOI: 10.1103/PhysRevD.105.072004.

[21] M. Aker et al. "Improved Upper Limit on the Neutrino Mass from a Direct Kinematic Method by KATRIN". In: *Physical Review Letters* 123.22 (Nov. 2019), p. 221802. DOI: 10.1103/PhysRevLett.123.221802.

[22] M. Aker et al. "Measurement of the electric potential and the magnetic field in the shifted analysing plane of the KATRIN experiment". In: (Aug. 2024). URL: http://arxiv.org/abs/2408.07022.

[23] M. Aker et al. "Precision measurement of the electron energy-loss function in tritium and deuterium gas for the KATRIN experiment". In: *The European Physical Journal C* 81.7 (May 2021). DOI: 10.1140/epjc/s10052-021-09325-z.

[24] M. Aker et al. "Search for Lorentz-invariance violation with the first KATRIN data". In: *Physical Review D* 107.8 (Apr. 2023), p. 082005. DOI: 10.1103/PhysRevD.107.082005.

[25] M. Aker et al. "The design, construction, and commissioning of the KATRIN experiment". In: *Journal of Instrumentation* 16.08 (Aug. 2021), T08015. DOI: 10.1088/1748-0221/16/08/T08015.

[26] D. Akimov et al. "Observation of coherent elastic neutrino-nucleus scattering". In: *Science* 357.6356 (Sept. 2017), pp. 1123–1126. DOI: 10.1126/SCIENCE.AAO0990.

[27] Y. A. Akulov and B. A. Mamyrin. "Determination of the ratio of the axial-vector to the vector coupling constant for weak interaction in triton beta decay". In: *Physics of Atomic Nuclei* 65.10 (Oct. 2002), pp. 1795–1797. DOI: 10.1134/1.1515842.

[28] Alexander Curt Marsteller. "Characterization and Optimization of the KATRIN Tritium Source". PhD thesis. Karlsruhe Institute of Technology, 2020. DOI: 10.5445/IR/1000127553.

[29] B. K. Alpert et al. *Most stringent bound on electron neutrino mass obtained with a scalable low temperature microcalorimeter array*. 2025. arXiv: 2503.19920 [hep-ex].

[30] D. W. P. Amaral et al. “A direct detection view of the neutrino NSI landscape”. In: *Journal of High Energy Physics* 71 (July 2023). DOI: 10.1007/JHEP07(2023)071.

[31] J. F. Amsbaugh et al. “Focal-plane detector system for the KATRIN experiment”. In: *Nuclear Instruments and Methods in Physics Research Section A: Accelerators, Spectrometers, Detectors and Associated Equipment* 778 (Apr. 2015), pp. 40–60. DOI: 10.1016/J.NIMA.2014.12.116.

[32] F. P. An et al. “New measurement of θ_{13} via neutron capture on hydrogen at Daya Bay”. In: *Physical Review D* 93.7 (Apr. 2016), p. 072011. DOI: 10.1103/PHYSREVD.93.072011.

[33] F. P. An et al. “Precision Measurement of Reactor Antineutrino Oscillation at Kilometer-Scale Baselines by Daya Bay”. In: *Physical Review Letters* 13.16 (Apr. 2023), p. 161802. DOI: 10.1103/PHYSREVLETT.130.161802.

[34] A. Angelescu et al. “Closing the window on single leptoquark solutions to the B-physics anomalies”. In: *Journal of High Energy Physics* 2018.10 (Oct. 2018), pp. 1–33. DOI: 10.1007/JHEP10(2018)183.

[35] Anna Katharina Schaller. “Characterization and mitigation of the background in KATRIN”. PhD thesis. Technical University of Munich, 2020. URL: https://mediatum.ub.tum.de/doc/1553598/1553598.pdf.

[36] S. Antusch, J. Baumann, and E. Fernández-Martínez. “Non-standard neutrino interactions with matter from physics beyond the Standard Model”. In: *Nuclear Physics B* 810.1-2 (Mar. 2009), pp. 369–388. DOI: 10.1016/j.nuclphysb.2008.11.018.

[37] D. Aristizabal Sierra, V. De Romeri, and N. Rojas. “COHERENT analysis of neutrino generalized interactions”. In: *Physical Review D* 98.7 (Oct. 2018), p. 075018. DOI: 10.1103/PhysRevD.98.075018.

[38] V. Aseev et al. “Energy loss of 18 keV electrons in gaseous T and quench condensed D films”. In: *The European Physical Journal D* 10.1 (Mar. 2000), pp. 39–52. DOI: 10.1007/s100530050525.

[39] A. Ashtari Esfahani et al. “Tritium Beta Spectrum Measurement and Neutrino Mass Limit from Cyclotron Radiation Emission Spectroscopy”. In: *Physical Review Letters* 131 (10 Sept. 2023), p. 102502. DOI: 10.1103/PhysRevLett.131.102502.

[40] K. S. Babu and C. N. Leung. “Classification of effective neutrino mass operators”. In: *Nuclear Physics B* 619.1 (Dec. 2001), pp. 667–689. DOI: 10.1016/S0550-3213(01)00504-1.

[41] M. Babutzka. “Design and development for the Rearsection of the KATRIN experiment”. PhD thesis. Karlsruhe Institute of Technology, 2014. DOI: 10.5445/IR/1000045598.

[42] J. N. Bahcall. “Solar Neutrinos. I. Theoretical”. In: *Physical Review Letters* 12.11 (Mar. 1964), p. 300. DOI: 10.1103/PhysRevLett.12.300.

[43] J. N. Bahcall and R. Davis. “Solar neutrinos: A scientific puzzle”. In: *Science* 191.4224 (Jan. 1976), pp. 264–267. DOI: 10.1126/SCIENCE.191.4224.264.

[44] G. Bak et al. “Measurement of Reactor Antineutrino Oscillation Amplitude and Frequency at RENO”. In: *Physical Review Letters* 121.20 (Nov. 2018), p. 201801. DOI: 10.1103/PHYSREVLETT.121.201801.

[45] A. M. Baldini et al. “Search for the lepton flavour violating decay $\mu^+ \to \mathrm{e}^+\gamma$ with the full dataset of the MEG experiment”. In: *The European Physical Journal C* 76.8 (Aug. 2016), pp. 1–30. DOI: `10.1140/EPJC/S10052-016-4271-X`.

[46] I. K. Banerjee et al. “PTOLEMY’s test of generalized neutrino interactions: unveiling challenges and constraints”. In: *Journal of Cosmology and Astroparticle Physics* 2024.04 (Apr. 2024), p. 002. DOI: `10.1088/1475-7516/2024/04/002`.

[47] J. Barranco et al. “Constraining nonstandard neutrino-electron interactions”. In: *Physical Review D* 77.9 (May 2008), p. 093014. DOI: `10.1103/PHYSREVD.77.093014`.

[48] J. Barry, J. Heeck, and W. Rodejohann. “Sterile neutrinos and right-handed currents in KATRIN”. In: *Journal of High Energy Physics* 7 (July 2014), pp. 1–23. DOI: `10.1007/JHEP07(2014)081`.

[49] M. Bauer and M. Neubert. “Minimal Leptoquark Explanation for the $R_{D^{(*)}}$,R_K, and $(\mathrm{g}\text{-}2)_\mu$ Anomalies”. In: *Physical Review Letters* 116.14 (Apr. 2016), p. 141802. DOI: `10.1103/PHYSREVLETT.116.141802`.

[50] G. Beamson, H. Q. Porter, and D. W. Turner. “The collimating and magnifying properties of a superconducting field photoelectron spectrometer”. In: *Journal of Physics E: Scientific Instruments* 13.1 (Jan. 1980), pp. 64–66. DOI: `10.1088/0022-3735/13/1/018`.

[51] D. Bečirević et al. “Leptoquark model to explain the B-physics anomalies, R_K and R_D”. In: *Physical Review D* 94.11 (Dec. 2016), p. 115021. DOI: `10.1103/PHYSREVD.94.115021`.

[52] A. Beglarian et al. “KATRIN design report”. In: *Wissenschaftliche Berichte FZKA* (2004). URL: `www.katrin.kit.edu/publikationen/DesignReport2004-12Jan2005.pdf`.

[53] J. Behrends. “Design and commissioning of a monoenergetic photoelectron source and active background reduction by magnetic pulse at the KATRIN experiment”. PhD thesis. University of Münster, 2017. URL: `https://www.katrin.kit.edu/publikationen/phd_behrens.pdf`.

[54] U. Bellgardt et al. “Search for the decay $\mu^+ \to e^+e^+e^-$”. In: *Nuclear Physics B* 299.1 (Mar. 1988), pp. 1–6. DOI: `10.1016/0550-3213(88)90462-2`.

[55] S. Bergmann, Y. Grossman, and E. Nardi. “Neutrino propagation in matter with general interactions”. In: *Physical Review D* 60.9 (Oct. 1999), p. 093008. DOI: `10.1103/PhysRevD.60.093008`.

[56] W. Bertl et al. “A search for μ-e conversion in muonic gold”. In: *The European Physical Journal C* 47.2 (May 2006), pp. 337–346. DOI: `10.1140/EPJC/S2006-02582-X`.

[57] T. Bhattacharya et al. “Axial, scalar, and tensor charges of the nucleon from $2+1+1$-flavor Lattice QCD”. In: *Physical Review D* 94 (2016), p. 054508. DOI: `10.1103/PhysRevD.94.054508`.

[58] M. Bilenky and A. Santamaria. “One-loop effective lagrangian for an extension of the standard model with a heavy charged scalar singlet”. In: *Nuclear Physics B* 420.1-2 (May 1994), pp. 47–93. DOI: `10.1016/0550-3213(94)90375-1`.

[59] S. Bilenky. *Introduction to the Physics of Massive and Mixed Neutrinos*. Vol. 817. Lecture Notes in Physics. Berlin, Heidelberg: Springer Berlin Heidelberg, 2010. DOI: `10.1007/978-3-642-14043-3`.

[60] I. Bischer and W. Rodejohann. “General neutrino interactions at the DUNE near detector”. In: *Physical Review D* 99.3 (Feb. 2019), p. 036006. DOI: `10.1103/PHYSREVD.99.036006`.

[61] I. Bischer and W. Rodejohann. “General neutrino interactions from an effective field theory perspective”. In: *Nuclear Physics B* 947 (2019). DOI: `10.1016/j.nuclphysb.2019.114746`.

[62] I. Bischer, W. Rodejohann, and X.-J. Xu. “Loop-induced neutrino non-standard interactions”. In: *Journal of High Energy Physics* 10 (Oct. 2018), p. 96. DOI: `10.1007/JHEP10(2018)096`.

[63] I. F. Bischer. “Effective Neutrino Interactions: Origins and Phenomenology”. PhD thesis. Heidelberg University, 2021. DOI: `10.11588/heidok.00030163`.

[64] M. Blennow et al. “A combined study of source, detector and matter non-standard neutrino interactions at DUNE”. In: *Journal of High Energy Physics* 8 (Aug. 2016), p. 90. DOI: `10.1007/JHEP08(2016)090`.

[65] J. Bonn et al. “The KATRIN sensitivity to the neutrino mass and to right-handed currents in beta decay”. In: *Physics Letters B* 703.3 (Sept. 2011), pp. 310–312. DOI: `10.1016/J.PHYSLETB.2011.08.005`.

[66] M. Borghesi et al. “An updated overview of the HOLMES status”. In: *Nuclear Instruments and Methods in Physics Research, Section A: Accelerators, Spectrometers, Detectors and Associated Equipment* 1051 (2023). DOI: `10.1016/j.nima.2023.168205`.

[67] W. Buchmüller, R. Rückl, and D. Wyler. “Leptoquarks in lepton-quark collisions”. In: *Physics Letters B* 191.4 (1987), pp. 442–448. DOI: `10.1016/0370-2693(87)90637-X`.

[68] L. Calibbi and G. Signorelli. “Charged lepton flavour violation: An experimental and theoretical introduction”. In: *Rivista del Nuovo Cimento* 41.2 (Feb. 2018), pp. 71–174. DOI: `10.1393/NCR/I2018-10144-0`.

[69] O. Cata and T. Mannel. *Linking lepton number violation with B anomalies*. 2019. arXiv: `1903.01799 [hep-ph]`.

[70] J. Chadwick. “Intensitätsverteilung im magnetischen Spectrum der β-Strahlen von radium B + C”. In: *Verhandl. Dtsc. Phys. Ges.* 16 (1914), p. 383. URL: `https://cds.cern.ch/record/262756`.

[71] W. F. Chang et al. “Charged lepton flavor violating processes and scalar leptoquark decay branching ratios in the colored Zee-Babu model”. In: *Journal of High Energy Physics* 10 (Oct. 2016), pp. 1–26. DOI: `10.1007/JHEP10(2016)106`.

[72] Z. Chen, T. Li, and J. Liao. “Constraints on general neutrino interactions with exotic fermion from neutrino-electron scattering experiments”. In: *Journal of High Energy Physics* 5 (May 2021), pp. 1–18. DOI: `10.1007/JHEP05(2021)131`.

[73] T. P. Cheng and L.-F. Li. “Neutrino masses, mixings, and oscillations in SU(2)×U(1) models of electroweak interactions”. In: *Physical Review D* 22.11 (Dec. 1980), pp. 2860–2868. DOI: `10.1103/PhysRevD.22.2860`.

[74] Y. Chikashige, R. Mohapatra, and R. Peccei. “Are there real goldstone bosons associated with broken lepton number?” In: *Physics Letters B* 98.4 (Jan. 1981), pp. 265–268. DOI: `10.1016/0370-2693(81)90011-3`.

[75] V. Cirigliano, S. Gardner, and B. R. Holstein. “Beta decays and non-standard interactions in the LHC era”. In: *Progress in Particle and Nuclear Physics* 71 (July 2013), pp. 93–118. DOI: `10.1016/j.ppnp.2013.03.005`.

[76] V. Cirigliano, M. González-Alonso, and M. L. Graesser. “Non-standard charged current interactions: beta decays versus the LHC”. In: *Journal of High Energy Physics* 2 (Feb. 2013), p. 46. DOI: 10.1007/JHEP02(2013)046.

[77] B. T. Cleveland et al. “Measurement of the Solar Electron Neutrino Flux with the Homestake Chlorine Detector”. In: *The Astrophysical Journal* 496.1 (Mar. 1998), p. 505. DOI: 10.1086/305343.

[78] P. 8. Collaboration et al. *The Project 8 Neutrino Mass Experiment*. 2022. arXiv: 2203.07349 [nucl-ex].

[79] P. Coloma et al. *Global constraints on non-standard neutrino interactions with quarks and electrons*. 2023. arXiv: 2305.07698 [hep-ph].

[80] G. Cowan et al. “Asymptotic formulae for likelihood-based tests of new physics”. In: *European Physics Journal C* 71 (2011), p. 1554. DOI: 10.1140/epjc/s10052-011-1554-0.

[81] D. F. Hinz. “Background systematics and extensions to the KATRIN background model”. PhD thesis. Karlsruhe Institute of Technology, 2022. DOI: 10.5445/IR/1000151022.

[82] G. Danby et al. “Observation of High-Energy Neutrino Reactions and the Existence of Two Kinds of Neutrinos”. In: *Physical Review Letters* 9.1 (July 1962), p. 36. DOI: 10.1103/PhysRevLett.9.36.

[83] D. Decamp et al. “A precise determination of the number of families with light neutrinos and of the Z boson partial widths”. In: *Physics Letters B* 235.3-4 (Feb. 1990), pp. 399–411. DOI: 10.1016/0370-2693(90)91984-J.

[84] M. Deniz et al. “Measurement of $\bar{\nu}_e$-electron scattering cross section with a CsI(Tl) scintillating crystal array at the Kuo-Sheng nuclear power reactor”. In: *Physical Review D* 81.7 (Apr. 2010), p. 072001. DOI: 10.1103/PHYSREVD.81.072001.

[85] F. F. Deppisch et al. “Leptoquark patterns unifying neutrino masses, flavor anomalies, and the diphoton excess”. In: *Physical Review D* 94.1 (July 2016), p. 013003. DOI: 10.1103/PHYSREVD.94.013003.

[86] M. Descher. “Differential spectrum modeling and sensitivity for keV sterile neutrino search at KATRIN”. PhD thesis. Karlsruhe Institute of Technology, 2024. DOI: 10.5445/IR/1000166956.

[87] DESI Collaboration et al. *DESI 2024 VI: Cosmological Constraints from the Measurements of Baryon Acoustic Oscillations*. 2024. arXiv: 2404.03002 [astro-ph.CO].

[88] B. Dev et al. “Neutrino non-standard interactions: A status report”. In: *SciPost Physics Proceedings* 2.2 (Dec. 2019), p. 001. DOI: 10.21468/SCIPOSTPHYSPROC.2.001.

[89] N. Doss and J. Tennyson. “Excitations to the electronic continuum of ^{3}HeT$^+$ in investigations of T_2 β-decay experiments”. In: *Journal of Physics B: Atomic, Molecular and Optical Physics* 41.12 (June 2008), p. 125701. DOI: 10.1088/0953-4075/41/12/125701.

[90] N. Doss et al. “Molecular effects in investigations of tritium molecule β decay endpoint experiments”. In: *Physical Review C* 73.2 (Feb. 2006), p. 025502. DOI: 10.1103/PhysRevC.73.025502.

[91] K. Eguchi et al. “First Results from KamLAND: Evidence for Reactor Antineutrino Disappearance”. In: *Physical Review Letters* 90 (Jan. 2003), p. 021802. DOI: 10.1103/PhysRevLett.90.021802.

[92] E. Ellinger. “Development and Investigation of the Forward Beam Monitor for the KATRIN experiment”. PhD thesis. University of Wuppertal, 2019. URL: https://doi.org/10.25926/r160-7a40.

[93] C. P. Enz. “Fermi interaction with non-conservation of «lepton charge» and of parity”. In: *Il Nuovo Cimento* 6.1 (July 1957), pp. 250–254. DOI: 10.1007/BF02827778.

[94] M. Erhard et al. “Technical design and commissioning of the KATRIN large-volume air coil system”. In: *JINST* 13.02 (2018), P02003. DOI: 10.1088/1748-0221/13/02/P02003.

[95] M. Erhard. “Influence of the magnetic field on the transmission characteristics and neutrino mass systematics of the KATRIN experiment”. PhD thesis. Karlsruhe Institute of Technology, 2016. URL: https://publikationen.bibliothek.kit.edu/1000065003.

[96] I. Esteban et al. “NuFit-6.0: updated global analysis of three-flavor neutrino oscillations”. In: *Journal of High Energy Physics* 12 (Dec. 2024), pp. 1–33. DOI: 10.1007/JHEP12(2024)216.

[97] Fabian Block. “Determination of Electromagnetic Fields and Tritium Column Density for Neutrino Mass Analysis with KATRIN”. PhD thesis. Karlsruhe Institute of Technology, 2022. DOI: 10.5445/IR/1000145073.

[98] Y. Farzan and M. Tórtola. “Neutrino oscillations and Non-standard Interactions”. In: *Frontiers in Physics* 5 (Feb. 2018), p. 324394. DOI: 10.3389/FPHY.2018.00010.

[99] G. J. Feldman and R. D. Cousins. “Unified approach to the classical statistical analysis of small signals”. In: *Physical Review D* 57.7 (Apr. 1998), pp. 3873–3889. DOI: 10.1103/PhysRevD.57.3873.

[100] E. Fermi. “Versuch einer Theorie der β-Strahlen”. In: *Zeitschrift für Physik* 88.3-4 (Mar. 1934), pp. 161–177. DOI: 10.1007/BF01351864.

[101] F. Feruglio, P. Paradisi, and A. Pattori. “Lepton flavour violation in composite Higgs models”. In: *The European Physical Journal C* 75.12 (Dec. 2015), pp. 1–26. DOI: 10.1140/EPJC/S10052-015-3807-9.

[102] D. Foreman-Mackey et al. “emcee : The MCMC Hammer ”. In: *Publications of the Astronomical Society of the Pacific* 125.925 (Mar. 2013), pp. 306–312. DOI: 10.1086/670067.

[103] F. Fränkle et al. “Radon induced background processes in the KATRIN pre-spectrometer”. In: *Astroparticle Physics* 35.3 (Oct. 2011), pp. 128–134. DOI: 10.1016/j.astropartphys.2011.06.009.

[104] F. M. Fränkle. “Background Investigations of the KATRIN Pre-Spectrometer”. PhD thesis. Karlsruhe Institute of Technology, 2010. DOI: 10.5445/IR/1000019392.

[105] D. Z. Freedman. “Coherent effects of a weak neutral current”. In: *Physical Review D* 9.5 (Mar. 1974), p. 1389. DOI: 10.1103/PhysRevD.9.1389.

[106] S. Fukuda et al. “Constraints on Neutrino Oscillations Using 1258 Days of Super-Kamiokande Solar Neutrino Data”. In: *Physical Review Letters* 86.25 (June 2001), p. 5656. DOI: 10.1103/PhysRevLett.86.5656.

[107] Y. Fukuda et al. “Evidence for Oscillation of Atmospheric Neutrinos”. In: *Physical Review Letters* 81 (Aug. 1998), pp. 1562–1567. DOI: 10.1103/PhysRevLett.81.1562.

[108] D. Furse et al. “Kassiopeia: a modern, extensible C++ particle tracking package”. In: *New Journal of Physics* 19.5 (May 2017), p. 053012. DOI: 10.1088/1367-2630/AA6950.

[109] D. L. Furse. “Techniques for direct neutrino mass measurement utilizing tritium β-decay”. PhD thesis. Massachusetts Institute of Technology, 2015. URL: https://dspace.mit.edu/handle/1721.1/99313.

[110] A. Gando et al. “Reactor on-off antineutrino measurement with KamLAND”. In: *Physical Review D* 88.3 (Aug. 2013), p. 033001. DOI: 10.1103/PHYSREVD.88.033001.

[111] L. Gastaldo et al. “The Electron Capture Ho-163 Experiment ECHo”. In: *Journal of Low Temperature Physics* 176.5 (May 2014), pp. 876–884. DOI: 10.1007/S10909-014-1187-4.

[112] G. Gelmini and M. Roncadelli. “Left-handed neutrino mass scale and spontaneously broken lepton number”. In: *Physics Letters B* 99.5 (Mar. 1981), pp. 411–415. DOI: 10.1016/0370-2693(81)90559-1.

[113] C. Giunti, C. Kim, and U. Lee. “Coherence of neutrino oscillations in vacuum and matter in the wave packet treatment”. In: *Physics Letters B* 274.1 (Jan. 1992), pp. 87–94. DOI: 10.1016/0370-2693(92)90308-Q.

[114] C. Giunti and C. W. Kim. “Fundamentals of Neutrino Physics and Astrophysics”. In: *Fundamentals of Neutrino Physics and Astrophysics* (Jan. 2007), pp. 1–728. DOI: 10.1093/ACPROF:OSO/9780198508717.001.0001.

[115] F. Glück, I. Joó, and J. Last. “Measurable parameters of neutron decay”. In: *Nuclear Physics A* 593.2 (Oct. 1995), pp. 125–150. DOI: 10.1016/0375-9474(95)00354-4.

[116] F. Glück et al. “Electromagnetic design of the large-volume air coil system of the KATRIN experiment”. In: *New J. Phys.* 15 (2013), p. 083025. DOI: 10.1088/1367-2630/15/8/083025.

[117] M. Gonzalez-Alonso, O. Naviliat-Cuncic, and N. Severijns. “New physics searches in nuclear and neutron β decay”. In: *Progress in Particle and Nuclear Physics* 104 (Mar. 2018), pp. 165–223. DOI: 10.1016/j.ppnp.2018.08.002.

[118] M. González-Alonso and J. M. Camalich. “Isospin Breaking in the Nucleon Mass and the Sensitivity of β Decays to New Physics”. In: *Physical Review Letters* 112 (2014), p. 042501. DOI: 10.1103/PhysRevLett.112.042501.

[119] M. González-Alonso, J. Martin Camalich, and K. Mimouni. “Renormalization-group evolution of new physics contributions to (semi)leptonic meson decays”. In: *Physics Letters B* 772 (Sept. 2017), pp. 777–785. DOI: 10.1016/J.PHYSLETB.2017.07.003.

[120] S. Görhardt. “Background Reduction Methods and Vacuum Technology at the KATRIN Spectrometer”. PhD thesis. Karlsruhe Institute of Technology, 2014. URL: https://publikationen.bibliothek.kit.edu/1000038050.

[121] S. Groh. “Modeling of the response function and measurement of transmission properties of the KATRIN experiment”. PhD thesis. Karlsruhe Institute of Technology, 2015. DOI: 10.5445/IR/1000046546.

[122] B. Grzadkowski et al. “Dimension-six terms in the Standard Model Lagrangian”. In: *Journal of High Energy Physics* 10 (Oct. 2010), pp. 1–18. DOI: 10.1007/JHEP10(2010)085.

[123] A. Gupta, D. Majumdar, and S. Prakash. *Neutrino oscillation measurements with JUNO in the presence of scalar NSI*. 2023. arXiv: 2306.07343 [hep-ph].

[124] W. Hampel et al. “GALLEX solar neutrino observations: Results for GALLEX IV”. In: *Physics Letters B* 447.1-2 (1999), pp. 127–133. DOI: 10.1016/S0370-2693(98)01579-2.

[125] T. Han et al. “Scalar and tensor neutrino interactions”. In: *Journal of High Energy Physics* 07 (2020), p. 207. DOI: 10.1007/JHEP07(2020)207.

[126] F. Harms. “Characterization and Minimization of Background Processes in the KATRIN Main Spectrometer”. PhD thesis. Karlsruhe Institute of Technology, 2015. DOI: 10.5445/IR/1000050027.

[127] W. K. Hastings. “Monte Carlo sampling methods using Markov chains and their applications”. In: *Biometrika* 57.1 (Apr. 1970), pp. 97–109. DOI: 10.1093/BIOMET/57.1.97.

[128] C. Hati et al. “Reconciling B-meson decay anomalies with neutrino masses, dark matter and constraints from flavour violation”. In: *Journal of High Energy Physics* 11 (Nov. 2018), pp. 1–46. DOI: 10.1007/JHEP11(2018)011.

[129] N. Haußmann. “Development of Analysis Tools and Automatisation of Run Control for KATRIN”. PhD thesis. Karlsruhe Institute of Technology, 2013. URL: https://www.katrin.kit.edu/publikationen/dth-Haussmann.pdf.

[130] K. Hayasaka et al. “Search for lepton-flavor-violating τ decays into three leptons with 719 million produced $\tau^+\tau^-$ pairs”. In: *Physics Letters B* 687.2-3 (Apr. 2010), pp. 139–143. DOI: 10.1016/J.PHYSLETB.2010.03.037.

[131] J. Heeck and D. Teresi. “Pati-Salam explanations of the B-meson anomalies”. In: *Journal of High Energy Physics* 12 (Dec. 2018), pp. 1–34. DOI: 10.1007/JHEP12(2018)103.

[132] G. Hooft. “Naturalness, Chiral Symmetry, and Spontaneous Chiral Symmetry Breaking”. In: *Recent Developments in Gauge Theories* (1980), pp. 135–157. DOI: 10.1007/978-1-4684-7571-5_9.

[133] M. Hötzel. “Simulation and analysis of source-related effects for KATRIN”. PhD thesis. Karlsruhe Institute of Technology, 2012. DOI: 10.5445/IR/1000031259.

[134] K. Hugenberg. “Design of the electrode system of the KATRIN main spectrometer”. PhD thesis. University of Münster, 2008. URL: http://www.uni-muenster.de/Physik.KP/AGWeinheimer/theses/Diplom_Karen_Hugenberg.pdf.

[135] J. M. Hyde. “Biprobability approach to CP phase degeneracy from non-standard neutrino interactions”. In: *Nuclear Physics B* 949 (Dec. 2019), p. 114804. DOI: 10.1016/J.NUCLPHYSB.2019.114804.

[136] J. D. Jackson, S. B. Treiman, and H. W. Wyld. “Possible Tests of Time Reversal Invariance in Beta Decay”. In: *Physical Review* 106.3 (May 1957), p. 517. DOI: 10.1103/PhysRev.106.517.

[137] T. M. James et al. “Automated Quantitative Spectroscopic Analysis Combining Background Subtraction, Cosmic Ray Removal, and Peak Fitting”. In: *Applied Spectroscopy* 67.8 (Aug. 2013), pp. 949–959. DOI: 10.1366/12-06766.

[138] S. Jana, L. Puetter, and A. Y. Smirnov. “Restricting Sterile Neutrinos by Neutrinoless Double Beta Decay”. In: *Physical Review D* 111 (Jan. 2025), p. 015011. DOI: 10.1103/PhysRevD.111.015011.

[139] E. E. Jenkins, A. V. Manohar, and P. Stoffer. “Low-energy effective field theory below the electroweak scale: operators and matching”. In: *Journal of High Energy Physics* 3 (Mar. 2018), p. 16. DOI: 10.1007/JHEP03(2018)016.

[140] K. v. Meyenn, ed. *Wolfgang Pauli - Wissenschaftlicher Briefwechsel mit Bohr, Einstein, Heisenberg u.a.* XXX. Vol. 2. 1985.

[141] W. Käfer. “Sensitivity Studies for the KATRIN experiment”. PhD thesis. Karlsruhe Institute of Technology, 2012. DOI: 10.5445/IR/1000026021.

[142] H. de Kerret et al. “Double Chooz θ_{13} measurement via total neutron capture detection”. In: *Nature Physics* 16.5 (Apr. 2020), pp. 558–564. DOI: 10.1038/s41567-020-0831-y.

[143] Kerstin Schönung. “Development of a Rear Wall for the KATRIN Rear Section and investigation of tritium compatibility of Rear Section components”. PhD thesis. Karlsruhe Institute of Technology, 2016. DOI: 10.5445/IR/1000056077.

[144] A. N. Khan, W. Rodejohann, and X.-J. Xu. “Borexino and general neutrino interactions”. In: *Physical Review D* 101 (2020). DOI: 10.1103/PhysRevD.101.055047.

[145] M. Kleesiek et al. “β-Decay spectrum, response function and statistical model for neutrino mass measurements with the KATRIN experiment”. In: *The European Physical Journal C* 79.3 (Mar. 2019), p. 204. DOI: 10.1140/epjc/s10052-019-6686-7.

[146] M. Kleesiek. “A Data-Analysis and Sensitivity-Optimization Framework for the KATRIN Experiment”. PhD thesis. Karlsruhe Institute of Technology, 2014. URL: http://nbn-resolving.org/urn:nbn:de:swb:90-433013%5Cnhttp://digbib.ubka.uni-karlsruhe.de/volltexte/1000043301.

[147] C. Klein, M. Lindner, and S. Ohmer. “Minimal radiative neutrino masses”. In: *Journal of High Energy Physics* 3 (Mar. 2019), pp. 1–24. DOI: 10.1007/JHEP03(2019)018.

[148] M. Klein. “Tritium ions in KATRIN: blocking, removal and detection”. PhD thesis. Karlsruhe Institute of Technology, 2018. DOI: 10.5445/IR/1000093526.

[149] K. Kodama et al. “Observation of tau neutrino interactions”. In: *Physics Letters B* 504.3 (Apr. 2001), pp. 218–224. DOI: 10.1016/S0370-2693(01)00307-0.

[150] Korbinian Urban. “Application of a TRISTAN Silicon Drift Detector as Forward Beam Monitor in KATRIN”. Master’s thesis. Technical University of Munich, 2019. URL: https://publications.mppmu.mpg.de/2019/MPP-2019-356/FullText.pdf.

[151] L. Kuckert. “The windowless gaseous tritium source of the KATRIN experiment – Characterisation of gas dynamical and plasma properties”. PhD thesis. Karlsruhe Institute of Technology, 2016. DOI: 10.5445/IR/1000065077.

[152] L. W. Köllenberger. “Combined neutrino-mass analysis of the first five KATRIN science runs”. PhD thesis. Karlsruhe Institute of Technology, 2024. DOI: 10.5445/IR/1000170238.

[153] J. Lauer. “Search for new light bosons with the KATRIN experiment”. In: *Proceedings of 42nd International Conference on High Energy Physics* 476 (Dec. 2024), p. 326. DOI: 10.22323/1.476.0326.

[154] T. D. Lee and C. N. Yang. “Question of Parity Conservation in Weak Interactions”. In: *Physical Review* 104.1 (Oct. 1956), pp. 254–258. DOI: 10.1103/PhysRev.104.254.

[155] T. Li, X. D. Ma, and M. A. Schmidt. “General neutrino interactions with sterile neutrinos in light of coherent neutrino-nucleus scattering and meson invisible decays”. In: *Journal of High Energy Physics* 7 (July 2020), pp. 1–34. DOI: `10.1007/JHEP07(2020)152`.

[156] J. Liao, D. Marfatia, and K. Whisnant. “Degeneracies in long-baseline neutrino experiments from nonstandard interactions”. In: *Physical Review D* 93.9 (May 2016), p. 093016. DOI: `10.1103/PHYSREVD.93.093016`.

[157] J. Liao, D. Marfatia, and K. Whisnant. “Nonstandard neutrino interactions at DUNE, T2HK and T2HKK”. In: *Journal of High Energy Physics* 1 (Jan. 2017), pp. 1–27. DOI: `10.1007/JHEP01(2017)071`.

[158] M. Lindner, W. Rodejohann, and X. J. Xu. “Coherent neutrino-nucleus scattering and new neutrino interactions”. In: *Journal of High Energy Physics* 3 (Mar. 2017), pp. 1–29. DOI: `10.1007/JHEP03(2017)097`.

[159] V. M. Lobashev and P. E. Spivak. “A method for measuring the electron antineutrino rest mass”. In: *Nuclear Instruments and Methods in Physics Research Section A: Accelerators, Spectrometers, Detectors and Associated Equipment* 240.2 (Oct. 1985), pp. 305–310. DOI: `10.1016/0168-9002(85)90640-0`.

[160] A. V. Lokhov and F. V. Tkachov. “Confidence intervals with a priori parameter bounds”. In: *Physics of Particles and Nuclei* 46.3 (May 2015), pp. 347–365. DOI: `10.1134/S1063779615030089`.

[161] A. Lokhov et al. “Background reduction at the KATRIN experiment by the shifted analysing plane configuration”. In: *The European Physical Journal C* 82.3 (Mar. 2022), pp. 1–11. DOI: `10.1140/EPJC/S10052-022-10220-4`.

[162] P. O. Ludl and W. Rodejohann. “Direct neutrino mass experiments and exotic charged current interactions”. In: *Journal of High Energy Physics* 6 (2016), p. 40. DOI: `10.1007/JHEP06(2016)040`.

[163] E. Ma. “Verifiable radiative seesaw mechanism of neutrino mass and dark matter”. In: *Physical Review D* 73.7 (Apr. 2006), p. 077301. DOI: `10.1103/PhysRevD.73.077301`.

[164] M. B. Machatschek. “A Phenomenological Theory of KATRIN Source Potential Systematics and its Application in Krypton-83m Calibration Measurements”. PhD thesis. Karlsruhe Institute of Technology, 2021. DOI: `10.5445/IR/1000132391`.

[165] Z. Maki, M. Nakagawa, and S. Sakata. “Remarks on the Unified Model of Elementary Particles”. In: *Progress of Theoretical Physics* 28.5 (Nov. 1962), pp. 870–880. DOI: `10.1143/PTP.28.870`.

[166] M. Malinský, T. Ohlsson, and H. Zhang. “Nonstandard neutrino interactions from a triplet seesaw model”. In: *Physical Review D* 79.1 (Jan. 2009), p. 011301. DOI: `10.1103/PhysRevD.79.011301`.

[167] S. Mertens et al. “Background due to stored electrons following nuclear decays in the KATRIN spectrometers and its impact on the neutrino mass sensitivity”. In: *Astroparticle Physics* 41 (Jan. 2013), pp. 52–62. DOI: `10.1016/j.astropartphys.2012.10.005`.

[168] P. Minkowski. “$\mu \to e\gamma$ at a rate of one out of 109 muon decays?” In: *Physics Letters B* 67.4 (Apr. 1977), pp. 421–428. DOI: `10.1016/0370-2693(77)90435-X`.

[169] R. N. Mohapatra and J. C. Pati. “"Natural" left-right symmetry”. In: *Physical Review D* 11.9 (May 1975), p. 2558. DOI: `10.1103/PhysRevD.11.2558`.

[170] R. N. Mohapatra and G. Senjanović. “Neutrino Mass and Spontaneous Parity Nonconservation”. In: *Physical Review Letters* 44.14 (Apr. 1980), pp. 912–915. DOI: 10.1103/PhysRevLett.44.912.

[171] D. Naredo-Tuero et al. *Living at the Edge: A Critical Look at the Cosmological Neutrino Mass Bound.* 2024. arXiv: 2407.13831 [astro-ph.CO].

[172] A. Nava. “Detector and beamline response modeling for differential electron measurements with the KATRIN experiment”. PhD thesis. Milan Bicocca U., 2025.

[173] S. Navas et al. “Review of Particle Physics”. In: *Physical Review D* 110.3 (Aug. 2024), p. 030001. DOI: 10.1103/PhysRevD.110.030001.

[174] O. Naviliat-Cuncic and M. González-Alonso. “Prospects for precision measurements in nuclear β decay in the LHC era”. In: *Annalen der Physik* 525.8-9 (Sept. 2013), pp. 600–619. DOI: 10.1002/andp.201300072.

[175] J. Neyman. “Outline of a Theory of Statistical Estimation Based on the Classical Theory of Probability”. In: *Philosophical Transactions of the Royal Society of London. Series A, Mathematical and Physical Sciences* 236.767 (Aug. 1937), pp. 333–380. DOI: 10.1098/rsta.1937.0005.

[176] T. Ohlsson. “Status of non-standard neutrino interactions”. In: *Reports on Progress in Physics* 76.4 (Mar. 2013), p. 044201. DOI: 10.1088/0034-4885/76/4/044201.

[177] E. W. Otten and C. Weinheimer. “Neutrino mass limit from tritium β decay”. In: *Reports on Progress in Physics* 71.8 (Aug. 2008), p. 086201. DOI: 10.1088/0034-4885/71/8/086201.

[178] D. K. Papoulias and T. S. Kosmas. “COHERENT constraints to conventional and exotic neutrino physics”. In: *Physical Review D* 97.3 (Feb. 2018), p. 033003. DOI: 10.1103/PHYSREVD.97.033003.

[179] J. C. Pati and A. Salam. “Unified Lepton-Hadron Symmetry and a Gauge Theory of the Basic Interactions”. In: *Physical Review D* 8.4 (Aug. 1973), pp. 1240–1251. DOI: 10.1103/PhysRevD.8.1240.

[180] P. F. Pérez and M. B. Wise. “On the origin of neutrino masses”. In: *Physical Review D* 80.5 (Sept. 2009), p. 053006. DOI: 10.1103/PhysRevD.80.053006.

[181] A. Picard et al. “A solenoid retarding spectrometer with high resolution and transmission for keV electrons”. In: *Nuclear Instruments and Methods in Physics Research Section B: Beam Interactions with Materials and Atoms* 63.3 (Feb. 1992), pp. 345–358. DOI: 10.1016/0168-583X(92)95119-C.

[182] R. L. Plackett. “Karl Pearson and the Chi-Squared Test”. In: *International Statistical Review* 51.1 (Apr. 1983). DOI: 10.2307/1402731.

[183] B. Pontecorvo. “Mesonium and anti-mesonium”. In: *Sov. Phys. JETP* 6 (1957), p. 429.

[184] M. Prall et al. “The KATRIN pre-spectrometer at reduced filter energy”. In: *New Journal of Physics* 14.7 (July 2012), p. 073054. DOI: 10.1088/1367-2630/14/7/073054.

[185] F. Priester and B. Bornschein. “TriToP – A compatibility experiment with turbomolecular pumps under tritium atmosphere”. In: *Vacuum* 98 (Dec. 2013), pp. 22–28. DOI: 10.1016/J.VACUUM.2012.09.006.

[186] F. Priester, M. Sturm, and B. Bornschein. “Commissioning and detailed results of KATRIN inner loop tritium processing system at Tritium Laboratory Karlsruhe”. In: *Vacuum* 116 (June 2015), pp. 42–47. DOI: 10.1016/J.VACUUM.2015.02.030.

[187] F. Priester et al. “Tritium Processing Systems and First Tritium Operation of the KATRIN Experiment”. In: *Fusion Science and Technology* 76.4 (May 2020), pp. 600–604. DOI: 10.1080/15361055.2020.1730118.

[188] X. Qian and P. Vogel. “Neutrino mass hierarchy”. In: *Progress in Particle and Nuclear Physics* 83 (July 2015), pp. 1–30. DOI: 10.1016/J.PPNP.2015.05.002.

[189] F. Reines and C. L. Cowan. “Free Antineutrino Absorption Cross Section. I. Measurement of the Free Antineutrino Absorption Cross Section by Protons”. In: *Physical Review* 113.1 (Jan. 1959), pp. 273–279. DOI: 10.1103/PhysRev.113.273.

[190] W. W. Repko and C.-e. Wu. “Radiative corrections to the end point of the tritium β decay spectrum”. In: *Physical Review C* 28.6 (Dec. 1983), pp. 2433–2436. DOI: 10.1103/PhysRevC.28.2433.

[191] W. Rodejohann, X. J. Xu, and C. E. Yaguna. “Distinguishing between Dirac and Majorana neutrinos in the presence of general interactions”. In: *Journal of High Energy Physics* 2017.5 (May 2017), pp. 1–21. DOI: 10.1007/JHEP05(2017)024.

[192] C. Rodenbeck. “A method for determining the transition energies of ^{83m}Kr at the KATRIN experiment”. In: *The European Physics Journal C* 82.8 (Aug. 2022), p. 700. DOI: 10.1140/EPJC/S10052-022-10667-5.

[193] C. Röttele. “Tritium suppression factor of the KATRIN transport section”. PhD thesis. Karlsruher Institute of Technology, 2019. DOI: 10.5445/IR/1000096733.

[194] A. Saenz and P. Froelich. “Effect of final-state interactions in allowed β decays. II. Reliability of the β-decay spectrum for T2”. In: *Physical Review C* 56.4 (Oct. 1997), pp. 2162–2184. DOI: 10.1103/PhysRevC.56.2162.

[195] A. Saenz, S. Jonsell, and P. Froelich. “Improved Molecular Final-State Distribution of HeT$^+$ for the β-Decay Process of T”. In: *Physical Review Letters* 84.2 (Jan. 2000), pp. 242–245. DOI: 10.1103/PhysRevLett.84.242.

[196] J. Schechter and J. W. F. Valle. “Neutrino masses in SU(2) $\otimes$ U(1) theories”. In: *Physical Review D* 22.9 (Nov. 1980), pp. 2227–2235. DOI: 10.1103/PhysRevD.22.2227.

[197] L. Schimpf. “Characterisation of energy loss processes of 18.6 keV electrons inside the windowless tritium source of KATRIN”. PhD thesis. Karlsruhe Institute of Technology, 2021. DOI: 10.5445/IR/1000131810.

[198] M. Schlösser et al. “Accurate calibration of the laser Raman system for the Karlsruhe Tritium Neutrino Experiment”. In: *Journal of Molecular Structure* 1044 (July 2013), pp. 61–66. DOI: 10.1016/J.MOLSTRUC.2012.11.022.

[199] M. D. Schwartz. *Quantum Field Theory and the Standard Model*. Cambridge University Press, 2014. ISBN: 978-1-107-03473-0.

[200] J. S. Schwarz. “The Detector System of the KATRIN Experiment - Implementation and First Measurements with the Spectrometer”. PhD thesis. Karlsruhe Institute of Technology, 2014. DOI: 10.5445/IR/1000042772.

[201] C. D. Shin et al. “Observation of reactor antineutrino disappearance using delayed neutron capture on hydrogen at RENO”. In: *Journal of High Energy Physics* 29 (Apr. 2020), pp. 1–27. DOI: 10.1007/JHEP04(2020)029.

[202] D. Siegmann et al. “Development of a Silicon Drift Detector Array to Search for keV-scale Sterile Neutrinos with the KATRIN Experiment”. In: *Journal of Physics G* 51.8 (June 2024), p. 085202. DOI: 10.1088/1361-6471/ad4bf8.

[203] F. Simkovic, R. Dvornicky, and A. Faessler. “Exact relativistic tritium beta-decay endpoint spectrum in a hadron model”. In: *Physical Review C - Nuclear Physics* 77.5 (Dec. 2007). DOI: 10.1103/PhysRevC.77.055502.

[204] Sonja Schneidewind. “Determination of the energy-dependent energy-loss function and sensitivity improvements for the KATRIN experiment”. PhD thesis. University of Münster, to be published 2025.

[205] N. M. Steinbrink et al. “Statistical sensitivity on right-handed currents in presence of eV scale sterile neutrinos with KATRIN”. In: *Journal of Cosmology and Astroparticle Physics* 2017.06 (June 2017), p. 015. DOI: 10.1088/1475-7516/2017/06/015.

[206] Y. Suzuki. “Kamiokande solar neutrino results”. In: *Nuclear Physics B - Proceedings Supplements* 38.1-3 (Jan. 1995), pp. 54–59. DOI: 10.1016/0920-5632(94)00733-C.

[207] N. R.-M. Trost. “Modeling and measurement of Rydberg-State mediated Background at the KATRIN Main Spectrometer”. PhD thesis. Karlsruhe Institute of Technology, 2018. DOI: 10.5445/IR/1000090450.

[208] K. Valerius. “Spectrometer-related background processes and their suppression in the KATRIN experiment”. PhD thesis. University of Münster, 2009. URL: https://repositorium.uni-muenster.de/document/miami/93137705-73f4-404a-a438-09d487cbff63/diss_valerius.pdf.

[209] P. Vilain et al. “Measurement of differential cross sections for muon-neutrino electron scattering”. In: *Physics Letters B* 302.2-3 (Mar. 1993), pp. 351–355. DOI: 10.1016/0370-2693(93)90408-A.

[210] P. Vilain et al. “Precision measurement of electroweak parameters from the scattering of muon-neutrinos on electrons”. In: *Physics Letters B* 335.2 (Sept. 1994), pp. 246–252. DOI: 10.1016/0370-2693(94)91421-4.

[211] K. C. Wang. “A Suggestion on the Detection of the Neutrino”. In: *Physical Review* 61.1-2 (1942), p. 97. DOI: 10.1103/PhysRev.61.97.

[212] S. Weinberg. “A Model of Leptons”. In: *Physical Review Letters* 19.21 (Nov. 1967), pp. 1264–1266. DOI: 10.1103/PhysRevLett.19.1264.

[213] S. Weinberg. “Baryon- and Lepton-Nonconserving Processes”. In: *Physical Review Letters* 43.21 (Nov. 1979), pp. 1566–1570. DOI: 10.1103/PhysRevLett.43.1566.

[214] S. S. Wilks. “The Large-Sample Distribution of the Likelihood Ratio for Testing Composite Hypotheses”. In: *Ann. Math. Statist.* 9.1 (Mar. 1938), pp. 60–62. DOI: 10.1214/AOMS/1177732360.

[215] M. B. Wise and Y. Zhang. “Effective theory and simple completions for neutrino interactions”. In: *Physical Review D - Particles, Fields, Gravitation and Cosmology* 90.5 (Sept. 2014), p. 053005. DOI: 10.1103/PHYSREVD.90.053005.

[216] M. Zacher. “High-field electrodes design and an angular-selective photoelectron source for the KATRIN spectrometers”. PhD thesis. University of Münster, 2015.

[217] A. Zee. “A theory of lepton number violation and neutrino Majorana masses”. In: *Physics Letters B* 93.4 (June 1980), pp. 389–393. DOI: 10.1016/0370-2693(80)90349-4.

[218] K. Zuber. *Neutrino Physics*. Third edition. | Boca Raton : CRC Press, 2020. | Series: Series in high energy physics, cosmology & gravitation: CRC Press, May 2020. ISBN: 9781315195612. DOI: 10.1201/9781315195612.

Acknowledgements

Lastly, I would like to express my sincerest gratitude to all the wonderful people both at KATRIN and in my private life who have accompanied me on my way and made my PhD into such a wonderful experience. In particular, I would like to thank a few people that have been invaluable for the success of this work:

- Firstly, I would like to thank Prof. Guido Drexlin for awakening my interest in neutrino physics during his lectures, for encouraging me to take on part of the data analysis for my Master's Thesis and finally giving me so many opportunities to follow my interests, travel to conferences, and promote my work during my PhD.
- Equally, I want to thank Prof. Kathrin Valerius for always showing interest in my work, giving me lots of helpful feedback, both for my presentations and publications, as well as being so supportive of my further training in teaching. I also enjoyed working on equal opportunity events together and going on group runs.
- I dearly have to thank Dr. Alexey Lokhov for always being there, lifting my spirits, engaging in countless physics discussions, giving comments and feedback, and during all that time being such a pleasant person to share an office with.
- Also, thank you, Hanna Henke, for your trust, joining the analysis team, and tirelessly performing studies for me when I was stressed.
- Furthermore, I would like to thank the Krypton team, Dr. Magnus Schlösser, Dr. Moritz Machatschek, and Matthias Böttcher for all the endurance, effort, and teamwork that went into finalising our work on the source systematic. It was only possible with all of you and I'm so happy that we finally made it.
- I also want to thank the people which helped me prepare my work for publication through their thorough review and fruitful discussions, especially Weiran Xu, Benedikt Bieringer, Joscha Lauer and Dr. Ferenc Glück.
- Finally, I am grateful for the great atmosphere and companionship we had at the institute, that exceeded the day-to-day work. Joscha Lauer, Jaroslav Štorek, Svenja Heyns, Neven Kovač, and Dr. Khushbakht Habib, thank you for every fun break we had, for going on conferences and summer schools with me, spending time together on the weekends, and always supporting each other. You really made this into a wonderful time for me.